INFLUENCE OF Gd SUBSTITUTION ON STRUCTURAL AND MAGNETIC PROPERTIES OF $Co_{0.40}Cu_{0.20}Zn_{0.40}Gd_xFe_{2-x}O_4$

A Dissertation Submitted to the Department of Physics, Bangladesh University of Engineering & Technology, Dhaka, in Partial Fulfillment of the Requirement for the Degree of Master of Philosophy in Physics

SUBMITTED

By

MOHAMMED ANWAR HOSSAIN

Examination Roll No. : 0411143004P

Session : April 2011

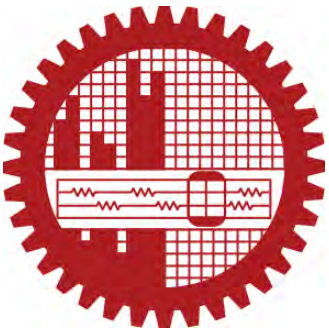

DEPARTMENT OF PHYSICS

BANGLADESH UNIVERSITY OF ENGINEERING & TECHNOLOGY

DHAKA 1000, BANGLADESH

CANDIDATE'S DECLARATION

It is hereby declared that this thesis or any part of it has not been submitted elsewhere for the award of any degree or diploma.

Mohammed Anwar Hossain

BANGLADESH UNIVERSITY OF ENGINEERING & TECHNOLOGY
DEPARTMENT OF PHYSICS, DHAKA 1000, BANGLADESH

CERTIFICATION OF THESIS

The thesis titled **"INFLUENCE OF Gd SUBSTITUTION ON SRUCTURAL AND MAGNETIC PROPERTIES OF $Co_{0.40}Cu_{0.20}Zn_{0.40}Gd_xFe_{2-x}O_4$"** submitted by **MOHAMMED ANWAR HOSSAIN,** Roll No.: 0411143004 P, Session: April 2011, has been accepted as satisfactory in partial fulfillment of the requirement for the degree of **Master of Philosophy** (M. phil.) in Physics on **September 04, 2016.**

BOARD OF EXAMINERS

1. (A. Hassan) — Chairman
   Dr. A. K. M. Akther Hossain (Supervisor)
   Professor, Department of Physics,
   BUET, Dhaka-1000, Bangladesh

2. (F. Khanam) — Member (Ex- Officio)
   Mrs. Fahima Khanam
   Head and Professor, Department of Physics,
   BUET, Dhaka-1000, Bangladesh

3. ( ) — Member
   Dr. Md. Abu Hashan Bhuiyan
   Professor, Department of Physics,
   BUET, Dhaka-1000, Bangladesh.

4. ( ) — Member
   Dr. Md. Mostak Hossain
   Professor, Department of Physics,
   BUET, Dhaka-1000, Bangladesh.

5. ( ) — Member (External)
   Dr. Md. Mizanur Rahman
   Associate Professor, Department of Physics,
   University of Dhaka, Dhaka-1000, Bangladesh.

DEDICATED TO

MY FATHER

MOHAMMED ABUL BASHAR

AND

MY BELOVED MOTHER

ANWARA BEGUM

ACKNOWLEDGEMENTS

First of all I express all my admiration and devotion to the almighty Allah, the most beneficent who has enabled me to perform this research work and to submit this thesis.

I express my profound gratitude to my honorable supervisor Prof. Dr. A.K.M. Akther Hossain, Department of Physics, Bangladesh University of Engineering and Technology (BUET), for his constant direction, constructive criticism and inspiration in pursuing the whole investigation of the present research. Words are always insufficient to express his working capacities and unending enthusiasm for scientific rigorousness for innovative investigations. This always becomes the everlasting source of inspiration for his students.

I am very grateful to Prof. Fahima Khanam, Head, Department of Physics, BUET, Dhaka, Bangladesh, for giving me all sorts of supports from the Department.I like to express my gratitude to Prof. Dr. Md. Abu Hashan Bhuiyan, Prof. Dr. Jiban Podder, Prof. Dr. Md. Feroz Alam Khan, Prof. Dr. Md. Mostak Hossain, Prof. Dr. Afia Begum, Prof. Dr. Md. Forhad Mina, Prof. Dr. Md. Rafi Uddin, Dr. Nasreen Akter, Dr. Mohammad Abdul Basith, Dr. Mohammad Abu Sayem Karal and all other teachers of the Department of Physics, for their cooperation.

I would like to thank Dr. Nazrul Islam Khan, Principal Scientific Officer, Materials Science Division, Atomic Energy Commission, Dhaka, Bangladesh, for giving me all sorts of supports to measure the XRD analysis of my various samples.

I am also grateful to Dr. Farhad Alam Dr. Md. Belal Hossain, Dr. Sajal Chandra Mazumder & Dr. Mohammad Julhash Miah, for their inspiration and encouragement. I wish to give special thanks to PhD researchers of the Department of Physics, Abdulla Al-Momin, Md. Kamrul Haque Bhuiyan, Bablu Chandra Das & Roksana pervin for their constant support. I also gratefully acknowledge the wishes to M.Phil. Research fellows, Md. Nazrul Islam, Mamun-Ar-Rashid, Abdul Ahad, Md. Arifur Rahman, Sonnet Kumar, and all others researchers of Experimental Solid State Physics Lab, BUET, for their cooperation throughout the study.

I remember with much gratefulness Honorable Planning Minister Lotus Kamal, Md. Ibrahim Khalil Mozumder and other members of GB, Principal Md. Zakir Hossain, Maolana Lokman Hakim & all respected teachers of Choto Sarifpur Degree College for their valuable suggestions and inspiration.

Finally, I would mention a very special gratefulness for the moral support and sustaining inspiration provided by the members of my family. This dissertation would never have been possible without their love and affection.

(Mohammed Anwar Hossain)

Author

ABSTRACT

Polycrystalline $Co_{0.40}Cu_{0.20}Zn_{0.40}Gd_xFe_{2-x}O_4$ prepared by standard solid state reaction technique sintered at various temperatures (1000, 1050, 1100 and 1150ºC) in air for 3 hours. Structural, surface morphology and compositional analysis are characterized by X-ray diffraction (XRD) and Scanning electron microscopy (SEM) respectively. The DC magnetizations as a function of applied magnetic field are performed and increases with increasing applied magnetic field up to 0.1T, then saturation occurs. The XRD patterns confirm the formation of spinel structure. The lattice parameter, a_o, increases with the Gd content. The bulk density (ρ_B) increases and porosity (p) of the samples decreases with the increase of Gd content. The average grain size increases with the Gd content, then decreases. The initial permeability ($\mu_i^{/}$) is found to increase with Gd content up to x=0.050 and then decreases. The value of Q-factor increases with increasing Gd contents from x=0.000 to x=0.050, then it decreases. The real part of dielectric constant ($\varepsilon^{/}$) initially decreases rapidly in the low frequency region but at very high frequencies its value becomes so small that it becomes independent of applied frequency. The dielectric loss tangent ($\tan\delta_E$) decreases with the increase of Gd content due to the decrease of polarization. The value of electric modulus ($M^{/}$) is very low in the low frequency region. As frequency increases the value of $M^{/}$ increases and reaches a maximum constant value. The value of $Z^{/}$ (real part of impedance) and $Z^{//}$ (imaginary part impedance) decrease with increasing frequency. The decrease in the values of $Z^{/}$ and $Z^{//}$ shows that the ac conductivity increases as the frequency increases and $Z^{/}$ indicates dielectric relaxation process. The value of AC conductivity (ζ_{AC}) increases with AC applied field which obeys the Jonschers power law.

CONTENTS

CHAPTER 4

EXPERIMENTAL TECHNIQUES 63-80

LIST OF FIGURES

LIST OF TABLES **Pages**

LIST OF SYMBOLS AND ABBREVIATIONS

B	Magnetic induction
D	Average grain diameter
$F(\theta)$	Nelson-Riley function
f_r	Resonance frequency
g	Landé splitting factor
H_c	Coercivity
H_s	Saturation magnetizing field
J	Current density
J_{ij}	Exchange integral
K	Total anisotropy
K_1	Magneto-crystalline anisotropy constant
L_s	Self-inductance of the sample core
L_o	Inductance of the winding coil without sample
M	Magnetization
M_s	Saturation magnetization
M_r	Remanance
N	Number of turn
N_A	Avogadro's number
n_B	Number of Bohr magneton
P	Porosity
P_{intra}	Intra-granular porosity
P_{inter}	Inter-granular porosity
P_e	Eddy current loss
RQF	Relative quality factor
T_C	Curie temperature
T_N	Néel temperature
T_S	Sintering temperature
$\tan\delta$	Loss tangent (Magnetic/Dielectric)
$Z^{/}$	Real part of impedance
$Z^{//}$	Imaginary part of impedance
$\alpha_{Y\text{-}K}$	Yafet-Kittle angle

β	Peak breadth
γ	Domain wall energy
ω	Angular velocity
δ	Phase angle
ζ_{ac}	AC conductivity
$\varepsilon^{/}$	Real part dielectric constant
$\varepsilon^{//}$	Imaginary part dielectric constant
μ_w	Wall permeability
μ_i	Initial permeability
$\mu_i^{/}$	Real part of complex permeability
$\mu_i^{//}$	Imaginary part of complex permeability
μ_B	Bohr magneton
μ_o	Permeability of free space
μ_r	Relative permeability
χ_{spin}	Intrinsic rotational susceptibility
χ_w	Domain wall susceptibility
$\rho_{X\text{-}ray}$	Theoretical density
ρ_B	Bulk density
a_o	Lattice constant
(hkl)	Miller indices
$M^{/}$	Real part of electric modulus
$M^{//}$	Imaginary part of electric modulus
B-site	Octahedral site
A-site	Tetrahedral site
EMI	Electromagnetic interference
FWHM	Full width at half maximum
AC	Alternating current
VSM	Vibrating Sample Magnetometer
XRD	X-ray diffraction
SEM	Scanning Electron Microscope

CHAPTER 1

INTRODUCTION

1.1 Background and present state of the problem

Ferrite materials with spinel or inverse spinel structure play an important role in technological and magnetic applications because of their high saturation magnetization, sufficiently low dielectric losses over a wide range of frequencies, high electrical resistivity and large permeability [1-4]. According to their crystal structure, spinel-type ferrites have natural super lattice. They have tetrahedral A sites and octahedral B sites in AB_2O_4 crystal structure. They show various magnetic properties depending on the composition and cation distribution. Various cations can be placed in the A sites and B sites to tune its magnetic properties. Depending on the A site and B site cations, it can exhibit ferromagnetic, antiferromagnetic, spin-(cluster) glass and paramagnetic behavior [5-7].

Cobalt ferrites present an increasing interest in applications like magneto-optical devices and high-density recording media due to their large coercive field, high magneto-crystalline anisotropy, moderate saturation magnetization, remarkable chemical stability and mechanical hardness [8-10]. In the last decade, an increasing attention was given to magnetoelectric composites based on cobalt ferrite [11, 12]. Co-Zn ferrite is also a candidate material for applications in drug delivery [13]. These are hard magnetic material having high Neel temperature.

Permeability is one of the most important parameters used in evaluating ferrimagnetic materials. Not only it is a function of the chemical composition and crystal structure but it is strongly dependent on microstructure, temperature, stress,

and several other factors [14]. Magnetocrystalline anisotropy and magnetostriction affect the mechanism of magnetization which also includes the permeability [14].

The uniformity of the grain and the average grain size play an important role for magnetic properties such as the permeability. The sintering temperature has a great influence on the microstructure of the ferrites [15]. The electrical and magnetic properties of *Co*-based ferrites are controlled by the density, porosity, grain size and other features of the saturation magnetization. It strongly depends on grain size, composition, temperature, cation distribution and preparation condition.

The super exchange interactions in antiferromagnetic materials may cause magnetic disorderness and frustrations at lower temperature and the system shows a low temperature spin glass or re-entrant spin glass (RSG) behavior [16-19]. In the RSG two transitions are expected. One at high temperature another is low temperature. Several concepts have been developed in order to understand the properties of disordered magnetic phases.

Scientists are continuing their effort to achieve the optimum parameters of ferrites, like high *Ms*, high permeability, high resistivity, low eddy current loss, etc. Since the research on ferrites is so vast, it is difficult to collect all experimental results and information about all types of ferrites in every aspect. The systematic research is still necessary for more comprehensive understanding of such materials.

Many researchers have studied the effect of Gd on the various properties of Ni-ferrite [20], Co-ferrite [21], Ni-Cu-Zn ferrite [22]. To the best of our knowledge, no literature is available on the structural and magnetic properties of Gd substitution of $Co_{0.40}Cu_{0.20}Zn_{0.40}Gd_xFe_{2-x}O_4$. In this present research, Gd^{3+} substituted $Co_{0.40}Cu_{0.20}Zn_{0.40}Gd_xFe_{2-x}O_4$ will be prepared and characterized.

1.2 Motivation of this Research

The history of magnetism began with the discovery of the properties of magnetite (Fe_3O_4), which is called ferrite. The use of ferrites has become established in many branches of telecommunication and electronic engineering and they now embrace a very wide diversity of composition, properties and applications. The Néel propose that in ferrimagnetic materials, the opposing moments are unequal and a spontaneous magnetization remains. There were still two different lattice sites i.e. *A* and *B* sublattices, respectively and have opposite types of magnetic moment. The most common example is Fe_3O_4. It has been found that for this particular ferrite, one Fe^{3+} ion occupies *A*-site while the Fe^{3+} and Fe^{2+} ions occupy *B*-sites. The net magnetic moment of Fe_3O_4 is therefore, equal to the magnetic moment of Fe^{2+} ion. Ferrimagnetic materials have spontaneous magnetization below the T_N, and show no magnetic order (are paramagnetic) above this temperature. However, there is sometimes a temperature below the T_N at which the two sublattices have equal moments, resulting in a net magnetic moment of zero; this is called the magnetization compensation point. This compensation point is observed easily in garnets and rare earth-transition metal alloys. Some ferrimagnetic materials are YIG (yttrium iron garnet) and ferrites composed of iron oxides and other elements such as aluminum, cobalt, nickel, manganese and zinc. In the last two decades, latest advancement in wireless technology has explored the area of real-time communication [23]. Internet-accessible cell phones and high-speed wireless local area network are the best examples of this technology. The core of this systems is based on a radio frequency (RF) circuit consisting of transmission and receiving circuit blocks required in signal amplification, filtering modulation that in turn require hundreds of passive chip components such as capacitors and inductors. Inductors adapted to RF circuits of

mobile device are mostly multilayer chip inductors (MLCIS). Materials with high permeability are also required for reducing the number of layers in MLCIs and for realizing the better miniaturization [24, 25]. The electrical properties and structure of spinel ferrite are closely related. There are different mechanisms available in literature to explain the electrical transport properties. In one of the report Koops proposed that the high permittivity of ferrite is attributed to the conductivity inhomogeneity between grains and grain boundaries [26]. The electrical conductivity and dielectric behavior of ferrites depend on chemical composition, grain size or structure and preparation conditions. Studies the effect of temperature, composition and frequency on the dielectric behavior and ac electrical conductivity offer valuable information about conducting phenomenon in ferrites based on localized electric charge carriers. Electron hopping is known to be a mechanism for both conduction and polarization in ferrites.

Ferrites are extensively studied materials because of their several interesting physical properties. They have high resistivity, and anisotropic properties. The anisotropy is actually induced by an external applied field. When this applied field aligns with the magnetic dipoles it causes a net magnetic dipole moment and causes the magnetic dipoles to precess at a frequency controlled by the applied field, called Larmor or precession frequency. As a particular example, a microwave signal circularly in the same direction as this precession strongly interacts with the magnetic dipole moments; when it is polarized in the opposite direction the interaction is very low. When the interaction is strong, the microwave signal can pass through the material. This directional property is used in the construction of microwave devices like isolators, circulators and gyrators. Ferrimagnetic materials are also used to produce optical insulators and circulators.

The crystal structure is expected to change due to the substitution of Gd in $Co_{0.40}Cu_{0.20}Zn_{0.40}Gd_xFe_{2-x}O_4$. Due to the structural change there may be a variation of magnetic interaction between A-site and B-site cations and hence a change of magnetic properties is also expected in $Co_{0.40}Cu_{0.20}Zn_{0.40}Gd_xFe_{2-x}O_4$. Better quality materials are expected in terms of magnetization, initial permeability and microstructure. At present, Bangladesh is very dependent on the imported ferrite cores and other soft magnetic materials. If we develop a high quality ferrite with desired characteristics in our country, importation can be stopped that will save foreign currency.

1.3 Objectives with specific aims

Ferrite is especially convenient for high frequency application because of its high resistivity. The mechanism of eddy current losses and damping of domain wall motion can be understood from the relative magnitudes of the real and imaginary parts of the complex initial permeability.

The main objectives of the present research are as follows:

- To synthesize spinel $Co_{0.40}Cu_{0.20}Zn_{0.40}Gd_xFe_{2-x}O_4$ with x= 0.0, 0.025, 0.050, 0.075, 0.100 samples by conventional solid state reaction technique. Various samples prepared from these powders have been sintered at different temperatures.
- Structural characterization has been performed by X-ray diffraction (XRD). From the XRD results lattice parameter, density and porosity of all compositions are determined.
- From microstructural analysis, the average grain sizes of all compositions have been measured to investigate the influence of grain size on the domain

wall motion, density and porosity of the above mentioned compositions through the Scanning Electron Microscopy (SEM) studies.

- To study the frequency dependents complex permeability (20 Hz-120 MHz).of each composition has been measured with Wayne Kerr Electronics Precision impedance analyzer.
- To study the magnetic properties of various $Co_{0.40}Cu_{0.20}Zn_{0.40}Gd_xFe_{2-x}O_4$ through studying the electrical properties of various compositions by observing complex impedance spectra and Vibrating Sample Magnetometer (VSM) spectroscopy.
- To understand the transport properties of various compositions through studying the electrical properties such as AC conductivity and dielectric properties viz. dielectric constant and dielectric loss over a range of frequency (20Hz-120MHz).

1.4 Outline of the Thesis

The thesis has been divided into six chapters:

Chapter- 1 discusses about brief introduction of our present composition and objective of our research.

Chapter- 2 which is the review of the pertinent work done in fast and their important remarks. Also this chapter gives theoretical background as well as crystal structure of the spinel type ferrites.

Chapter - 3 the preparation of the sample is described here. The details of the every sample preparations are given.

Chapter- 4 gives descriptions of different experimental set up of all instruments and their usage is also described. The working principle of the instrument, their calibration and how to measurement are taken is also given.

Chapter- 5 is devoted to the results of various investigations of the study and a brief discussion is also given here. How a property changes depending on frequency or others, why it changes are all described. The all description is based on the early works and new thoughts and ideas are also given.

Chapter- 6 The conclusions drawn from the overall experimental results and of our present work are given in this chapter. And suggestion for the future work is also given here. Reference of the authors for each remark is enlisted at the end of each chapter.

11 References

[1] Dascalu, G., Popescu, T., Feder, M., Caltun, O. F., "Structural, electric and magnetic properties of $CoFe_{1.8}RE_{0.2}O_4$ (RE=Dy, Gd , La) bulk materials", J. Magn. Magn. Mater. Vol. 333, pp. 69-74, 2013.

[2] Hankare, P. P., Patil, R. P., Garadkar, K. M., Sasikala,R., Chougule, B. K., " Synthesis, dielectric behavior and impedence measurement studies of Cr-substituted Zn-Mn ferrites", Mater. Res. Bull. Vol. 46, pp. 447-452, 2011.

[3] Rahaman,A. U., Rafiq, M. A., Maaz, K., Karim, S., Sung Oh Cho., Hasan, M. M.,"Temparature induced delocalization of charge carriers and metallic phase in $Co_{0.6}Sr_{0.4}Fe_2O_4$ nanoparticles", J. Appl. Phys. Vol. 112, pp. 063718, 2012.

[4] Muthu, K. S., Lakshminarasimh, N.," Impedance spectroscopic studies on $NiFe_2O_4$ with different morphologies: microstructure vs. dielectric properties", Ceram. Int. Vol. 39, pp. 2309, 2013.

[5] Parvin, Roksana, Momin, A. A., and Hossain, A. K. M. A., "Improvement of microstructure, initial permeability, magnetization and dielectric properties of nanocrystalline $Li_xCu_{0.1}Co_{0.1}Zn_{0.8-2x}Fe_{2+x}O_4$", J. Magn. Magn. Mater. Vol. 401, pp.760-769, 2016.

[6] Leung, L. K., Evans, B. J., Morish, A.H., Phys. " Low- Temparature Mossbauer Study of a Nikel Zink Ferrite": $Zn_xNi_{1-x}Fe_2O_4$ Rev. Vol. 8(1), pp. 29-34, 1973.

[7] Rahman, M. A., Rahman, M. A., & Hossain, A. A., "Effect of Cu^{2+} substitution on structural, magnetic and transport properties of $Fe_{2.5}Zn_{0.5}Cu_xO_4$", J. Magn. Magn. Mater. Vol. 369, pp. 168–175, 2014.

[8] Paulsen, J. A., Ring, A. P., Lo, C. C. H., Snyder, J. E., Jiles, D. C., " Manganese-substituted cobalt ferrite magnetostrictive materials for magnetic stress sensor applications", J. Appl. Phys. Vol. 97, pp. 044502, 2005.

[9] Caltun, O. F., Dumitru, I., Feder, M., Lupu, N., Chiriac, H., "Substituted cobalt ferrites for sensors applications," J. Magn. Magn. Mater. Vol. 5, pp. 45–47, 2007.

[10] Boutiuc, L. M., Dumitru, I., Caltun, O. F., Feder, M., Vilceanu, V., "Coprecipitated cobalt ferrite for sensors," Sensor Letters, Vol. 7, pp. 244–246, 2009.

[11] Lo, C. C. H., Ring, A. P., Snyder, J. E., Jiles, D. C., "Improvement of magnetomechancial properties of cobalt ferrite by magnetic annealing," IEEE Transactions on Magnetics," vol. 41, pp. 3676–3678,2005.

[12] Barbosa, J., Almeida, B. G., Mendes, J. A., Rolo, A. G., Araujo, J. P., Sousa, J., B., "Nanogranular $BaTiO_3$–$CoFe_2O_4$ thin films deposited by pulsed laser ablation", J. Appl. Phys. Vol. 101, pp. 09M101, 2007.

[13] Duong, G. V., et al., "Monodispersed Nanocrystalline $Co_{1-x}Zn_xFe_2O_4$ particles by forced hydrolysis: Synthesis and characterization", J. Magn. Magn. Mater. Vol. 311, pp. 46-50, 2007.

[14] Goldman, A., "Modern Ferrites Technology" 2nd Edition, Pittsburgh, PA, USA, 1999.

[15] Valenzuela, R., "Magnetic Ceramics", Cambridge University Press, Cambridge, 1994.

[16] Bhargava, S C., Morrish, A H., unkel, H. K., and Li, Z. W., "Spin-glass ordering in a spinel ferrite, $Mg(Al,Fe)_2O_4$" J. Phys. Condens. Matter. Vol. 12, pp. 9667–9687, UK, 2000.

[17] Binder, K., Young, A. P., "Spin glasses: Experimental facts, theoretical concepts, and open questions" Rev. Mod. Phys., Vol. 58, pp. 801-976, 1986

[18] Mydosh, J. A., "Spin Glasses: An Experimental Introduction", Taylor and Francis, London Washington, DC, 1993.

[19] Chengyi Hou, Hao Yu, Qinghong Zhang, Yaogang Li, Hongzhi Wang, "Preparation and magnetic property analysis of monodisperse Co–Zn ferrite nanospheres", J. Alloys Compd., Vol. 491, pp. 431–435, 2010.

[20] Bharathi, K. K., and Markandeyulu, G.,"Ferroelectric and ferromagnetic properties of Gd substituted nickel ferrite", J. Appl. Phys. Vol. 103, pp. 07E309 (01-03), 2008.

[21] Kumar, P., Chand, J., Verma, S., Singh, M., "Micro-structural studies of Gd doped Cobalt ferrite," International journal of theoretical and applied science", Vol. 3(02), pp. 10-12, 2011.

[22] Jadav, G. B., and Jadav, K. M., "Effect of gadolinium doped on electrical properties of Ni-Zn-Cu ferrite", Indian streams research journal. Vol. 3, pp. 1-4, 2013.

[23] Kim, K. Y., Kim, W. S., Ju, Y. D. and Jung H. J., "Effect of addition of the CoO-Fe_2O_3 system on the electromagnetic wave absorbing properties of sintered ferrite" J. Mater., Sci., Vol. 27, pp. 4741–4745, 1992.

[24] Qi, X. W., Zhou, J., Yue, Z., Gui, Z. L., Li, L. T., "Effect of Mn substitution on the magnetic properties of MgCuZn ferrites", J. Magn. Magn. Mater. Vol. 251, pp. 316-322, 2002.

[25] Nakamura, T., "Snoek's limit in high-frequency permeability of polycrystalline Ni-Zn, Mg-Zn, and NiCuZn spinel ferrites", J. Appl. Phys. Vol. 88, pp. 348-353, 2000.

[26] Koops, C. G., "On the dispersion of Resistivity and dielectric constant of Some Semiconductor at Audio frequencies", Phys. Rev., Vol. 83, pp. 121-124, 1951.

CHAPTER 2

LITERATURE REVIEW

2.1 Overview of the Materials

Ferrites materials with spinel or inverse spinel structure are the most technological important ferrimagnetic compounds derived from iron oxides such as magnetite (Fe_3O_4) as well as combination of other divalent metal oxides and trivalent iron oxide [1]. Ferrites commonly expressed by the general chemical formula $MeO.Fe_2O_3$, where *Me* represents divalent metals, first commanded the public attention when Hilbert (1909) focused on the usefulness of ferrites at high frequency [2]. A systematic investigation was launched by Snoek (1936) at Philips Research Laboratory [3]. At the same time Takai (1937) in Japan was seriously engaged in the research work on the same materials [2]. Snoek's extensive works on ferrites unveiled many mysteries regarding magnetic properties of ferrites. He was particularly looking for high permeability materials of cubic structure. This particular structure for symmetry reasons supports low crystalline anisotropy. He found suitable materials in the form of mixed spinel‟s of the type $MeZnFe_2O_4$, where *Me* stands for metals like *Cu*, *Mg*, *Ni, Co* or *Mn*, for which permeability were found to be up to 4000 [2-3, 4].

They are quite important because of their established correlations between polycrystalline structures, magnetic properties and the recent applications, such, as permanent magnets, high frequency transformer, magnetic recording heads, switching devices, radar as well as magneto-optic recording materials [5, 6-8]. Ferrites have also attracted a great amount of attention because of their magnetic behavior and their applications in power electronics devices from the radio frequency (300 kHz to 3 MHz) to the microwave frequency (3 MHz to 20 GHz) [9]. Particularly, cobalt-based ferrites are known to be a good candidate for high frequency devices, memory core

and magnetic recording media because of their unique physical properties such as high coercive force (H_c), moderate saturation magnetization (M_s), high Néel temperature (T_N), high resistivity, negligible eddy current losses, chemical stability and mechanical hardness [10-12]. Since the research on ferrites is so vast, it is difficult to collect all experimental results and information about all types of ferrites in every aspect. The systematic research is still necessary for more comprehensive understanding of such materials.

Many researchers have investigated the structural, magnetic and electrical properties of *Zn* substituted *Co*-ferrites [13-16]. In our laboratory Hossain *et al.* studied frequency dependence permeability of $Co_{0.60}Zn_{0.40}Fe_2O_4$ and $Co_{0.80}Zn_{0.20}Fe_2O_4$ [17]. Khan *et al.* [18] Reentrant spin glass behavior and large initial permeability of $Co_{0.5-x}Mn_xZn_{0.5}Fe_2O_4$ by solid state reaction technique. Azizi *et al.* [19] studied phase formation and change of magnetic properties of $Ni_{0.5}Co_{0.5}Fe_2O_4$ by annealing. They reported that *Hc* of annealed powders reduced and *Ms* increased with annealing temperature. They observed that cobalt ions in *B*-sites of cobalt doped nickel ferrite structure induce more magnetic anisotropy than nickel ferrite so. *Hc* is increased by doping cobalt in nickel ferrite. Structural, magnetic and dielectric properties of $Co_{0.5}Zn_{0.5}Fe_2O_4$ prepared by mechanical alloy and sintering process were studied by Waje *et al.* [20].They observed single phase cubic spinel with the lattice constant „a_0" to be in the range 0.841–0.842 nm, which is within the range of the theoretical *a0* values of 0.833 and 0.839 nm for zinc and cobalt ferrite, respectively. They reported effect of sintering temperature and frequency on initial permeability and it decreased after attaining the natural resonance frequency (200 MHz) of the material. The rare earth substituted different ferrites are becoming the promising materials for different applications. Addition of small amount of rare earth ions to

ferrite samples produces a change in their magnetic and electrical as well as structural properties depending upon the type and the amount of rare earth elements used. Rare earth ions can be divided into two categories: one with the radius closes to Fe ions; while the other with ionic radius larger than Fe ions [21]. The difference in their ionic radii will lead to micro strains, which may cause domain wall motion resulting in deformation of the spinel structure [22]. It has been stated that the rare earth ions commonly reside at the octahedral sites by replacing Fe^{3+}ions and have limited solubility in the spinel lattice due to their large ionic radii [23].

Ferrimagnetism in ferrite is largely governed by Fe-Fe interaction (the spin coupling of the 3d electrons). If the rare earth ions enter the spinel lattice, the RE-Fe interactions also appears (4f-3d coupling), which can lead to changes in the magnetization and Curie temperature [24]. The rare earth oxides are good electrical insulators and have resistivities at room temperature greater than 106 Ω-cm [25]. Rare earth ion forms the orthoferrite phase ($REFeO_3$).The occupation of RE ions on „B‟ sites impedes the motion of Fe^{2+}in the conduction process in ferrite, thus causing an increase in resistivity [26].

Many investigators have been carried out on the influence of different rare earth atoms (La, Sm, Gd, Nd, Dy, Tb, Ce, Th, Y, Eu) on the properties of ferrites. The results of these researches show that different rare earth atoms behave differently in spinel ferrite. Rezlescu et al. [27] investigated the effect of Fe replacement by RE (Yb, Er, Sm, Tb, Gd, Dy and Ce) ions on the properties of $(Ni_{0.7}Zn_{0.3})$ Fe_2O_4 ferrite. The results showed that the electrical resistivity of a ferrite increased by substituting a small quantity of Fe_2O_3 with RE_2O_3. Many physical of polycrystalline ferrites are very sensitive to the microstructure. The bulk (grain) and grain boundary are the two main components that determine the microstructure. Thus The information about the

associated physical parameters of the components that constitute the microstructure is important in understanding the overall properties of the materials. The electrical properties and microstructure of spinel ferrite are closely related. The bulk materials in ferrites are assume to be constituted o highly conducting grains separated by low conducting grain boundaries [28].

Jacobo et al. [29] worked on $(Zn_{0.5}Ni_{0.5})RE_{0.02}Fe_{1.98}O_4$ ferrites, with RE = Y, Gd and Eu. The results showed a small increase in the hyperfine field parameters and a strong decrease of the total resonant area with respect to the pure NiZn ferrite. Curie temperatures decreased and coercive fields increased with substitution. By adding much large ionic radii rare earth ions resulted in local distortion and disorder, enough to induce a softening of the network (s electron density).

Zhao et al. [30] reported influence of Gd on magnetic properties of $(Ni_{0.7}Mn_{0.3})$ $Gd_xFe_{2-x}O4$ferrites. It was found the crystallite sizes decreased when Gd ions were doped into NiMn ferrites. With Gd-substitution, when x>0.06 all Gd ions could not enter into the ferrite lattice but resided at the grain boundary. The maximum content of Gd^{3+}ions in ferrite lattices was substituted when x = 0.06. The values of Hc and Ms were zero for all the samples calcined at 600°C. In addition, the Hc and Ms values of the samples calcined at 800°C were larger than those sintered at 850°C, with Gd contents less than 0.08. Whereas, when the Gd contents at x = 0.08 and x = 0.10, the Hc and Ms values of the samples increased with the calcination temperatures.

Sun et al. [31] reported the effect of Fe substitution by La and Gd on the structure, magnetic, and dielectric properties of $(Ni_{0.5}Zn_{0.5}Fe_{2-x})$ RE_xO_4ferrites. It was found that the relative density of sintered bodies decreased and the lattice parameter increased with increasing RE ion substitution. La and Gd both tend to increase the cut-off frequency, decrease the initial permeability and magnetic loss tangent (tanδ)

which could be explained by a combination of low density, small grain size, secondary phase (REFeO3) formation, and more lattice defects. The low tanδ values resulted mainly from the reduction in eddy current loss due to the higher electrical resistivity with increasing RE ion.

Tasaki *et al.* [32] studied the effect of sintering atmosphere on permeability of sintered ferrite. They found that high density is one of the factors, which contribute to greater permeability. However, permeability decreased in an atmosphere without O_2 at high sintering temperature where high density was expected. This decrease in permeability is attributed to the variation of chemical composition caused by volatilization of *Zn*. At low sintering temperature a high permeability is obtained in an atmosphere without O_2 because densification and stoichiometry plays a principal role in increasing permeability. At high sintering temperature the highest permeability is obtained in the presence of O_2 because the effect of decrease of *Zn* content can then be neglected. Studying the electromagnetic properties of ferrites, Nakamura [33] suggested that both the sintering density and the average grain size increased with sintering temperature. These changes were responsible for variations in magnetization, initial permeability and electrical resistivity. High permeability attainment is certainly affected by the microstructure of the ferrites. Roess showed that [34] the very high permeability is restricted to certain temperature ranges and the shapes of permeability versus temperature curves are strongly affected by any inhomogeneity in the ferrite structure.

Leung *et al*. [35] performed a Low-temperature Mössbauer study of a nickel-zinc ferrite: $Zn_{1-x}Ni_xFe_2O_4$. They found that for $x \leq 0.5$ the resultant *A*- and *B*- site *Fe*-spin moments have a collinear arrangement, whereas for $x > 0.5$ a non-collinear arrangement of *A*- and *B*-site *Fe*-spin moments exist. An explanation based on the

relative strength of the exchange constant J_{AB} and J_{BB} is given to account for this difference. Rezlescu *et al.* [21] reported that the sintering behavior and microstructure of the ferrites samples largely affected by *PbO* addition. *PbO* significantly reduced the sintering temperatures, thus energy consumption is minimized and material loss by evaporation is minimized [36].

There are two mechanisms in the phenomenon of permeability; spin rotation in the magnetic domains and wall displacements. The uncertainty of contribution from each of the mechanisms makes the interpretation of the experimental results difficult. Globus [37] shows that the intrinsic rotational permeability μ_r and wall permeability μ_w may be written as: $\mu_r = 1 + 2\pi M_s^2 / K$ and $\mu_w = 1 + 3\pi M_s^2 D / 4\gamma$, where M_s is the saturation magnetization, K is the total anisotropy, D is the grain diameter and $\gamma \equiv K\delta_w$ is the wall energy.

El-Shabasy [38] studied the DC electrical resistivity of $Zn_xNi_{1-x}Fe_2O_4$ ferrites. He shows that the ferrite samples have semiconductor behavior where DC electrical resistivity decreases on increasing the temperature. $\rho(T)$ for all samples follows $\rho(T) = \rho_0 \exp(E/k_BT)$, where E is the activation energy for electric conduction and ρ_0 is the pre-exponential constant or resistivity at infinitely high temperature. The DC resistivity, $\rho(T)$, decreases as the *Zn* ion substitution increases. It is reported that *Zn* ions prefer the occupation of tetrahedral (*A*) sites; *Ni* ions prefer the occupation of octahedral (*B*) sites while *Fe* ions partially occupy the *A* and *B* sites. On increasing *Zn* substitution (at *A* sites), the *Ni* ion concentration (at *B* sites) will decrease. This lead to the migration of some *Fe* ions from *A* sites to *B* sites to substitute the reduction in *Ni* ion concentration at *B* sites. As a result, the number of ferrous and ferric ions at *B* sites (which is responsible for electric conduction in ferrites) increases.

Consequently ρ decreases on *Zn* substitution. Another reason for the decrease in ρ on increasing *Zn* ion substitution is that, zinc is less resistive ($\rho = 5.92\ \mu\Omega cm$) than nickel ($\rho = 6.99\ \mu\Omega cm$). The main conductivity mechanism in ferrites is attributed to electron hopping between Fe^{3+} and Fe^{2+} in octahedral sites. Resistivity in spinel"s is very sensitive to stoichiometry; a small variation of *Fe* content in $Zn_{0.7}Ni_{0.3}Fe_{2+x}O_{4-y}$ results in resistivity variations of $\sim 10^7$. Excess *Fe* can easily dissolve in spinel phase by a partial reduction of *Fe* from $3Fe_2^{3+}O_3$ to $2Fe^{2+}Fe_2^{3+}O_4$ (and $1/2O_2 \uparrow$) [3].

2.2 Magnetic Ordering

The onset of magnetic order in solids has two basic requirements:

(i) Individual atoms should have magnetic moments (spins),

(ii) Exchange interactions should exist that couple them together.

Magnetic moments originate in solids as a consequence of overlapping of the electronic wave function with those of neighboring atoms. This condition is best fulfilled by some transition metals and rare-earths. The exchange interactions depend sensitively upon the inter-atomic distance and the nature of the chemical bonds, particularly of nearest neighbor atoms. When the positive exchange dominates, which corresponds to parallel coupling of neighboring atomic moments (spins), the magnetic system becomes ferromagnetic below a certain temperature T_C called the Curie temperature. The common spin directions are determined by the minimum of magneto-crystalline anisotropy energy of the crystal. Therefore, ferromagnetic substances are characterized by spontaneous magnetization. But a ferromagnetic material in the demagnetized state displays no net magnetization in zero field because in the demagnetized state a ferromagnetic of macroscopic size is divided into a

number of small regions called domains, spontaneously magnetized to saturation value and the directions of these spontaneous magnetization of the various domains are such that the net magnetization of the specimen is zero. The existence of domains is a consequence of energy minimization. The size and formation of these domains is in a complicated manner dependent on the shape of the specimen as well as its magnetic and thermal history. When negative exchange dominates, adjacent atomic moments (spins) align antiparallel to each other, and the substance is said to be anti-ferromagnetic below a characteristic temperature, T_N, called the Néel temperature. In the simplest case, the lattice of an anti-ferromagnet is divided into two sublattices with the magnetic moments of these in anti-parallel alignment. This result is zero net magnetization. A special case of anti-ferromagnetism is ferrimagnetism. In ferrimagnetism, there are also two sublattices with magnetic moments in opposite directions, but the magnetization of the sublattices are of unequal strength resulting in a non-zero magnetization and therefore has net spontaneous magnetization. At the macroscopic level of domain structures, ferromagnetic and ferrimagnetic materials are therefore similar.

The Curie and Néel temperatures characterize a phase transition between the magnetically ordered and disordered (paramagnetic) states. From these simple cases of magnetic ordering various types of magnetic order exists, particularly in metallic substances. Because of long-range order and oscillatory nature of the exchange interaction, mediated by the conduction electrons, structures like helical, conical and modulated patterns might occur. *A* useful property for characterizing the magnetic materials is the magnetic susceptibility,χ, defined as the magnetization, M, divided by the applied magnetic field, H i.e. $\chi = M / H$. The temperature dependence of susceptibility or, more accurately, inverse of susceptibility is a good characterization

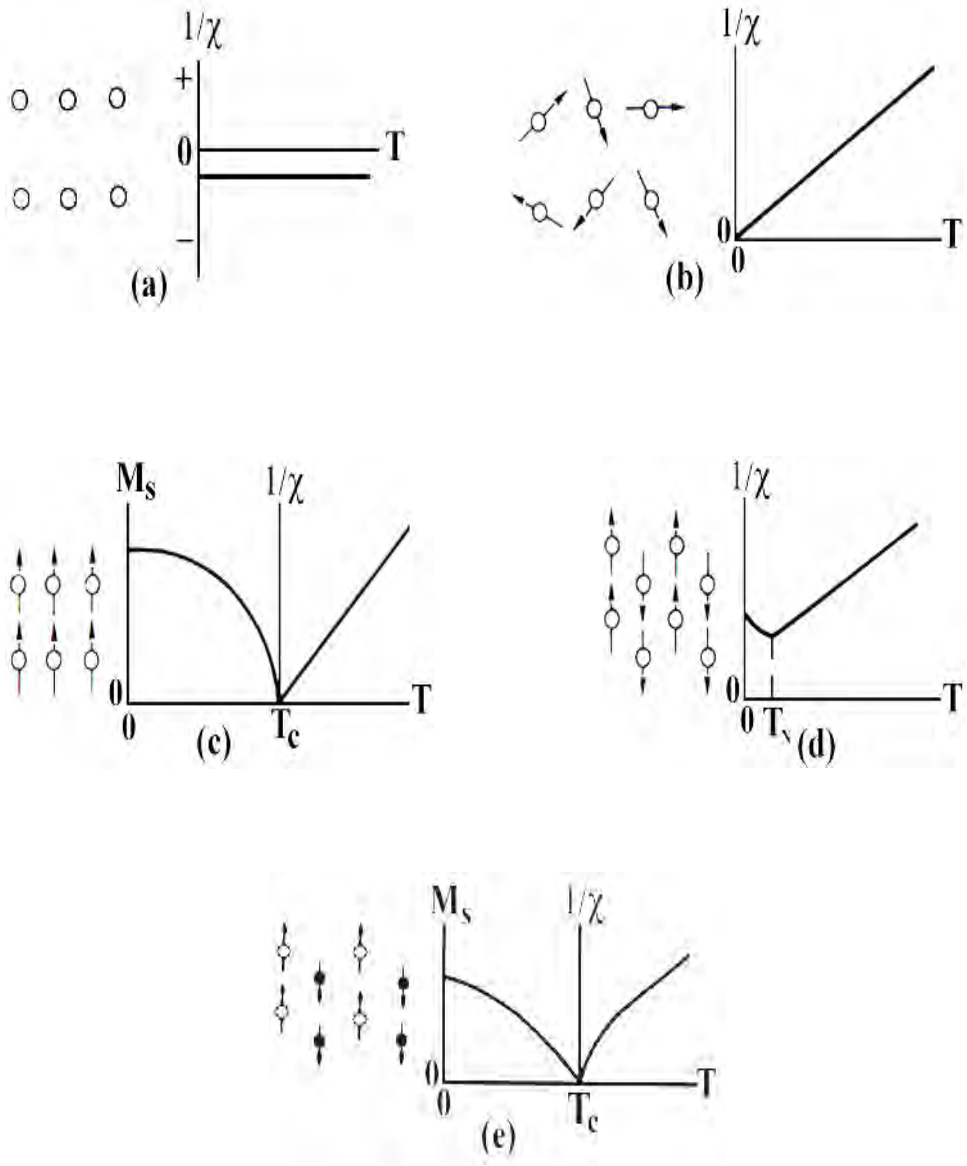

Fig.2.1 Temperature dependence of the inverse susceptibility for: (a) a diamagnetic material; (b) a paramagnetic material, showing Curie"s law behavior; (c) a ferromagnetic material, showing a spontaneous magnetization for $T<T_C$ and Curie-Weiss behavior for $T>T_C$; (d) an antiferromagnetic material; (e) a ferrimagnetic material, showing a net spontaneous magnetization for $T<T_C$ and nonlinear behavior for $T>T_C$.

parameter for magnetic materials, Fig. 2.1(e) shows that in the paramagnetic region, the variation of the inverse susceptibility with temperature of a ferrite material is decidedly non-linear. Thus the ferrite materials do not obey the Curie-Weiss law, $\chi = C/(T - T_C)$ [3,39].

2.3 Crystal Structure of Spinel Ferrites

2.3.1 Ionic Charge Balance and Crystal Structure of Cubic Spinel Ferrite

The spinel lattice is composed of a close-packed oxygen arrangement in which 32 oxygen ions form a unit cell that is the smallest repeating unit in the crystal network. Between the layers of oxygen ions, if we simply visualize them as spheres, there are interstices that may accommodate the metal ions. Now, the interstices are not all the same; some which are called *A* sites are surrounded by or coordinated with 4 nearest neighboring oxygen ions whose lines connecting their centers form a tetrahedron. Thus, *A* sites are called tetrahedral sites (Fig. 2.2 (a)). The other type of site (*B* sites) is coordinated by 6 nearest neighbor oxygen ions whose center connecting lines describe an octahedron. The *B* sites are called octahedral sites (Fig. 2.2(b)). In the unit cell of 32 oxygen ions, there are 64 tetrahedral sites and 32 octahedral sites. If all of these were filled with metal ions, of either *+2* or +3 valence, the positive charge would be very much greater than the negative charge and so the structure would not be electrically neutral. It turns out that of the 64 tetrahedral sites, only 8 are occupied and out of 32 octahedral sites, only 16 are occupied. If, as in the mineral, spinel, the tetrahedral sites are occupied by divalent ions and the octahedral sites are occupied by the trivalent ions, the total positive charge would be 8x (+2) = +16 plus the 16x (+3) =+48 or a total of +64 which is needed to balance the 32x (-2) = -64 for the oxygen ions. There would then be eight formula units of $MO.Fe_2O_3$ or MFe_2O_4 in a unit cell. *A* spinel unit cell contains two types of sub cells. The two types of sub cells alternate in a three- dimensional array so that each fully repeating unit cell requires eight sub cells.

The crystallographic environments of the *A* and *B* sites are distinctly different.The unit cell contains so many ions that a two-dimensional drawing of the

complete cell would not be very informative. Instead we can consider a unit cell of edge *a*, to be divided into eight octants, each of edge *a*/2, as shown in Fig. 2.2(c). The four shaded octants have identical contents, and so do the four unshaded octants. The contents of the two lower-left octants in Fig. 2.2(c) are shown in Fig. 2.2(d). One tetrahedral site occurs at the center of the right octant of Fig. 2.2(d), and other tetrahedral sites are at some but not all octant corners. Four octahedral sites occur in the left octant; one is connected by dashed lines to six oxygen ions, two of which, shown dotted, are in adjacent octants behind and below. The oxygen ions are arranged in the same way, in tetrahedral, in all octants. Not all of the available sites are actually occupied by metal ions. Only one-eighth of the *A* sites and one-half of the *B* sites are occupied, as shown in Table 2.1 [3]. In the mineral spinel, $MgO.Al_2O_3$, the Mg^{2+} ions are in *A* sites and the Al^{3+}ions are in *B* sites.

Some ferrites $MO.Fe_2O_3$ have exactly this structure, with M^{2+} in *A* sites and Fe^{3+} in *B* sites. This is called the normal spinel structure. If 8 divalent (*M*) ions occupy the *A*-site i.e., tetrahedral site and 16 tetravalent ions (Fe^{3+}) occupy the *B*-site i.e., octahedral site, the structure is said to be Normal spinel.

If *B*-site i.e., octahedral site is occupied half by divalent metal ion and half by trivalent iron ions, generally distributed in random and *A*-site i.e., tetrahedral site by trivalent iron ions, the structure is said to be Inverse spinel. Both zinc and cadmium ferrite have this structure and they are both nonmagnetic, i.e., paramagnetic. Many other ferrites, however, have the inverse spinel structure, in which the divalent ions are on *B* sites, and the trivalent ions are equally divided between *A* and B sites. The divalent and trivalent ions normally occupy the B sites in a random fashion, i.e., they are disordered. Iron, cobalt, and nickel ferrites have the inverse structure, and they are all ferromagnetic.

The normal and inverse structures are to be regarded as extreme cases, because X-ray and neutron diffraction show that intermediate structures can exist. Thus manganese ferrite is almost, but not perfectly, normal; instead of all the Mn^{2+} ions being on *A* sites, a fraction 0.8 is on A sites and 0.2 on B sites. Similarly, magnesium ferrite is not quite inverse; a fraction 0.9 of the Mg^{2+} ions is on B sites and 0.1 on A sites. The distribution of the divalent ions on A and B sites in some ferrites can be altered by heat treatment; it may depend, for example, on whether the material is quenched from a high temperature or slowly cooled.

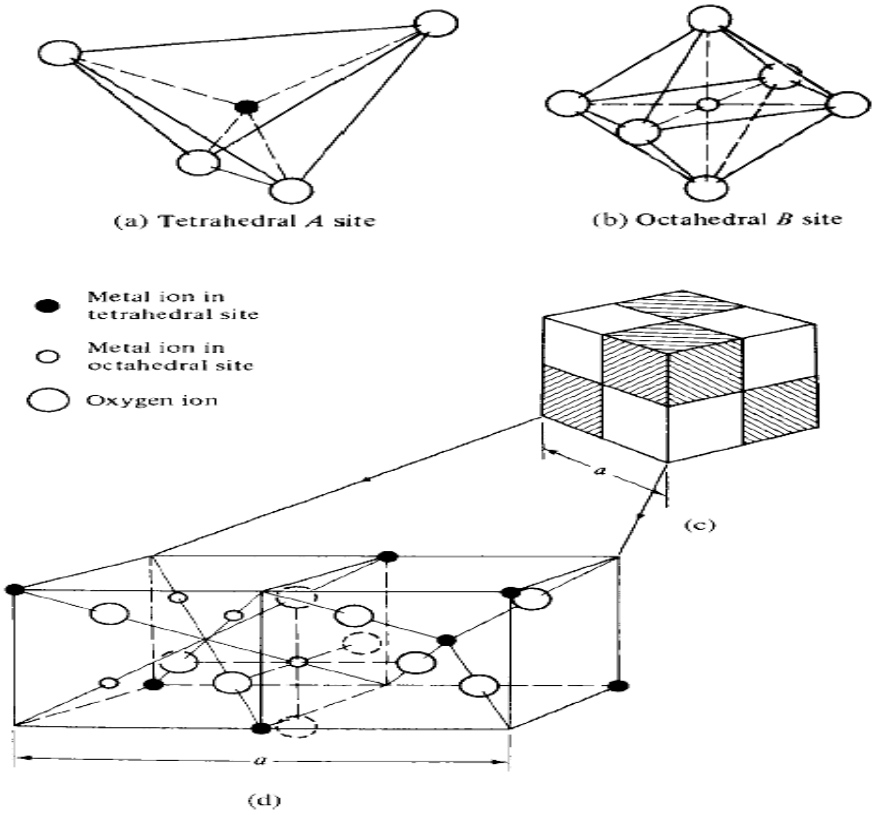

Fig.2.2 Crystal structure of a cubic ferrite [39].

The positions of the ions in the spinel lattice are not perfectly regular (as the packing of hard spheres) and some distortion does occur. The tetrahedral sites are often too small for the metal ions so that the oxygen ions move slightly to accommodate them. The oxygen ions connected with the octahedral sites move in such a way as to shrink

the size the octahedral cell by the same amount as the tetrahedral site expands. The movement of the tetrahedral oxygen is reflected in a quantity called the oxygen parameter, which is the distance between the oxygen ion and the face of the cube edge along the cube diagonal of the spinel subcell. This distance is theoretically equal to 3/8ao where ao is the lattice constant [2].

Table 2.1 Arrangements of Metal Ions in the Unit Cell of a Ferrite $MO.Fe_2O_3$ [39]

Kinds of sites	Number Available	Number Occupied	Occupants	
			Normal Spinel	Inverse Spinel
Tetrahedral (A)	64	8	$8M^{2+}$	$8\ Fe^{3+}$
Octahedral (B)	32	16	$16\ Fe^{3+}$	$8\ Fe^{3+}$ $8\ M^{2+}$

2.3.2 Site Preferences of the Ions

The preference of the individual ions for the two types of lattice sites is determined by;

1. The ionic radii of the specific ions
2. The size of the interstices
3. Temperature
4. The orbital preference for specific coordination

The most important consideration would appear to be the relative size of the ion compared to the size of the lattice site. The divalent ions are generally larger than the trivalent (because the larger charge produces greater electrostatic attraction and so pulls the outer orbits inward). The octahedral sites are also larger than the tetrahedral

[40]. Therefore, it is reasonable that the trivalent ions such as Fe^{3+} would go into the tetrahedral sites and the divalent ions would go into the octahedral. Two exceptions are found in Zn^{2+} and Cd^{2+} which prefer tetrahedral sites because the electronic configuration is favorable for tetrahedral bonding to the oxygen ions. Thus *Zn* takes preference for tetrahedral sites over the Fe^{3+} ions. Zn^{2+} and Co^{2+} have the same ionic radius but *Zn* prefers tetrahedral sites and Co^{2+} prefers octahedral sites because of the configurationally exception. Ni^{2+} and Cr^{3+} have strong preferences for octahedral sites, while other ions have weaker preferences [40].

2.3.3 Unit Cell Dimensions

The dimensions of the unit cell are given in Angstrom Units which are equivalent to 10^{-8} cm. If we assume that the ions are perfect spheres and we pack them into a unit cell of measured (X-ray diffraction) dimensions we find certain discrepancies that show that the packing is not ideal. The positions of the ions in the spinel lattice are not perfectly regular (as the packing of hard spheres) and some distortion does occur. The tetrahedral sites are often too small for the metal ions so that the oxygen ions move slightly to accommodate them. The oxygen ions connected with the octahedral sites move in such a way as to shrink the size of the octahedral cell by the same amount as the tetrahedral site expands .The movement of the tetrahedral oxygen is reflected in a quantity called the oxygen parameter which is the distance between the oxygen ion and the face of the cube edge along the cube diagonal of the spinel subcell. This distance is theoretically equal to $3/8a_o$. The unit cell length of *Li*-Ferrite, *Ni* ferrite and *Mg* Ferrite are observed to be 8.33 Å, 8.3390 Å and 8.36 Å respectively [3].

2.4 Cation Distribution of Spinel Ferrites

In spinel structure the distribution of cations over the tetrahedral or *A* sites and octahedral or *B* sites can be present in a variety of ways. If all the Me^{2+} ions in $Me^{2+}Me_2^{3+}O_4$ are in tetrahedral and all Me^{3+} ions in octahedral positions, the spinel is then called normal spinel. Another cation distribution in spinel exists, where one half of the cations Me^{3+} are in the *A* positions and the rest, together with the Me^{2+} ions are randomly distributed among the *B* positions. The spinel having the latter kind of cation distribution is known as inverse spinel. The distribution of these spinels can be summarized as [3, 41-42]

1) Normal spinels, i.e. the divalent metal ions are on *A*-sites: $Me^{2+}[Me_2^{3+}]O_4$,
2) Inverse spinels, i.e. the divalent metal ions are on *B*-sites: $Me^{3+}[Me^{2+}Me_2^{3+}]O_4$.

A completely normal or inverse spinel represents the extreme cases. There are many spinel oxides which have cation distributions intermediate between these two extreme cases and are called mixed spinel"s.

The general cation distribution for the spinel can be indicated as:

$$(Me_x^{2+}Me_{1-x}^{3+})[Me_{1-x}^{2+}Me_{1+x}^{3+}]O_4$$

where the first and third brackets represent the A and B sites respectively. For normal spinel x=1, for inverse spinel x=0. The quantity x is a measure of the degree of inversion. In the case of some spinel oxides x depends upon the method of preparation. The cation distributions of *Li*-Ferrite, *Mg*-Ferrite and *Ni*-Ferrite are shown below:

Li Ferrite : $(Fe^{3+})[Li_{0.5}Fe_{1.5}^{3+}]O_4$ [3,43]

Ni Ferrite : $(Fe^{3+})[Ni^{2+}Fe^{3+}]O_4$

Mg Ferrite $(Mg_{1-x}Fe^{3+})[Mg_x Fe_{2-x}{}^{3+}]\ O_4$

where x is the degree of inversion.

Both Li ferrite and Ni-Ferrite is a inverse spinel and Mg –Ferrite is a mixed ferrite.

The cation distribution of various $Li_xMg_{0.4}Ni_{0.6-2x}Fe_{2+x}O_4$ ferrite assumed as

$$\left(Fe^{3+}_{0.9}\right)[Li^{1+}_{x}Mg^{2+}_{0.4}Ni^{2+}_{0.6-2x}Fe^{3+}_{1.1+x}] \qquad [44]$$

The basic magnetic properties of the ferrites are very sensitive functions of their cation distributions. Mixed ferrites having interesting and useful magnetic properties are prepared by mixing two or more different types of metal ions. Spinel oxides are ionic compounds and hence the chemical bonding occurring in them can be taken as purely ionic to a good approximation. The total energy involved, however, consists of the Coulomb energy, the born repulsive energy, the polarization and the magnetic interaction energy. The energy terms are all dependent on lattice constant, oxygen position parameter and the ionic distribution. In principle the equilibrium cation distribution can be calculated by minimizing the total energy with respect to these variables. But the only energy that can be written with any accuracy is the Coulomb energy. The individual preference of some ions for certain sites resulting from their electronic configuration also play an important role. The divalent ions are generally larger than the trivalent (because the larger charge produces greater electrostatic attraction and so pulls the outer orbits inward). The octahedral sites are also larger than the tetrahedral. Therefore, it would be reasonable that the trivalent ions Fe^{3+} (0.73Å) would go into the tetrahedral sites and the divalent ions Fe^{2+} (0.86Å) go into the octahedral. Two exceptions are found in Zn^{2+} and Cd^{2+} which prefer tetrahedral sites because the electronic configuration is favorable for tetrahedral bonding to the oxygen ions. It is known that Li^{1+}(0.82Å), Ni^{2+}(0.73Å) and Mg^{2+}(0.80Å) ions occupy B sites [45]. Hence the factors influencing the distribution

the cations among the two possible lattice sites are mainly their ionic radii of the specific ions, the size of the interstices, temperature, the matching of their electronic configuration to the surrounding anions and the electrostatic energy of the lattice, the so-called Madelung energy, which has the predominant contribution to the lattice energy under the constrain of overall energy minimization and charge neutrality.

2.5 Interaction between Magnetic Moments on Lattice Sites

Spontaneous magnetization of spinels (at 0K) can be estimated on the basis of their composition, cation distribution, and the relative strength of the possible interaction. Since cation-cation distances are generally large, direct (ferromagnetic) interactions are negligible. Because of the geometry of orbital involved, the strongest superexchange interaction is expected to occur between octahedral and tetrahedral cations. The strength of interaction or exchange force between the moments of the two metal ions on different sites depends on the distances between these ions and the oxygen ion that links them and also on the angle between the three ions.

The nearest neighbours of a tetrahedral, an octahedral and an anion site are shown in Fig. 2.3. The interaction is greatest for an angle of 180^0 and also where the interionic distances are the shortest.

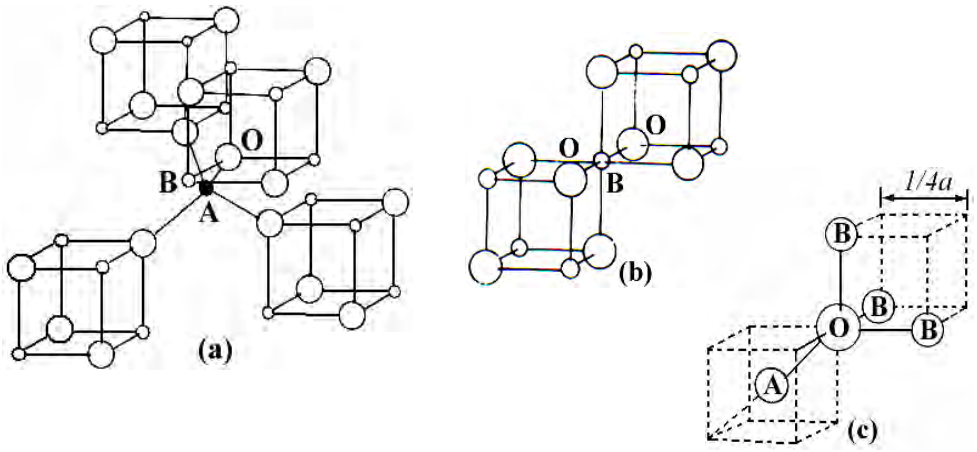

Fig.2.3 Nearest neighbors of (a) a tetrahedral site, (b) an octahedral site and (c) an anion site.

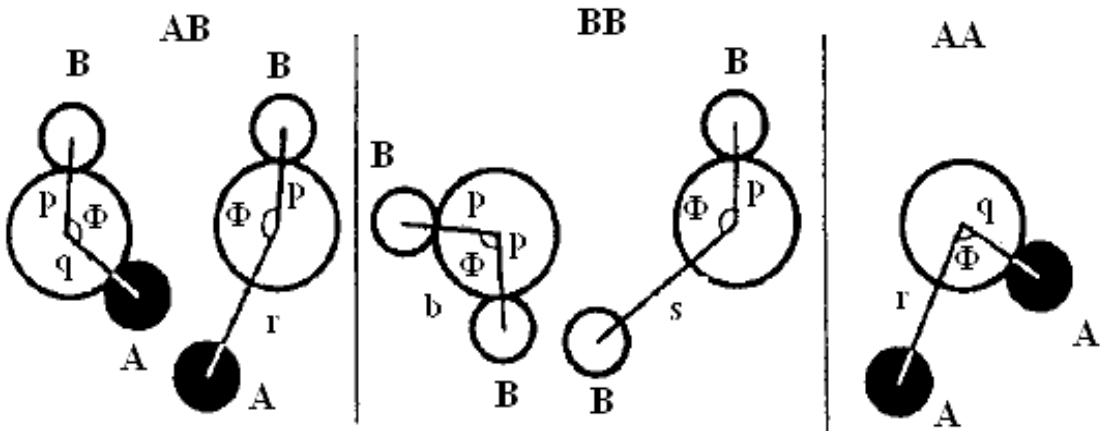

Fig.2.4 Interionic distances and angles in the spinel structure for the different type of lattice site interactions [40, 46].

Fig.2.4 shows the inter-atomic distances and the angles between the ions for the different types of interactions. In the A-A and B-B cases, the angles are too small or the distances between the metal ions and the oxygen ions are too large. The best combinations of distances and angles are found in the A-B interactions. For an undistorted spinel, the A-O-B angles are about 125^0 and 154^0 [2-3, 47]. The B-O-B angles are 90^0 and 125^0 but in the latter; one of the B-O distances is large. In the A-A case the angle is about 80^0. Therefore, the interaction between moments on the A and B sites is strongest. The B-B interaction is much weaker and the most unfavorable situation occurs in the A-A interaction. By examining the interactions involving the major contributor, or the A-B interaction which orients the unpaired spins of these ions antiparallel, Néel was able to explain the ferrimagnetism of ferrites The interaction between the tetrahedral and octahedral sites is shown in Fig. 2.4. An individual A site is interacted with a single B site, but each A site is linked to four such units and each B site is linked to six such units. Thus, to be consistent throughout the crystal, all A sites and all B sites act as unified blocks and are coupled antiparallel as blocks [40].

2.6 Magnetism in Spinel Ferrite:

The magnetic moment of a free atom is associated with the orbital and spin motions of electrons in an incomplete sub-shell of the electronic structure of the atom. In crystals the orbital motions are quenched, that is the orbital planes may be considered to be fixed in space relative to the crystal lattice, and in such a way that in bulk the crystal has no resultant moment from this source. Moreover this orbital-lattice coupling is so strong that the application of a magnetic field has little effect upon it. The spin axes are not tightly bound to the lattice as are the orbital axes. The anions surrounding a magnetic cation subject it to a strong inhomogeneous electric field and influence the orbital angular momentum. However, the spin angular momentum remains unaffected. For the first transition group elements this crystal field effect is intense partly due to the large radius of the 3d shell and partly due to the lack of any outer electronic shell to screen the 3d shell whose unpaired electrons only contribute to the magnetic moment. We have originally defined the magnetic moment in connection with permanent magnets. The electron itself may well be called the smallest permanent magnet [2]. For an atom with a resultant spin quantum number *S,* the spin magnetic moment will be

$$\mu = g\sqrt{S(S+1)}\mu_B$$

Where g is the Landé splitting factor and μ_B, known as the Bohr magneton, is the fundamental unit of magnetic moment. The value of g for pure spin moment is 2 and the quantum number associated with each electron spin is $\pm 1/2$. The direction of the moment is comparable to the direction of the magnetization (from South to North poles) of a permanent magnet to which the electron is equivalent.

Fig. 2.5 illustrates the electronic configuration of Fe atoms and Fe^{3+} ions. Fe atom has four unpaired electrons and ion has five unpaired electrons. Each unpaired electron spin

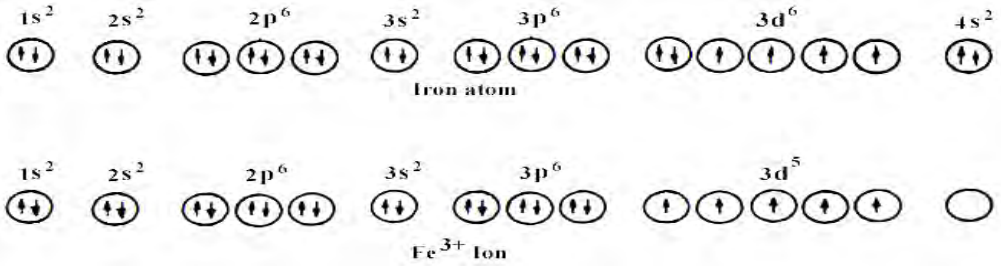

Fig.2.5 Electronic configuration of atoms and ions [40].

produced 1 Bohr magneton. In compounds, ions and molecules, account must be taken of the electrons used for bonding or transferred in ionization. It is the number of unpaired electrons remaining after these processes occur that gives the net magnetic moment [2]. According to the Hund"s rules the moment of *Fe* atom and Fe^{3+} ions are $4\mu_B$ and $5\mu_B$ respectively. Similarly the moment of $Fe^{2+}$and Ni^{2+} ion are $4\mu_B$ and $2\mu_B$ respectively.

2.6 .1 Magnetic Moments of Some Spinels Ferrites

2.6.1.1 Inverse Spinels:

In the nickel ferrite it was observed that the moments of the eight Ni^{2+} ions on the octahedral sites. The value of moment per Ni^{2+}ion is $2\mu_B$ or *16* μ_B for a unit cell containing eight formula units. The magnetic moments of the other inverse spinels can be predicted in a similar manner. These predicted values are listed in Table 2.2 along with the measured values [40]. Because the effect of thermal agitation on the magnetic moments will lower the magnetic moment, the correlation of the moment to Bohr magnetons is always referred to the value at absolute zero or 0^0K. This is usually done by extrapolation of the values at very low temperatures. The deviations from the theoretical values can be attributed to several factors, namely:

- The ion distribution on the various sites may not be as perfect as predicted.
- The orbital magnetic contribution may not be zero as assumed.
- The directions of the spins may not be antiparallel in the interactions. In other words, they may be canted.

2.6.2 Exchange Interactions in Spinel

The intense short-range electrostatic field, which is responsible for the magnetic ordering, is the exchange force that is quantum mechanical in origin and is related to the overlapping of total wave functions of the neighboring atoms. The total wave function consists of the orbital and spin motions. Usually the net quantum number is written as *S*, because the magnetic moments arise mostly due to the spin motion as described above. The exchange interactions coupling the spins of a pair of electrons are proportional to the scalar product of their spin vectors [48, 42, 49]

$$V_{ij} = -2J_{ij}\,\vec{S}_{i.}.\vec{S}_{j} \tag{2.1}$$

where J_{ij} is the exchange integral given in a self-explanatory notation by

$$J_{ij} = \int \psi_i^*(1)\psi_j^*(2)\left[\frac{1}{r_{12}} + \frac{1}{r_{ij}} - \frac{1}{r_{i1}} - \frac{1}{r_{j2}}\right]\psi_i(2)\psi_j(2)dv_1 dv_2 \tag{2.2}$$

In this expression r''s are the distances, subscripts *i* and *j* refer to the atoms, 1 and 2 refers to the two electrons. If the *J* in equation (2.1) is positive, we achieve ferromagnetism. A negative *J* may give rise to anti-ferromagnetism or ferrimagnetism.

Magnetic interactions in spinel ferrites as well as in some ionic compounds are different from the one considered above because the cations are mutually separated by bigger anions (oxygen ions). These anions obscure the direct overlapping of the cation charge distributions, sometimes partially and sometimes completely making the direct exchange interaction very weak. Cations are too far apart in most oxides for a direct cation-cation interaction. Instead, super-exchange interactions appear, i.e., indirect exchange via anion *p*-orbitals that may be strong enough to order the magnetic moments. Apart from the electronic structure of cations this type of interactions strongly depends on the geometry of arrangement of the two interacting cations and

the intervening anion. Both the distance and the angles are relevant. Usually only the interactions with in first coordination sphere (when both the cations are in contact with the anion) are important. In the Neél theory of ferrimagnetism the interactions taken as effective are inter- and intra-sublattice interactions *A-B*, *A-A* and *B-B*. The type of magnetic order depends on their relative strength.

The super-exchange mechanism between cations that operate via the intermediate anions was proposed by Kramer for such cases and was developed by Anderson and Van Vleck [48, 42]. A simple example of superexchange is provided by *MnO* which was chosen by Anderson. From the crystal structure of *MnO* it will be seen that the anti-parallel manganese ions are collinear with their neighbouring oxygen ions. The O^{2-} ions each have six *2p* electrons in three anti-parallel pairs. The outer electrons of the Mn^{2+} ions are in *3d* sub-shells which are half filled with five electrons in each. The phenomenon of super-exchange is considered to be due to an overlap between the manganese 3*d* orbits and the oxygen *2p* orbits with a continuous interchange of electrons between them.

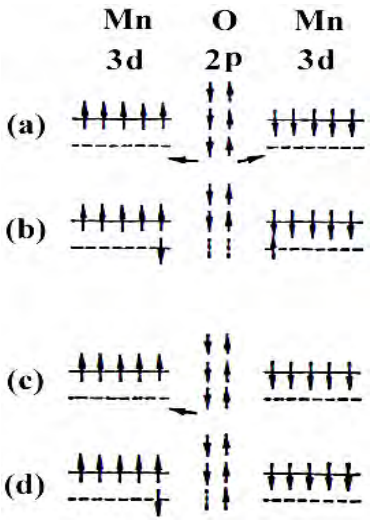

Fig.2.6 Illustrating super-exchange in *MnO*.

It appears that, for the overall energy of the system to be a minimum, the moments of the manganese ions on either side of the oxygen ion must be anti-parallel. The

manganese magnetic moments are thus, in effect, coupled through the intervening oxygen ion. The idea is illustrated in Fig. 2.6.

In Fig. 2.6 (a) and Fig. 2.6 (c) the outer electrons in a pair of Mn^{2+} ions, and in an intervening O^{2-} ion in the unexcited state, are shown by the arrows. One suggested mode of coupling is indicated in Fig. 2.6 (b). The two electrons of a pair in the oxygen ion are simultaneously transferred, one to the left and the other to the right. If their directions of spin are unchanged then, by Hund‟s rules, the moments of the two manganese ions must be anti-parallel as shown. Another possibility is represented in Fig. 2.6(d). One electron only has been transferred to the manganese ion on the left. The oxygen ion now has a moment of $1\mu_B$ and if there is negative interaction between the oxygen ion and the right-hand manganese ion then again the moments of the manganese ions will be anti-parallel. If these ideas are accepted then the oxygen ions play an essential part in producing anti-ferromagnetism in the oxide. Moreover, because of the dumbbell shape of the *2p* orbits, the coupling mechanism should be most effective when the metal ions and the oxygen ions lie in one straight line, that is, the angle between the bonds is 180˚, and this is the case with *MnO*.

In the case of spinel ferrites the coupling is of the indirect type which involves overlapping of oxygen wave functions with those of the neighboring cations. Consider two transition metal cations separated by an *O*, Fig. 2.7. The O^{2-} has no net magnetic moment since it has completely filled shells, with *p*-type outermost orbitals.

Orbital p_x has two electrons: one with spin up, and the other with spin down, consistent with pauli‟s exclusion principle. The essential point is that when an oxygen *p* orbital overlaps with a cation *d* orbital, one of the *p* electrons can be accepted by the cations. When one of the transition-metal cations is brought close the O^{2-}, partial electron overlap (between a *3d* electron from the cation and a *2p* electron form the O^{2-}

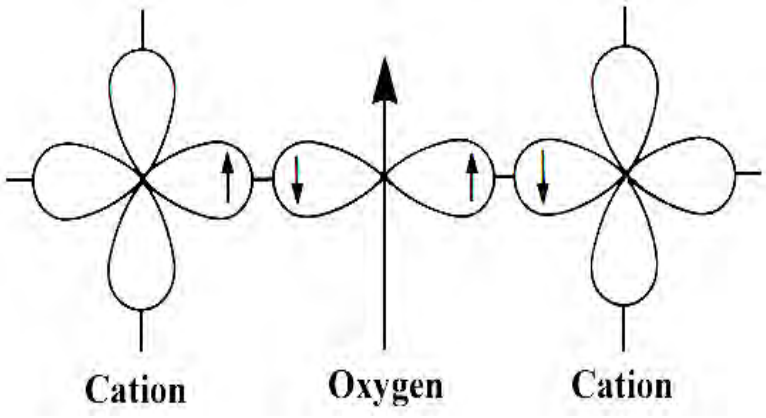

Fig.2.7 Schematic representation of the superexchange interaction in the magnetic oxides. The *p* orbital of an anion (center) interact with the *d* orbitals of the transitional metal cations.

) can occur only for anti-parallel spins, because electrons with the same spin are repelled. Empty *3d* states in the cation are available for partial occupation by the O^{2-} electron, with an anti-parallel orientation. Electron overlap between the other cation and the O^{2-} then occurs resulting in anti-parallel spins and therefore anti-parallel order between the cations. Since the *p* orbitals are linear, the strongest interaction is expected to take place for cation–O^{2-}–cation angles close to 180° [3].

2.6.3 Néel Theory of Ferrimagnetism

If we consider the simplest case of a two-sublattice system having antiparallel and non-equal magnetic moments, the inequality may be due to:

1) different elements in different sites,
2) same element in different ionic states, and
3) Different crystalline fields leading to different effective moments for ions having the same spin.

The spins on one sub-lattice are under the influence of exchange forces due to the spins on the second sub-lattice as well as due to other spins on the same sub-lattice.

The molecular fields acting on the two sub-lattices A and B can be written as [3, 39, 41-42, 47-48]

$$\vec{H}_A = \lambda_{AA}\vec{M}_A + \lambda_{AB}\vec{M}_B,$$

$$\vec{H}_B = \lambda_{AB}\vec{M}_A + \lambda_{BB}\vec{M}_B$$

where $\vec{M}_A$ and $\vec{M}_B$ are the magnetizations of the two sub-lattices and λ"s are the Weiss constants. Since the interaction between the sub-lattices is anti-ferromagnetic, λ_{AB} must be negative, but λ_{AA} and λ_{BB} may be negative or positive depending on the crystal structure and the nature of the interacting atoms. Probably, these interactions are also negative, though they are in general quite small.

Assuming all the exchange interactions to be negative the molecular fields will be then given by

$$\vec{H}_A = -\lambda_{AA}\vec{M}_A - \lambda_{AB}\vec{M}_B,$$

$$\vec{H}_B = -\lambda_{AB}\vec{M}_A - \lambda_{BB}\vec{M}_B$$

Since in general, λ_{AA} and λ_{BB} are small compared to λ_{AB}, it is convenient to express the strengths of these interactions relative to the dominant λ_{AB} interaction.

$$\text{Let} \quad \lambda_{AA} = \alpha\lambda_{AB}$$

$$\text{And} \quad \lambda_{BB} = \beta\lambda_{AB}$$

In an external applied field $\vec{H}$, the fields acting on *A* and *B* sites are

$$\vec{H}_A = \vec{H} - \lambda_{AB}(\alpha\vec{M}_A - \vec{M}_B),$$

$$\vec{H}_B = \vec{H} - \lambda_{AB}(\vec{M}_A - \beta\vec{M}_B)$$

At temperatures higher than the transition temperature, T_N, $\vec{H}_A$, $\vec{M}_A$ and $\vec{M}_B$ are all parallel and we can write

$$\vec{M}_A = \frac{C_A}{T}[\vec{H} - \lambda_{AB}(\alpha\vec{M}_A - \vec{M}_B)], \qquad (2.3)$$

$$\vec{M}_B = \frac{C_B}{T}[\vec{H} - \lambda_{AB}(\vec{M}_A - \beta\vec{M}_B)] \tag{2.4}$$

Where C_A and C_B are the Curie constants for the two sublattices.

Here, $C_A = N_A g\mu_B^2 S_A(S_A+1)/3K$ and $C_B = N_B g\mu_B^2 S_B(S_B+1)/3K$

N_A and N_B denote the number of magnetic ions on A and B sites respectively and S_A and S_B are their spin quantum numbers. Solving for the susceptibility, χ, one gets [3,39]

$$\frac{1}{\chi} = \frac{T}{C} - \frac{1}{\chi_0} - \frac{b}{T-\theta}$$

$$\frac{1}{\chi} = \frac{T+(C/\chi_0)}{C} - \frac{b}{T-\theta} \tag{2.5}$$

Where C, χ_0, b and θ are constants for particular substance and are given by

$$C = C_A + C_B$$

$$\frac{1}{\chi_0} = -\frac{1}{C^2}[C_A^2\lambda_{AA} + C_B^2\lambda_{BB} + 2C_AC_B\lambda_{AB}]$$

$$b = \frac{C_AC_B}{C^3}[C_A^2(\lambda_{AA}-\lambda_{BB})^2 + C_B^2(\lambda_{BB}-\lambda_{AB})^2$$
$$-2C_AC_B\{\lambda_{AB}^2 - (\lambda_{AA}+\lambda_{BB})\lambda_{AB} + \lambda_{AA}\lambda_{BB}\}]$$

$$\theta = -\frac{C_AC_B}{C}(\lambda_{AB}+\lambda_{BB}) - 2\lambda_{AB}$$

Equation (2.5) represents a hyperbola, and the physically meaning part of it is plotted in Fig. 2.9. This curvature of the plot of $1/\chi$ versus T is a characteristics feature of a ferrimagnet. It cuts the temperature axis at T_C, called the Ferrimagnetic Curie point. At high temperatures the last term of equation (2.5) become negligible, and reduces to a Curie-Weiss law: $\chi = \dfrac{C}{T+(C/\chi_0)}$

This is the equation of straightline, shown dashed in Fig. 2.8, to which the $1/\chi$ versus T curve becomes asymptotic at high temperatures. The Ferrimagnetic Curie

temperature T_C is obtained from equations (2.3) and (2.4) with $H = 0$ and setting the determinant of the coefficients of M_i equal to zero. This gives

$$T_C = \frac{1}{2}[C_A\lambda_{AA} + C_B\lambda_{BB} + \{(C_A\lambda_{AA} - C_B\lambda_{BB})^2 + 4C_AC_B\lambda_{AB}^2\}^2] \qquad (2.6)$$

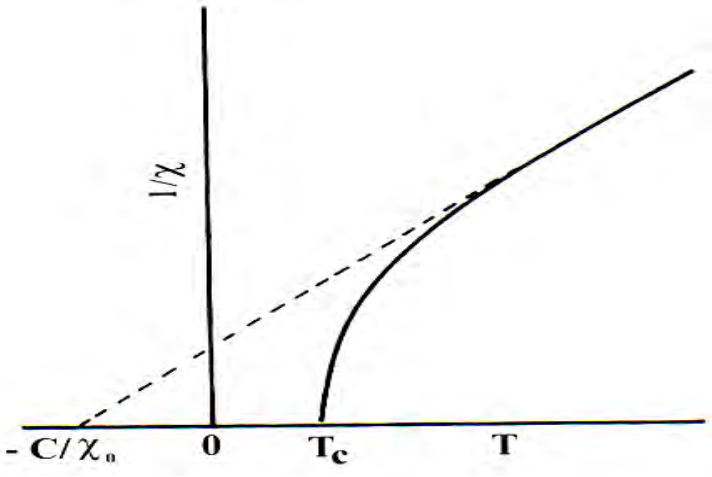

Fig.2.8. The temperature dependence of the inverse susceptibility for ferrimagnets.

Equation (2.5) is in good agreement with the experiment, except near the Curie point. The experimental Curie temperature, the temperature at which the susceptibility becomes infinite and spontaneous magnetization appears, is lower than the theoretical Curie temperature [39]. This disagreement between theory and experiment in the region of Curie point is presumably due to the short-range spin order (spin clusters) at temperatures above experimental T_C [3, 39].

The sub-lattice magnetizations will in general have different temperature dependences because the effective molecular fields acting on them are different. This suggests the possibility of having anomaly in the net magnetization versus temperature curves, Fig. 2.9. For most ferrimagnets the curve is similar to that of ferromagnets, but in a few cases there be a compensation point in the curve, Fig. 2.9(c) [2, 39]. At a point below the Curie temperature point, the two sub-lattice magnetizations are equal and thus appear to have no moment. This temperature is

called the compensation point. Below this temperature one sub-lattice magnetization is larger and provides the net moment. Above this temperature the other magnetization does dominates and the net magnetization reverses direction.

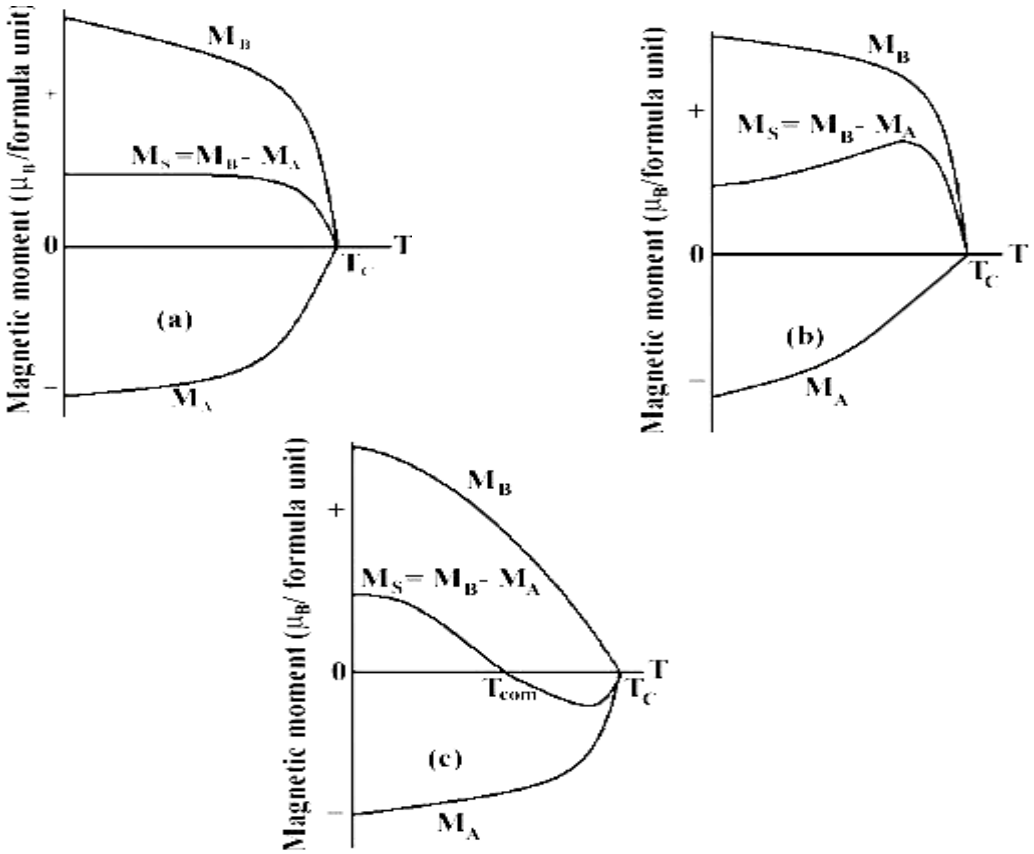

Fig.2.9 Superposition of various combinations of two opposing sublattice magnetizations producing differing resultants including one with a compensation point (schematic).

The essential requisite for Néel configuration is a strong negative exchange interaction between *A* and *B* sub-lattices which results in their being magnetized in opposite directions below the transition point. But there may be cases where intra-sublattice interactions are comparable with inter-sublattice interaction. Neel's theory predicts paramagnetism for such substances at all temperatures. This is unreasonable since strong *AA* or *BB* interaction may lead to some kind of ordering especially at low temperature. In the cases of no *AB* interaction, antiferromagnetic ordering may be

expected either in the or in the *B* sub-lattice. Under certain conditions there may be non-collinear spin arrays of still lower energy.

2.7 Microstructure

A polycrystalline is much more than many tiny crystals bonded together. The interfaces between the crystals, or the grain boundaries which separate and bond the grains, are complex and interactive interfaces. The whole set of a given material‟s properties (mechanical, chemical and especially electrical and magnetic) depend strongly on the nature of the microstructure.

In the simplest case, the grain boundary is the region, which accommodates the difference in crystallographic orientation between the neighboring grains. For certain simple arrangements, the grain boundary is made of an array of dislocations whose number and spacing depends on the angular deviation between the grains. The ionic nature of ferrites leads to dislocation patterns considerably more complex than in metals, since electrostatic energy accounts for a significant fraction of the total boundary energy [3]. For low-loss ferrite, Ghate [2] states that the grain boundaries influence properties by

1) creating a high resistivity intergranular layer,
2) acting as a sink for impurities which may act as a sintering aid and grain growth modifiers,
3) Providing a path for oxygen diffusion, this may modify the oxidation state of cations near the boundaries.

In addition to grain boundaries, ceramic imperfections can impede domain wall motion and thus reduce the magnetic property. Among these are pores, cracks, inclusions, second phases, as well as residual strains. Imperfections also act as energy wells that pin the domain walls and require higher activation energy to detach.

Stresses are microstructural imperfections that can result from impurities or processing problems such as too rapid a cool. They affect the domain dynamics and are responsible for a much greater share of the degradation of properties than would expect [2].

Grain growth kinetics depends strongly on the impurity content. A minor dopant can drastically change the nature and concentration of defects in the matrix, affecting grain boundary motion, pore mobility and pore removal [3, 52]. The effect of a given dopant depends on its valence and solubility with respect to host material. If it is not soluble at the sintering temperature, the dopant becomes a second phase which usually segregates to the grain boundary.

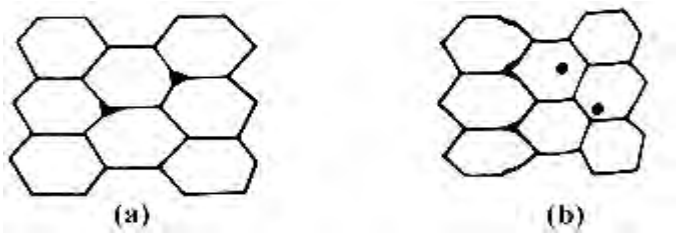

Fig.2.10 Porosity character: (a) intergranular, (b) intragranular.

The porosity of ceramic samples results from two sources, intragranular porosity and intergranular porosity, Fig. 2.10. An undesirable effect in ceramic samples is the formation of exaggerated or discontinuous grain growth which is characterized by the excessive growth of some grains at the expense of small, neighboring ones (Fig. 2.11).

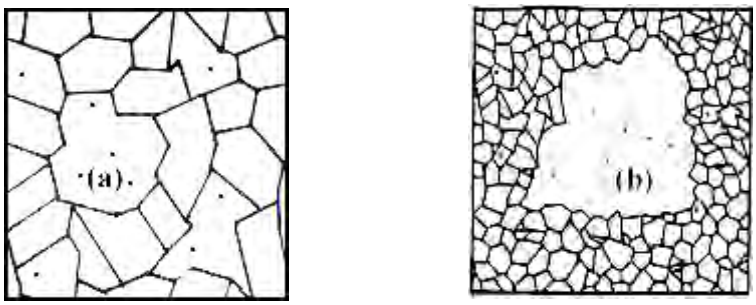

Fig.2.11 Grain growth (a) discontinuous (b) duplex (schematic).

When this occurs, the large grain has a high defect concentration. Discontinuous growth is believed to result from one or several of the following: powder mixtures with impurities; a very large distribution of initial particle size; sintering at excessively high temperatures; in ferrites containing *Zn* and /or *Mn*, a low O_2 partial pressure in the sintering atmosphere. When a very large grain is surrounded by smaller ones, it is called „duplex" microstructure.

2.8 Theories of Permeability:

Permeability is defined as the proportionality constant between the magnetic field induction *B* and applied field intensity *H* [3, 47,50].

$$B = \mu H \tag{2.7}$$

If the applied field is very low, approaching zero, the ratio will be called the initial permeability, Fig. 2.15 and is given by

$$\mu_i = \frac{\Delta B}{\Delta H}_{(\Delta H \to 0)}$$

This simple definition needs further sophistications. A magnetic material subjected to an ac magnetic field can be written as

$$H = H_0 e^{i\omega t} \tag{2.8}$$

It is observed that the magnetic flux density *B* lag behind *H*. This is caused due to the presence of various losses and is thus expressed as

$$B = B_0 e^{i(\omega t-\delta)} \tag{2.9}$$

Here δ is the phase angle that marks the delay of *B* with respect to *H*. The permeability is then given by

$$\mu = \frac{B}{H} = \frac{B_0 e^{i(\omega t-\delta)}}{H_0 e^{i\omega t}} = \frac{B_0 e^{-i\delta}}{H_0} = \frac{B_0}{H_0}\cos\delta - i\frac{B_0}{H_0}\sin\delta = \mu^{/} - i\mu^{//} \tag{2.10}$$

$$\text{where} \quad \mu' = \frac{B_0}{H_0}\cos\delta \tag{2.11}$$

$$\text{and} \quad \mu'' = \frac{B_0}{H_0}\sin\delta \tag{2.12}$$

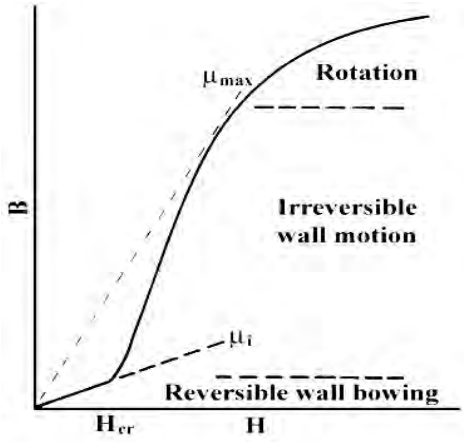

Fig.2.12 Schematic magnetization curve showing the important parameter: initial permeability, μ_i (the slope of the curve at low fields) and the main magnetization mechanism in each magnetization range [3].

The real part (μ') of complex permeability (μ), as expressed in equation (2.10) represents the component of *B* which is in phase with *H*, so it corresponds to the normal permeability. If there are no losses, we should have $\mu = \mu'$. The imaginary part μ'' corresponds to that of *B*, which is delayed by phase angle 90° from *H* [48, 49]. The presence of such a component requires a supply of energy to maintain the alternating magnetization, regardless of the origin of delay. The ratio of μ'' to μ', as is evident from equation (2.12) and (2.11) gives

$$\frac{\mu''}{\mu'} = \frac{\frac{B_0}{H_0}\sin\delta}{\frac{B_0}{H_0}\cos\delta} = \tan\delta \tag{2.13}$$

This $\tan\delta$ is called loss factor.

The quality factor is defined as the reciprocal of this loss factor, i.e.

$$\text{Quality factor} = \frac{1}{\tan\delta} \tag{2.14}$$

$$\text{And the relative quality factor, } Q = \frac{\mu'}{\tan\delta} \tag{2.15}$$

The curves that show the variation of both μ' and μ'' with frequency are called the magnetic spectrum or permeability spectrum of the material [39]. The variation of permeability with frequency is referred to as dispersion. The measurement of complex permeability gives us valuable information about the nature of domain wall and their movements. In dynamic measurements the eddy current loss is very important. This occurs due to the irreversible domain wall movements. The permeability of a ferrimagnetic substance is the combined effect of the wall permeability and rotational permeability mechanisms.

2.8.1 Mechanisms of Permeability

The mechanisms can be explained as follows: A demagnetized magnetic material is divided into number of Weiss domains separated by Bloch walls. In each domain all the magnetic moments are oriented in parallel and the magnetization has its saturation value M_s. In the walls the magnetization direction changes gradually from the direction of magnetization in one domain to that in the next. The equilibrium positions of the walls result from the interactions with the magnetization in neighboring domains and from the influence of pores; crystal boundaries and chemical in homogeneities which tend to favour certain wall positions.

2.8.1.1 Wall Permeability

The mechanism of wall permeability arises from the displacement of the domain walls in small fields. Let"s us consider a piece of material in the demagnetized state, divided into Weiss domains with equal thickness L by means of 180° Bloch

walls (as in the Fig. 2.13). The walls are parallel to the YZ plane. The magnetization M_s in the domains is oriented alternately in the $+Z$ or $-Z$ direction. When a field H with a component in the $+Z$ direction is applied, the magnetization in this direction will be favoured. A displacement dx of the walls in the direction shown

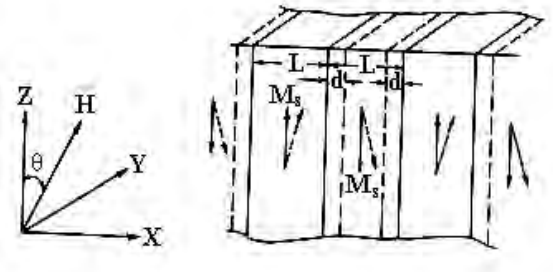

Fig.2.13 Magnetization by wall motion and spin rotation.

By the dotted lines will decrease the energy density by an amount [35, 21]:

$$\frac{2M_s H_z dx}{L}$$

This can be described as a pressure $M_s H_z$ exerted on each wall. The pressure will be counteracted by restoring forces which for small deviations may assume to be kdx per unit wall surface. The new equilibrium position is then given by

$$d = \frac{M_s H_z dx}{L}$$

From the change in the magnetization

$$\Delta M = \frac{2M_s d}{L},$$

the wall susceptibility χ_w may be calculated. Let H makes the angle θ with Z direction. The magnetization in the θ direction becomes

$$(\Delta M)_\theta = \frac{2M_s d}{L}\cos\theta \text{, And with } H_z = H\cos\theta \text{ and } d = \frac{2M_s H_z}{K}$$

we obtain

$$\chi_w = \frac{(\Delta M)_\theta}{H} = \frac{4M_s^2 \cos^2 \theta}{KL} \tag{2.16}$$

2.8.1.2 Rotational Permeability

The rotational permeability mechanism arises from rotation of the magnetization in each domain. The direction of M can be found by minimizing the magnetic energy E as a function of the orientation. Major contribution to E comes from the crystal anisotropy energy. Other contributions may be due to the stress and shape anisotropy. The stress may influence the magnetic energy via the magnetostriction. The shape anisotropy is caused by the boundaries of the sample as well as by pores, nonmagnetic inclusions and in homogeneities. For small angular deviations, α_x and α_y may be written as

$$\alpha_x = \frac{M_x}{M_s} \text{ and } \alpha_y = \frac{M_y}{M_s}.$$

For equilibrium Z-direction, E may be expressed as [52]

$$E = E_0 + \frac{1}{2}\alpha_x^2 E_{xx} + \frac{1}{2}\alpha_y^2 E_{yy}$$

where it is assumed that x and y are the principal axes of the energy minimum. Instead of E_{xx} & E_{yy}, the anisotropy field H_x^A and H_y^A are often introduced. Their magnitude is given by $H_x^A = \frac{E_{xx}}{2M_s}$ and $H_y^A = \frac{E_{yy}}{2M_s}$,

H_x^A & H_y^A represent the stiffness with which the magnetization is bound to the equilibrium direction for deviations in x and y direction, respectively. The rotational susceptibilities $\chi_{r,x}$ and $\chi_{r,y}$ for fields applied along x and y directions, respectively are $\chi_{r,x} = \frac{M_s}{H_x^A}$ and $\chi_{r,y} = \frac{M_s}{H_y^A}$.

For cubic materials it is often found that H_x^A and H_y^A are equal. For $H_x^A = H_y^A = H^A$ and a field H which makes an angle θ with the Z direction (as shown in Fig. 2.13) the rotational susceptibility, $\chi_{r,c}$ in one crystallite becomes

$$\chi_{r,c} = \frac{M_s}{H^A} \sin^2 \theta \qquad (2.17)$$

A polycrystalline material consisting of a large number of randomly oriented grains of different shapes, with each grain divided into domains in a certain way. The rotational susceptibility χ_r of the material has to be obtained as a weighted average of $\chi_{r,c}$ of each crystallite, where the mutual influence of neighboring crystallites has to be taken into account. If the crystal anisotropy dominates other anisotropies, then H^A will be constant throughout the material, so only the factor $\sin^2 \theta$ (equation 2.17) has to be averaged. Snoek [52] assuming a linear averaging of $\chi_{r,c}$ and found

$$\chi_r = \frac{2M_s}{3H^A}$$

The total internal susceptibility

$$\chi = \chi_w + \chi_r = \frac{4M_s^2 \cos^2 \theta}{KL} + \frac{2M_s}{3H^A} \qquad (2.18)$$

If the shape and stress anisotropies cannot be neglected, H^A will be larger. Any estimate of χ_r will then be rather uncertain as long as the domain structure, and the pore distribution in the material are not known. A similar estimate of χ_w would require knowledge of the stiffness parameter k and the domain width L. These parameters are influenced by such factors as imperfection, porosity and crystallite shape and distribution which are essentially unknown.

2.8.1.3 Frequency dependent Permeability Curve

The techniques of impedance spectroscopy, widely used in dielectrics have been applied to magnetic materials [40]. In this method, impedance measurements as a function of frequency are modified by means of an equivalent circuit and its elements are associated with the physical parameters of the material.

The complex permeability, μ^*, is determined from the complex impedance, Z^*, by :

$$\mu^* = (jk/\omega)Z^* \qquad (2.19)$$

Where k is the geometric constant relating to inductance, l, to the permeability. The equivalent circuit for domain wall bowing (applied field lower than critical field) is a parallel RL arrangement; for wall displacement, additional Warbarg-type impedance element is required (Irvine *et al*.) [53].

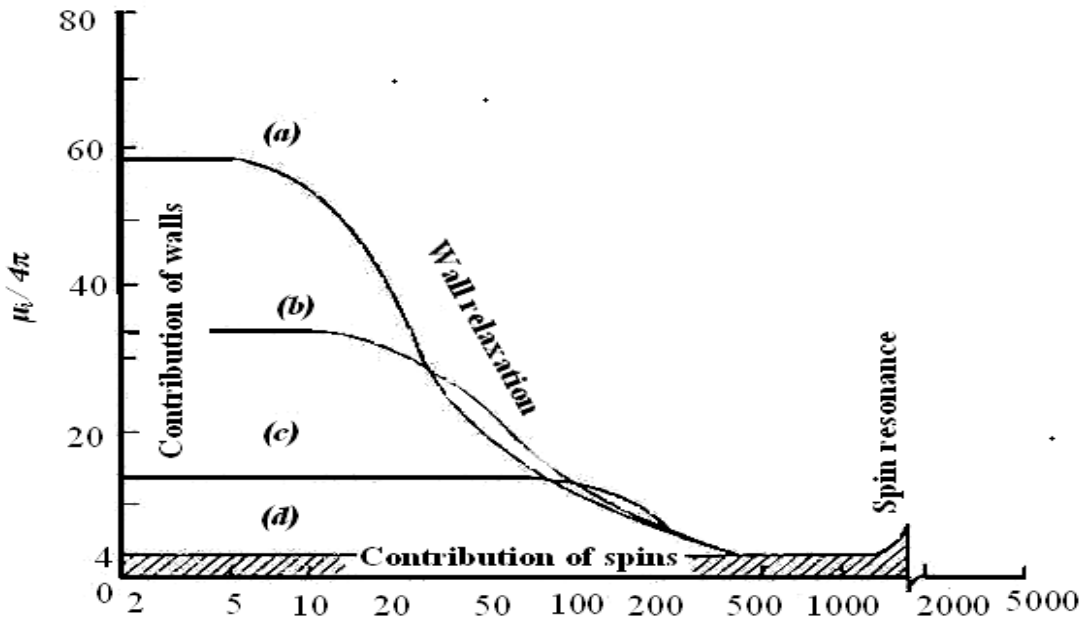

Fig.2.14 Permeability spectra of $NiFe_2O_4$ samples with different grain size: (a)11μm;(b) 5μm;(c)2 μm (d)size <0.2 μm(single domain behavior) [3].

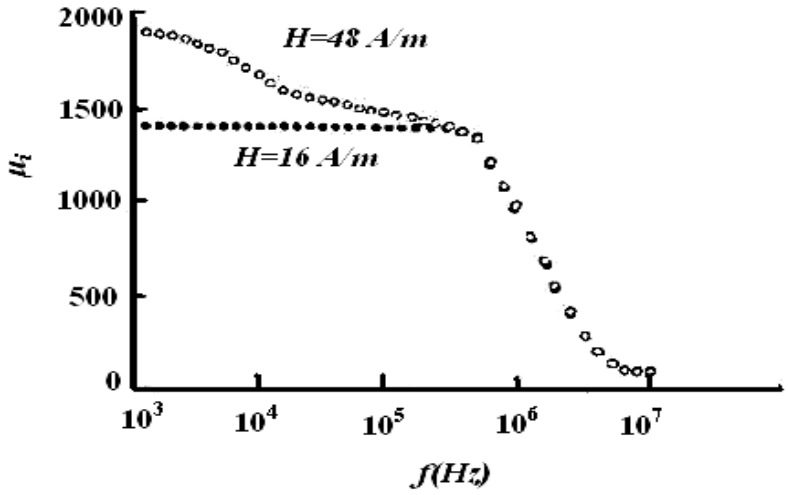

Fig.2.15 Permeability spectrum of a *Ni-Zn* sample at fields above (open circles) and below (filled circles) the critical field [54].

Many of the specific applications of ferrites depend on their behavior at high frequencies. When subjected to an ac field, ferrite permeability shows several dispersions; as the field frequency increases, the various magnetization mechanisms become unable to follow the field. The dispersion frequency for each mechanism is different time constants, Fig. 2.14. The low frequency dispersions are associated with domain wall dynamics and the high frequency dispersion, with spin resonance. The spin resonance phenomena occur usually in the GHz range. The two main magnetization mechanisms are wall bowing and wall displacement as discussed before in section 2.8. Any field results in a bowing of pinned walls, and if this field has higher value than the corresponding critical field, walls are unpinned and displaced. Otherwise, bowed walls remain pinned to material defects. Measurements at low fields therefore show only one wall dispersion. Measurements at high fields, several, complex dispersions are observed, such as those in Fig. 2.15. Wall displacement dispersion occurs at lower frequencies than wall bowing, since hysteresis is a more complex phenomenon of wall bowing, unpinning, displacement and pinning steps.

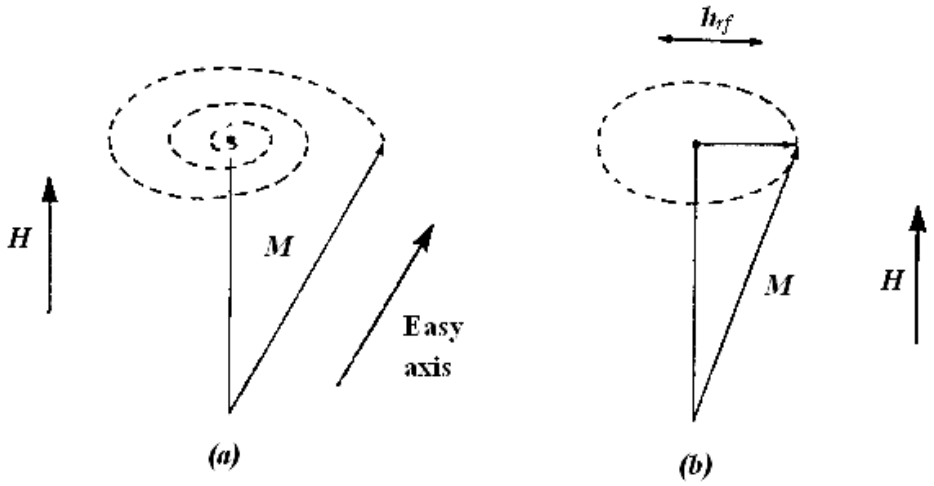

Fig.2.16 (a) Schematic representation of the spin deviation from an easy axis by processional spiraling into the field direction, (b) Precession is maintained by a perpendicular rf field, h_{rf} [3].

At very high frequencies, domain walls are unable to follow the field and the only remaining magnetization mechanism is spin rotation within domains. This mechanism eventually also shows a dispersion, which always takes the form of a resonance. Spins are subjected to the anisotropy field, representing spin-lattice coupling; as an external field is applied (out of the spins" easy direction), spins experience a torque. However, the response of spins is not instantaneous; spins precess around the field direction for a certain time (the relaxation time, *τ)* before adopting the new orientation, Fig. 2.16.

The frequency of this precession is given by the Larmor frequency:

$$\omega_L = \gamma \mu_o H_T \qquad (2.20)$$

Where H_T is the total field acting on the spin.

$H_T = H_K + H + H_d + \ldots\ldots$, where H_K ,H, H_d are the anisotropy and the external and demagnetization fields, respectively. If an ac field of angular frequency ω_L is applied to the sample, a resonant absorption (ferromagnetic resonance) occurs. The Larmour frequency is independent of the precession amplitude.

2.9 Magnetization Mechanism

2.9.1 Concept of Magnetic Domain and Domain Wall

In 1907 Pierre Weiss in his paper "Hypothesis of the molecular field" [46, 55] postulated that a ferromagnetic material rather than be uniformly magnetized, is divided into a number of regions of domains, each of which is magnetized to saturation level but the direction of magnetization from domain to domain need not be parallel. The magnetization vectors are parallel to preferred direction such that the demagnetization field, and hence the demagnetization energy ($W_{dem.} = 1/8\pi H^2_D$) is as small as possible. The total magnetization is then given by the vector summation of individual magnetization over all domains. The demagnetized state of the magnet is from the view point of an observer outside the material. In ferromagnetic materials, the atomic magnetic moments aligned in parallel fashion, while in ferrite domain, the net moments of the anti-ferromagnetic interaction are spontaneously oriented parallel to each other (even without applied magnetic field) [56]. The applied field serves as a control in changing the balance of potential energy within the, magnetic material. These uniformly magnetized domains are separated by a thin layer in which the magnetization gradually changes from one orientation to another. This transition boundary is called domain wall or Bloch wall.

The domain structure are found basically to reduce the magnetostatic energy i.e., the magnetic potential energy contained in the field lines (or flux lines) connecting north and south poles outside of the material. This concept can be understood by considering a simple case, as shown in Fig. 2.17, in which (a) to (e) represents a cross section of a ferromagnetic single crystal. In Fig. 2.17 (a) a single domain crystal is shown, the value of magnetostatic energy is high. The arrow indicates the direction of magnetization and hence the direction of spin alignment in the domain. If the crystal

is divided into two domains (Fig. 2.17 (b), the magnetic energy will be reduced by roughly one half of the single domain case. This splitting process continues to lower the energy of the system until more energy is required to form the domain boundary. When a large domain is split into *n* domains, as shown in Fig. 2.17 (c) the magnetic energy will be reduced to approximately *1/n* of the magnetic energy of that of type (a). For the domain structure configuration in Fig. 2.17 (d) and (e), the magnetic energy is zero as the flux circuit is completed within a crystal, (i.e., flux path never leaves the boundary of the material). These triangular domains are callled closure domains. Therefore the magnetostatic energy is reduced. This type of structure may also be found at the surface of the material. The boundaries between the domains are not sharp on atomic scale but are spread over a finite thickness within which the direction of the spin changes gradually from one domain to the next [55]. The spin within a domain wall as shown in Fig. 2.18, are pointing in necessary directions, so that the crystal anisotropy energy within the wall is higher than it is in the adjacent domains.

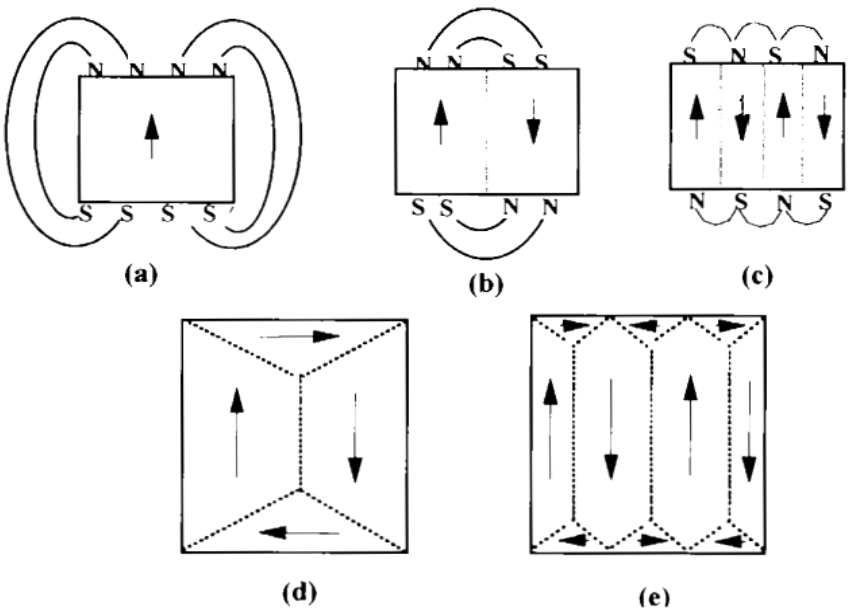

Fig.2.17 Possible domain structures showing progressively low energy .Each part is representing a cross-section of a ferromagnetic single crystal [3, 40].

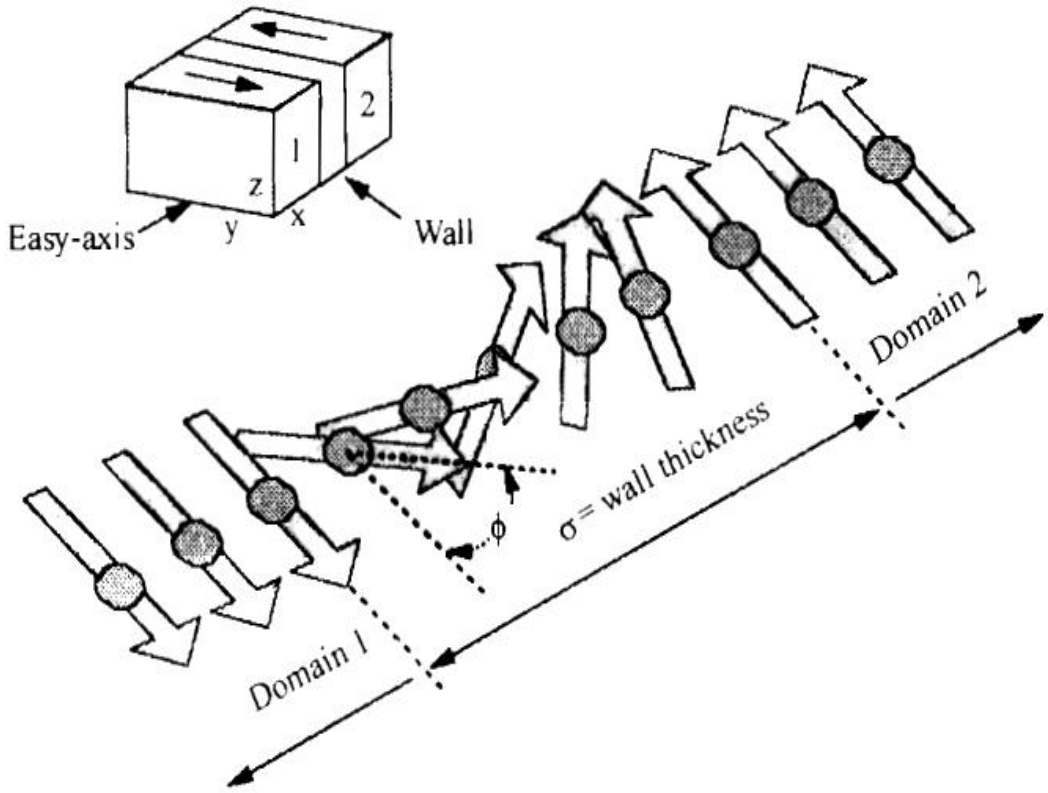

Fig.2.18 Schematic representation of a domain wall. All spins, within the wall thickness are in non-easy direction [39].

The exchange energy tries to align the spin in a direction parallel to the direction in the domain while the anisotropy energy tries to make the wall thin to minimize misalignment within the easy directions. The actual thickness of the domain wall is determined by the counterbalance of the exchange energy and anisotropy energy.

2.9.2 The dynamic behavior of Domains

Two general mechanisms are involved in changing the magnetization in a domain and, therefore, changing the magnetization in a sample. The first mechanism acts by rotating the magnetization towards the direction of the field. Since this may involve rotating the magnetization from an axis of easy magnetization in a crystal to one of more difficult magnetization, a certain amount of anisotropy energy is required. The

rotations can be small as indicated in Figure 2.19 (a) or they can be almost the equivalent of a complete 180˚ reversal or flip if the crystal structure is uniaxial and if the magnetizing field is opposite to the original magnetization direction of the domain. The other mechanism for changing the domain magnetization is one in which the direction of magnetization remains the same, but the volumes occupied by the different domains may change. In this process, the domains whose magnetizations are in a direction closest to the field direction grow larger while those that are more unfavorably oriented shrink in size. Fig. 2.19 (b) shows this process which is called domain wall motion.

The mechanism for domain wall motion starts in the domain wall. Present in the wall is a force (greatest with the moments in the walls that are at an angle of 90˚ to the applied field) that will tend to rotate those moments in line with the field. As a result, the center of the domain wall will move towards the domain opposed to the field. Thus, the area of the domain with favorable orientation will grow at the expense of its neighbour.

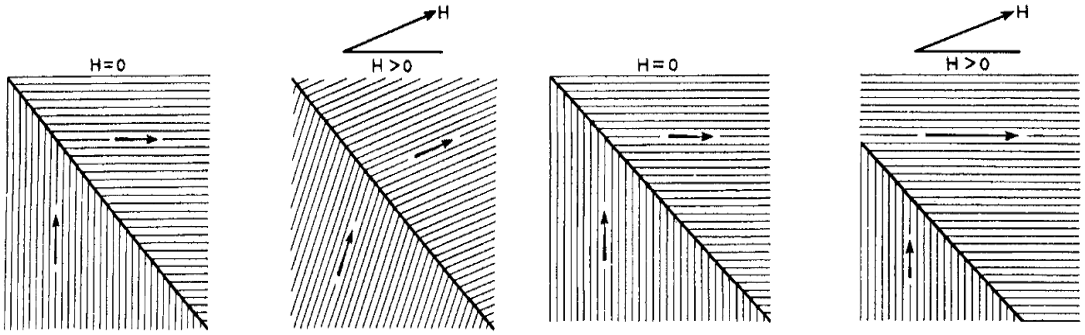

(a)Volume constant , directions changed b)Volume changed , directions constant

Fig.2.19 (a) Change of domain magnetization by domain wall movement and (b) Change of domain magnetization by domain rotation [40].

2.9.3 Bulk Material Magnetization

Although domains are not physical entities such as atoms or crystal lattices and can only be visualized by special means, for the purpose of magnetic structure

they are important in explaining the process of magnetization. A material that has strongly oriented moments in a domain often has no resultant bulk material magnetization. Non-magnetic material can be transformed into a strongly magnetic body by domain dynamics discussed above. If the material has been demagnetized, the domains point in all random directions so that there is complete cancellation and the resultant magnetization is zero (Fig. 2.20). The possible steps to complete orientation of the domains or magnetization of the material are also shown in Fig. 2.20 [40].

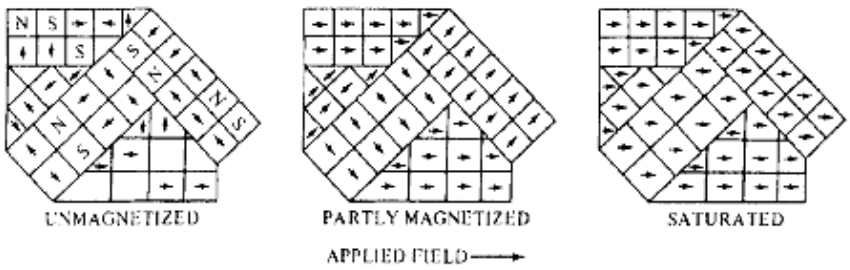

Fig.2.20 Stages in Magnetization of a sample containing several crystals [40].

2.9.4 The Magnetization Curve

For unmagnetized bulk material, there is a zero net magnetic moment. It can be predicted that there will be an infinite number of degree of magnetization between the unmagnetized and saturation condition, when the material is subjected to an external magnetic field. These extreme situations correspond respectively, to random orientation of domains complete alignment in one direction with elimination of domain walls. It can be started with the demagnetized specimen and increase the applied magnetic field and then the bulk material will be progressively magnetized by the domain dynamics. The magnetization of the sample will follow the course as shown in Fig. 2.21 [40]. The slope from the origin to a point on the curve or the ratio *M/H* is defined as magnetic susceptibility. This curve is called Magnetization Curve. This curve is generally perceived as being made of three major portions.

The first, the lower section, is the initial susceptibility region and is characterized by reversible domain wall movements and rotations. By reversible means that after the magnetization slightly with an increase in field the original magnetization conditions can be reversed if the field is reduced to initial value. The contribution of the displacement walls to an initial permeability is entirely dependent on the sort of material studied.

In the second stage magnetization curve, if the field is increased, the intensity of the magnetization increases more drastically, is called the irreversible magnetization range. This range is obtained mainly by the irreversible domain wall motion from one stable state to another. If the field is increased further, the magnetization curve become less steep and its process become reversible once more. In the third section of magnetization curve, the displacement of domain walls has already been completed and the magnetization takes place by rotation magnetization.

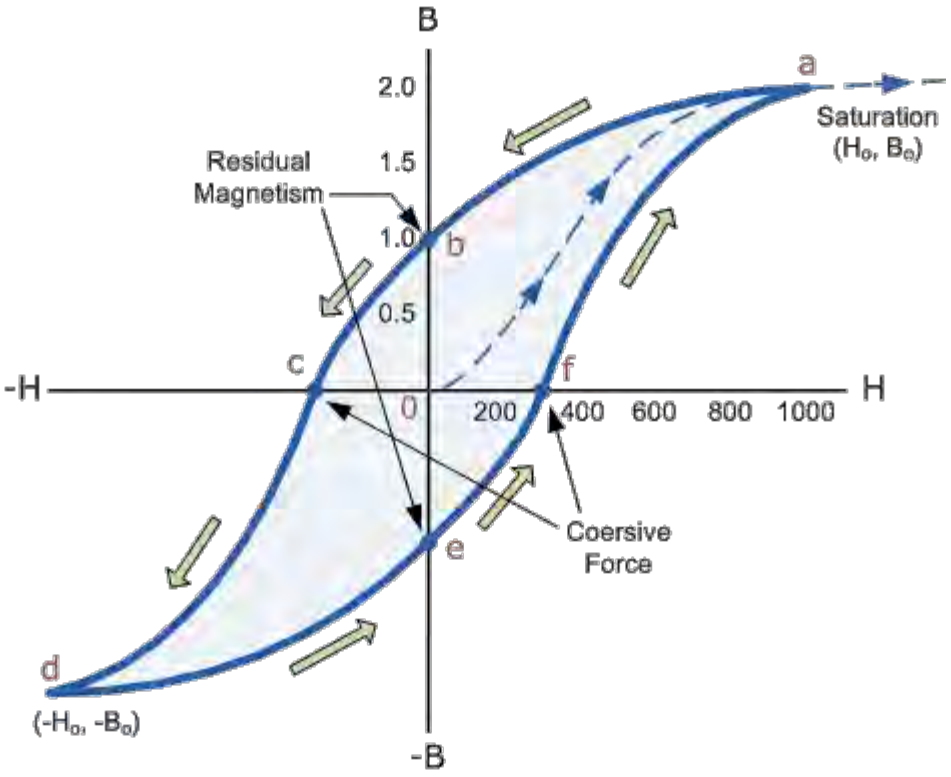

Fig.2.21 Domain dynamics during various parts of the magnetization curve [40].

This range is called rotation magnetization range. Beyond this range the magnetization gradually approaches to saturation magnetization (Fig. 2.21 b).

References

[1] Nicola, A., Spaldin, "Magnetic Materials, Fundamentals and device applications", Cambridge University Press, 2003.

[2] Goldman, A., "Handbook of Modern Ferromagnetic Materials", Kluwer Academic Pub., Boston U.S.A, 1999.

[3] Valenzuela, R., "Magnetic Ceramics", Cambridge University Press, Cambridge, 1994.

[4] Haque, M. M., "Influence of additives on the magnetic and electrical properties of iron-excess Mn-Zn ferrites," M. Phil. Thesis, BUET, Bangladesh, 2000.

[5] Wafaa, B., "Structural and electrical properties of zinc-substituted cobalt ferrite", J. Mater. Sci. Vol. 42, pp. 8254–8261, 2007.

[6] Goldman, A., "Modern Ferrites Technology", 2nd Edition, Pittsburgh, PA, USA, 1999.

[7] Hossain, A. K. M. Akther., Seki, M., Kawai, T., and Tabata, H., "Colossal magnetoresistance in spinel type $Zn_{1-x}Ni_xFe_2O_4$", J. Appl. Phys., Vol. 96, pp.1273-1275, 2004.

[8] Harzali, H., Saida, F., Marzouki, A., Megriche, A., Baillon, F., Espitalier, F., Mgaidi, A., "Structural and magnetic properties of nano-sized NiCuZn ferrites synthesized by co-precipitation method with ultrasound irradiation" J. Magn. Magn. Mater, Vol. 419, pp. 50-56, 2016.

[9] Zehani, K., Mazaleyrat, F., Loyau, V., Laboure, E., "Effect of temperature and time on properties of spark plasma sintered *Ni-Cu-Zn*: *Co* ferrite." J. Appl. Phys. Vol. 109, pp. 07A504 (1-3), 2011

[10] Hossain, A. K. M. Akther, Biswas, T. S., Mahmud, S. T., Yanagida, T., Tanaka, H., Kawai, T., "Enhancement of initial permeability due to Mn substitution in polycrystalline $Ni_{0.50-x}Mn_xZn_{0.50}Fe_2O_4$", J. Magn. Magn. Mater., Vol. 321, pp. 81-87, 2009.

[11] Zehani, K., Mazaleyrat, F., Loyau, V., Laboure, E., "Effect of temperature and time on properties of spark plasma sintered *Ni-Cu-Zn*: *Co* ferrite", J. Appl. Phys. Vol. 109(7), pp. 07A504, 2011.

[12] Ding, J., McCormick, P. Cl., and Street, R., "Magnetic properties of mechanically alloyed $CoFe_2O_4$", Solid State Commun., Vol. 95(1), pp. 31-33, 1995.

[13] Chengyi Hou, Hao Yu, Qinghong Zhang, Yaogang Li, Hongzhi Wang, "Preparation and magnetic property analysis of monodisperse Co–Zn ferrite nanospheres", J. Alloys Compd., Vol. 491, pp. 431–435, 2010.

[14] Arulmurugan, R., Jeyadevan, B., Vaidyanathan, G., Sendhilnathan, S., "Effect of zinc substitution on Co–Zn and Mn–Zn ferrite nanoparticles prepared by coprecipitation", J. Magn. Magn. Mater., Vol. 288, pp. 470–477, 2005.

[15] Hossain, A. K. M. Akther, Tabata, H., Kawai, T. "Magnetoresistive properties of $Zn_{1-x}Co_xFe_2O_4$ ferrites", J. Magn. Magn. Mater., Vol 320 (6), pp. 1157-1162, 2008.

[16] Xu, X., Cao, C., **"**Structure and ferromagnetic properties of Co-doped ZnO powders", J. Magn. Magn. Mater., Vol. 321 (14), pp. 2216-2219, 2009.

[17] Hossain, A. K. M. Akther, Khirul Kabir, K., Seki, M., Kawai, T., and Tabata, H., "Structural, AC, and DC magnetic properties of Co-Zn ferrite", J. Phys. Chem. Solids, Vol. 68 (10), pp. 1933-1939, 2007.

[18] Khan, M. H. R. Hossain, A. K. M. Akther, "Reentrant spin glass behavior and large initial permeability of $Co_{0.5-x}Mn_xZn_{0.5}Fe_2O_4$", J. Magn. Magn. Mater., Vol. 324, pp. 550-558, 2012.

[19] Azizi, A., Yoozbashizadeh, H., Yourdkhani, A., Mohammadi, M., "Phase formation and change of magnetic properties in mechanical alloyed $Ni_{0.5}Co_{0.5}Fe_2O_4$ by annealing", J. Magn. Magn. Mater., Vol. 322(1), pp. 56–59, 2010.

[20] Waje, S. B., Hashim, M., Yusoff, W. D. W., & Abbas, Z., "Sintering temperature dependence of room temperature magnetic and dielectric properties of $Co_{0.5}Zn_{0.5}Fe_2O_4$ prepared using mechanically alloyed nano particles", J. Mang. Mang. Mater., Vol 322, pp. 686-691, 2010.

[21] Rezlescu, N., Rezlescu, E., Pasnicu, C. and Craus, M. L., "Effects of the rare-earth ions on some properties of a Nickel-Zinc ferrite," J. Phys: Condens. Matter., Vol.6, pp. 5707-5716, 1994.

[22] Solyman, S., "Transport properties of La-doped Mn–Zn ferrite," Cera. Intern. Vol. 32(7), pp. 755-760, 2006.

[23] Sattar A. A, "Physical, magnetic and electrical properties of Ga substituted Mn ferrites", Egptian J Sol, Vol-27, pp. 99-110, 2004.

[24] Ahmed, M. A., and EL-Sayed, M. M., "Magnetic characterization and thermoelectric power of $Ni_{1-y}Zn_yCu_{0.3}Fe_{1.7}O_4$", J. Magn. Magn. Mater, Vol-308, pp. 40–45, 2007.

[25] Bogoroditzkll, N., Pasynkov, V. V., Basili, R. R., and Volokobinskll, Y. M., "Electrical Properties of the Rare-Earth Oxides", In Sov. Phys. Doklady Vol. 10, pp. 85, 1965.

[26] Sun, G. L., Li, J. B., Sun, J. J., Yang, X. Z., "The influences of Zn^{2+} and some rare-earth ions on the magnetic properties of nickel–zinc ferrites," J. Magn. Magn. Mater. Vol. 281(2), pp. 173-177, 2004.

[27] Rezlescu, N., Rezlescu, E., "The influence of Fe substitutions by R ions in a Ni-Zn Ferrite," Solid State Communications", Vol. 88, pp. 139-141, 1993.

[28] Gul, I. H. and Erum Pervaiz, "comparative study of $NiFe_{2-x}Al_xO_4$ ferrite nanoparticles synthesized by chemical co-precipitation and sol-gel combustion techniques," Mater. Res. Bull., Vol. 47, pp. 1353-1361, 2012.

[29] Jacobo, S. E., Duhalde, S., Bertorello , H. R., "Rare earth influence on the structural and magnetic properties of Ni-Zn ferrites," J. Magn. Magn. Mater. Vol. 2253, pp. 272–276, 2004.

[30] Zhao, L., Cui, Y., Yang, H., Yu, L., Jin, W., Feng, S., "The magnetic properties of $Ni_{0.7}Mn_{0.3}Gd_xFe_{2-x}O_4$ ferrite", Mat. Lett. Vol. 60(1), 104-108, 2006.

[31] Sun, J. J., Li, J. B., Sun, G. L. and Qu, W. G., "Synthesis of Dense Ni-Zn Ferrites by Spark Plasma sintering," Ceramics International, Vol. 28(8), pp. 855-858, 2002.

[32] Tasaki, J. and Ito, T., "Effect of Sintering Atmosphere on the permeability of Sintered Ferrites.", Ferrites: proceedings of the International. Conference on Ferrites, Japan, pp. 84-86, 1970.

[33] Nakamura, T., "Low-temperature sintering of Ni-Zn-Cu ferrite and its permeability spectra," J. Magn. Magn. Mater, Vol. 168, pp. 285-291, 1997.

[34] Roess, E., "Ferrites", University of Tokyo Press, Tokyo, pp.187, 1971.

[35] Leung, L. K., Evans, B. J. and Morrish, A. H., "Low-temperature Mössbauer study of a nickel-zinc ferrite: $Zn_{1-x}Ni_xFe_2O_4$," Physics Review B, Vol. 8, pp. 29-43, 1973.

[36] E. Rezlescu, L. Sachelarie, P. D. Popa and N. Rezlescu, "Effect of substitution of diavalent ions on the electrical and magnetic properties of Ni-Zn-Me ferrites," IEEE Trans. Magn, Vol. 36, pp. 3962-3967, 2000.

[37] Globus, A., "2nd EFS Conf. on Soft Magnetic Material", Wolfson Center for Magnetic Technology, Cardiff, Wales, 1975.

[38] El-Shabasy, M., "DC electrical properties of Ni-Zn ferrites," J. Magn. Magn. Mater, Vol.172, pp. 188-192, 1997.

[39] Cullity, B. D., "Introduction to Magnetic Materials", Addison-Wiley Publishing Company, Inc., California, 1972.

[40] Goldman, Alex, "Modern Ferrite Technology", 2nd Ed, Springer Science-Business Media, Inc, Pittsburgh, PA, USA, 2006.

[41] Brailsford, F., "Physical Principles of Magnetism", D. Van Nostrand Company Ltd., London, 1966.

[42] Dekker, A. J., "Solid State Physics", Macmillan India Ltd., New Delhi, 1998.

[43] Argentina, G. M., and Baba, P. D., "Microwave Lithium Ferrites: An Overview", IEEE Trans. Microw. Theory Techn, Vol. MTT-22, No. 6, pp. 652-658, 1974.

[44] Jadhav, S. A., "Magnetic properties of Zn-substituted Li-Cu ferrites", J. Magn. Magn. Mater, vol. 224, pp. 167-172, 2001.

[45] Baba, P. D. and Banerjee, S. K., "Microwave ferrite program," Summary Technical Report, ESD-TR-68-251, 1968.

[46] Smit, J. and Wijn, H. P. J. , "Ferrites", John Wiley and Sons, New York, p. 216,1959.

[47] Chikazumi, S., "Physics of Magnetism", John Wiley & Sons, Inc., New York, 1966.

[48] Wahab, M. A., "Solid State Physics-Structure and properties of materials", Narosa publishing house, New Delhi, 1999

[49] Kittel, C., "Introduction to Solid State Physics", 7th edition, John Wiley & Sons, Inc., Singapore, 1996.

[50] Hadfield, D., "Permanent Magnets and Magnetism", John Wiley & Sons, Inc., New York, 1962.

[51] Sikder, S. S., "Temperature dependence of magnetization and induced magnetic anisotropy of some Fe, Co and Ni-based amorphous ribbons," Ph. D. Thesis, BUET, Bangladesh, 1999.

[52] Snoek, J. L., Physica , "Dispersion and absorption in magnetic ferrites at frequencies above one Mc/s", Vol. 14, pp. 207-217, 1948.

[53] Irvine, J. T. S., West, A. R., Amano , E., Huanosta, A. & Valenzuela. R., "Characterization of magnetic materials by impedance spectroscopy", Solid State Ionics, Vol. 40-41, pp. 220-223, 1990.

[54] Globus, A., & Duplex, P., "Separation of susceptibility mechanisms for ferrites of low anisotropy", IEEE Trans. Magn, Vol. 2, pp. 441-445, 1966.

[55] Chickazumi S. and Charap, S.H., "Physics of Magnetism", Krieger Pub. Co. p. 248, 1978.

[56] Alan H, Morrish, "The Physical Properties of Magnetism", John Wiley and Sons, 1966.

CHAPTER 3

SAMPLE FABRICATION

In this chapter, various experimental methods of sample preparation techniques of rare earth doped gadolinium oxide are described briefly. We describe also the effect of the preparation, calcinations and sintering process of the rare earth substituted Co-Cu-Zn ferrites with the general formula $Co_{0.40}Cu_{0.20}Zn_{0.40}Gd_xFe_{2-x}O_4$ are also given in this chapter. Standard solid state reaction technique was employed for sample preparation.

3.1 Composition of the studied ferrite system

In the present research Gd^{+3} based soft ferrites are synthesized and investigated. The ferrites under investigation are: $Co_{0.40}Cu_{0.20}Zn_{0.40}Gd_xFe_{2-x}O_4$ (with x = 0.000, 0.025, 0.050, 0.075, and 0.100).

3.2. Sample Preparation Techniques

Structural and magnetic properties of rare earth (Gd) substituted Co-Cu-Zn ferrites are greatly dependent on fabrication technique. There are various fabrication processes. Single crystals of Gd_2O_3 based dilute magnetic composition can be grown using chemical reaction. The most common methods for fabricating gadolinium oxide based diluted magnetic composition are given below:

a. Thin film fabrication technique

i. Pulsed laser deposition (PLD) (*c*-sapphire and *a*-sapphire)

ii. Reactive sputtering (*c*-sapphire and *a*-sapphire)

iii. Glass RF sputtering

iv. Magnetron sputtering

b Bulk sample fabrication technique:

i. Solid state reaction technique

ii. Bulk ZnO ion Implantation

iii. Chemical solution method.

3.2.1 Material Synthesis and Sample Preparation

Among all the processes the solid state reaction process is relatively less expensive. Maintenance of the critical conditions here is relatively easier than other processes. Other advantages of this technique are reproducibility, easy control, and obtaining sufficient products for measurements. With a careful control of contamination and impurity it is possible to fabricate a perfect dilute magnetic composition. The detail of the fabrication technique is described in the following section.

3.2.2 Solid State Reaction

In the solid state reaction method, the required composition is usually prepare from the appropriate amount of raw mineral oxides or carbonates by crushing, grinding and milling [1]. Solid state reaction occurs between apparently regular crystal lattices, in which the kinetic motion is very much restricted and it depends on the presence of lattice defects [2]. In solid state reaction method, appropriate amounts of two or more component of chemical compounds are carefully grinded together and mixed thoroughly in mortar with pestle or ball milling with appropriate homogenization. Solid oxides do not usually react together at room temperature over normal time scale and it is necessary to heat them at much higher temperatures. The ground powders are then calcined in air or oxygen at a temperature above 500 °C. Sometime this process is continued until the mixture is converted into the correct crystalline phase. The calcined powders are then further crushed into fine powders. The pellets or disc shaped and toroid shaped samples are made of these calcined powders using uniaxial or isostatic pressure. Sintering is carried out in the solid state,

at temperatures between 900-1600 °C, for times of typically 1-10 hours and in various atmospheres (e.g. Air, O2 and N2).

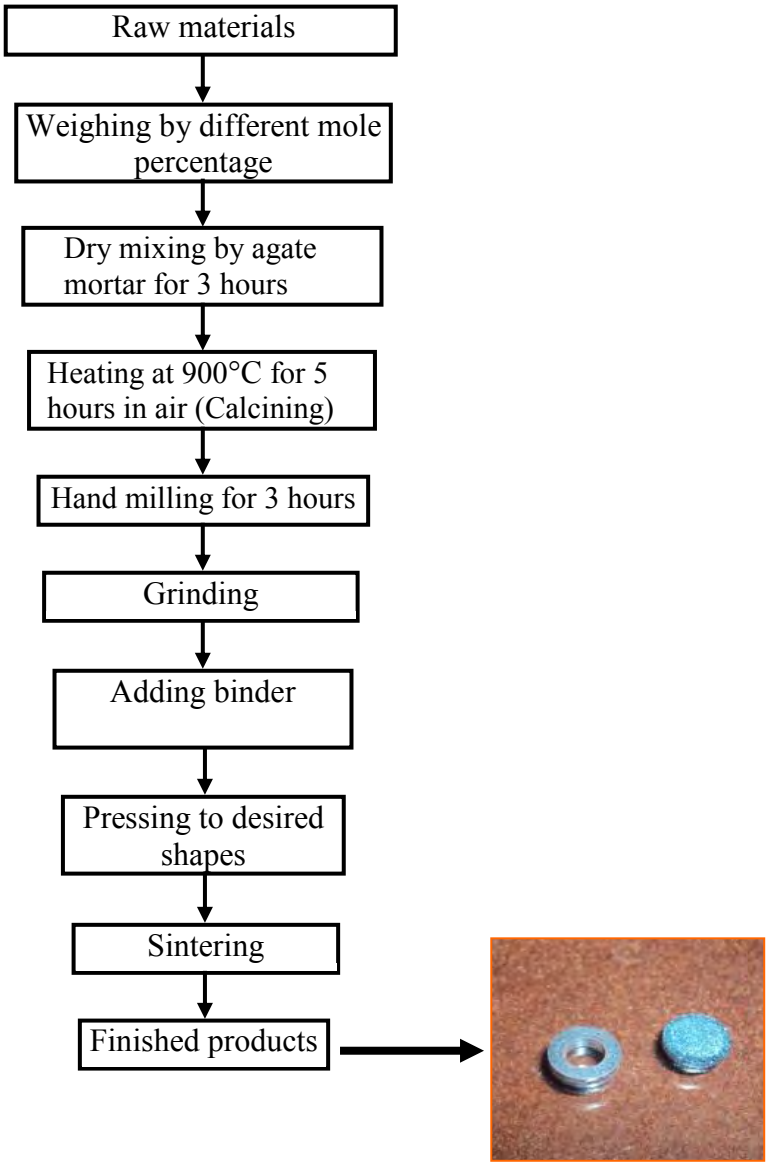

Fig.3.1 Flow chart for sample preparation and measurement by solid state reaction method.

3.2.3 Calcination and Sintering

Calcination is a heat treatment process, where the mixture of appropriate material is converted into the correct crystalline phase. Unwanted air molecules and impurities are also become evaporated while calcining. Sintering is used in order to get better densification and usually done at a higher temperature than calcination. Different grain sizes are found by sintering at different temperatures. After sintering

the compact solid becomes more homogeneous and free from unwanted impurities. Our samples were calcined at 900 °C for 5 hours in air and then sintered at different temperatures i.e. 1000, 1050, 1100 and 1150 °C for another 1 hour in air. The name of the furnace is *Carbolite Eurotherm 2408* made by England. The temperature ramp was 10^0C/min while rising and was 5°C/min while decreasing. After calcinations, samples got a different colour which indicated occurrence of chemical reaction among the compounds while calcining. After calcination two samples, formed two different coloured powder. The calcined powder was then further grinded for another three hours. Then the fine powder was pressed into pellets and toroids of 12 mm outer diameter and 6-7 inner diameter and 1-3 mm thick under a pressure of 10^4 *psi* for about 1-2 minutes using a uniaxial press. The name of uniaxial press that we used to palletized sample is *Will Corporation, Buehler ltd* made by U.S.A. The pellets and toroids formed inside the mould had a shinny surface. It was again placed in a boat and inserted into the furnace for sintering . The temperature ramp was 10ºC/min for heating and 5ºC/min for cooling.

3.3 Preparation of the present samples

Polycrystalline $Co_{0.40}Cu_{0.20}Zn_{0.40}Gd_xFe_{2-x}O_4$ (x= 0.000, 0.025, 0.050, 0.075 and 0.100) were prepared by a solid state reaction technique. Appropriate amount of commercially available high purity powders of Co_3O_4 (99.9%), CuO (99.99%), ZnO (99.9%), Gd_2O_3 (99.95%) and Fe_2O_3 (99.9%) were used as the raw materials. The exact amounts of compounds were calculated for each composition. Using those raw materials were weighed and mixed thoroughly by ball milling. Milling was carried out in a wet medium (distilled water) to increase the degree of mixing. The mixture was calcined at 900 ºC for 5 hours. The calcined powder again was crashed into fine powders.

(a) **(b)** **(c)**

Fig.3.2 (a) Carbolite Eurotherm 2408 and (b) uniaxial press(c) mortar with pestle Bangladesh University of Engineering and Technology (BUET).

From the fine powders, toroid and disk-shaped samples were prepared and sintered at various temperatures (1000, 1050, 1100 and 1150 °C). During sintering the samples were heated / cooled in various heating and cooling rates. It was expected that various heating/cooling rate was produce samples of various surface morphology, electric and magnetic properties. Two sets of each compositions were sintered at the above four temperatures. After sintering, one set of samples were kept for XRD analysis and another set of sample were rubbed and finished. First, the pellets and rings were rubbed using a sand paper (no. 800) then they were further rubbed using another fine sand paper (no.1200). Finally, finished samples were found. The thickness, inner diameter and outer diameter of each toroid shaped samples were measured. For disc shaped samples, thickness and diameter were measured.

Fig.3.3 Sample (a) disk shaped, (b) Toroid shaped.

References

[1] West, A. R., "*Solid State Chemistry and its applications*," pp. 5, (John Wiley & Sons, 1990).

[2] Schmalzried, H., "Solid State Reactions", Academic Press, New York (1974)

CHAPTER 4

EXPERIMENTAL TECHNIQUES

In this chapter we describe basic experimental techniques to measure the lattice parameters, structural and surface morphology and frequency dependent AC permeability of ferrite samples. We also describe the experimental technique for the measurement of magnetization. The transport properties and DC magnetization of the samples were also determined.

4.1 X-ray diffraction

Bragg reflection is a coherent elastic scattering in which the energy of the X-ray is not changed on reflection. If a beam of monochromatic radiation of wavelength λ is incident on a periodic crystal plane at an angle θ and is diffracted at the same angle as shown in Fig. 4.1, the Bragg diffraction condition for X-rays is given by

$$2d\,Sin\theta = n\lambda \qquad (4.1)$$

where d is the distance between crystal planes and n is the positive integer which represents the order of reflection. Equation (4.1) is known as Bragg law. This Bragg law suggests that the diffraction is only possible when $\lambda \leq 2d$ [1]. For this reason we cannot use the visible light to determine the crystal structure of a material. The X-ray diffraction (XRD) provides substantial information on the crystal structure.

X-ray diffraction was carried out with an X-ray diffractometer for the samples $Co_{0.40}Cu_{0.20}Zn_{0.40}Gd_xFe_{2-x}O_4$ (with x = 0.000, 0.025, 0.050, 0.075 and 0.100). For this purpose monochromatic *Cu-*K_α radiation was used. The lattice parameter for each peak of each sample was calculated by using the formula

$$a = d\sqrt{h^2 + k^2 + l^2} \qquad (4.2)$$

where *h*, *k* and *l* are the indices of the crystal planes. To determine the exact lattice parameter for each sample,

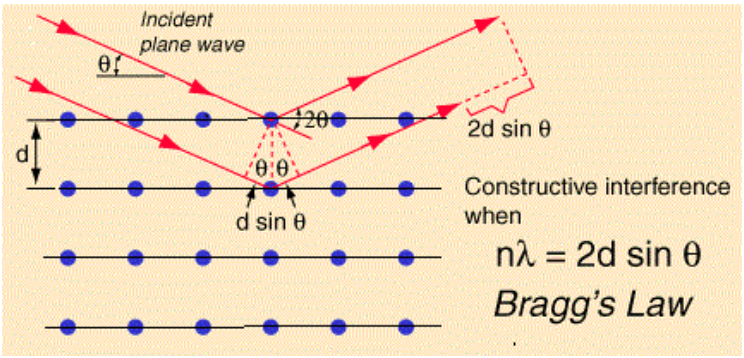

Fig.4.1 Bragg law of diffraction.

Nelson-Riley method was used. The Nelson-Riley function *F(θ)* is given as

$$F(\theta) = \frac{1}{2}\left[\frac{\cos^2\theta}{\sin\theta} + \frac{\cos^2\theta}{\theta}\right] \qquad (4.3)$$

The values of lattice constant 'a' of all the peaks for a sample are plotted against F(θ). Then using a least square fit method exact lattice parameter 'a_o' is determined. The point where the least square fit straight line cut the y-axis (i.e. at *F*(θ) = 0) is the actual lattice parameter of the sample.

The physical or bulk densities ρ_B of the samples were determined by Archimedes principle with water medium using the following expression [2]:

$$\rho_B = \frac{W\rho}{W - W'} g/cm^3 \qquad (4.4)$$

Where W is the weight of the sample in air, W' is the weight of the sample in the water and ρ is the density of water in room temperature.

The theoretical density ρ_{th} was calculated using following expression:

$$\rho_{th} = \frac{8M}{N_A a_o^3} g/cm^3 \qquad (4.5)$$

Where N_A is Avogadro's number (6.02×10^{23} mol^{-1}), M is the molecular weight. The porosity was calculated from the relation $P(\%) = \left\{ \left(\frac{\rho_{th} - \rho_B}{\rho_{th}} \right) \right\} \times 100\%$.

4.1.1 Phillips X′ Pert PRO X-ray diffractometer

X-ray diffraction (XRD) provides extensive information on the crystal structure. The wavelength of an X-ray is of the same order of magnitude as that of the lattice constant of crystals and this makes it so useful in structural analysis of crystal structure. To study the crystalline phases of the prepared samples PHILIPS PW3040 X'pert PRO X-ray diffractometer was used AEC, Dhaka, Bangladesh.

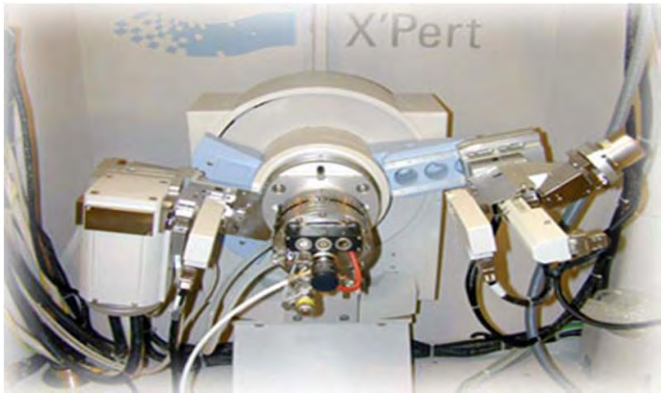

Fig.4.2 PHILIPS PW 3040 X'pert PRO X-ray diffractometer used for XRD.

The specimens were exposed to CuK_α radiation of wavelength, λ = 1.54178 Å with a primary beam of 40 kV and 30 mA with a sampling pitch of 0.02° and time for each step data collection was 1.0 sec. A 2θ scan was taken from 10° to 90° to get possible

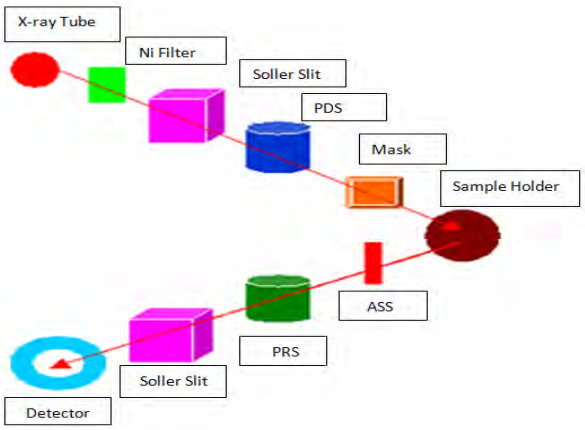

Fig.4.3 Block diagram of the PHILIPS PW 3040 X'Pert PRO XRD system.

fundamental peaks where Ni filter was used to reduce CuK_{β} radiation. All the data of the samples were analyzed using computer software "X′ PERT HIGHSCORE".

4.1.2 Powder X-ray diffractometer

Powder X- ray diffraction is perhaps the most widely used X–ray diffraction technique for characterizing materials; Powder diffraction is commonly used to identify unknown substances, by comparing diffraction database maintained by the International Center for Diffraction Data. It may also be used to characterize heterogeneous solid mixtures to determine relative abundance of crystalline compounds and, when coupled with lattice refinement technique, such as Rietveld refinement, can provide structural information on unknown materials. Powder diffraction is also a common method for determining strains in crystalline materials.

Powder diffraction data can be collected using either transmission or reflection geometry. Because the particles in the powder sample are randomly oriented, these two methods will yield the same data. Powder diffraction data are measured using the Philips XPERT PRO diffractometer, which measures data in the reflection mode and is used mostly with powder or solid samples.

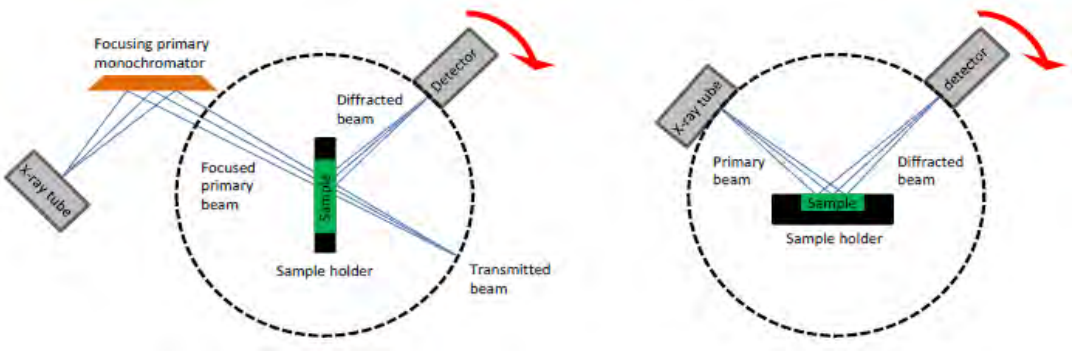

Fig.4.4 X-ray diffraction, (a) classic transmission geometry and (b) Classic reflection geometry.

Diffraction can occur when electromagnetic radiation interacts with a periodic structure whose distance is about the same as the wavelength of the radiation. This

technique uses the principle that waves interacting with atomic planes in a material will exhibit the phenomenon of diffraction. X-rays incident on a sample are scattered off at an equal angle. At certain angles of incidence, x-rays scattering off of neighboring parallel planes of atoms will interferer destructively. At other angles, these waves will interfere constructively and result in a large output signal at those angles. The XRD technique is based on Bragg's principle.

4.2 Surface morphology and microstructure

The microstructural study was performed in order to have an insight of the grain structures. The samples of different compositions and sintered at different temperatures were chosen for this purpose. The samples were visualized under a high-resolution Scanning Electron Microscope (SEM) and then photographed. Average grain sizes (grain diameter) of the samples were determined from SEM micrographs by linear intercept technique [3]. To do this, several random horizontal and vertical lines were drawn on the micrographs. Therefore, we counted the number of grains intersected and measured the length of the grains along the line traversed. Finally the average grain size was calculated.

4.3 Scanning Electron Microscope

SEM is a type of electron microscope that creates various images (surface morphology) by focusing a high energy beam of electrons onto the surface of a sample and detecting signals from the interaction of the incident electron with the sample's surface. The type of signals gathered in a SEM varies and can include secondary electrons, characteristic x-rays, and back scattered electrons. In a SEM, these signals come not only from the primary beam impinging upon the sample, but from other interactions within the sample near the surface. The SEM is capable of

producing high resolution images of a sample surface in its primary use mode, secondary electron imaging. Due to the manner in which this image is created, SEM images have great depth of field yielding a characteristic three-dimensional appearance useful for understanding the surface structure of a sample. This great depth of field and the wide range of magnifications are the most familiar imaging mode for specimens in the SEM. Characteristic x-rays are emitted when the primary beam causes the ejection of inner shell electrons from the sample and are used to tell the elemental composition of the sample. The back-scattered electrons emitted from the sample may be used alone to form an image or in conjunction with the characteristic x-rays as atomic number contrast clues to the elemental composition of the sample. In the present study, the SEM micrographs of different sintered pellets were taken using a field emission scanning electron microscope (FESEM, JEOL, JSM 7800F).

Fig.4.5 Scanning Electron Microscope (SEM).

4.3.1 Scanning process and image formation

In a typical SEM, an electron beam is thermionically emitted from an electron gun fitted with a tungsten filament cathode. Tungsten is normally used in thermo ionic

electron guns because it has the highest melting point and lowest vapor pressure of all metals, thereby allowing it to be heated for electron emission, and because of its low cost. The electron beam, which typically has an energy ranging from a few 100 eV to 40 keV, is focused by one or two condenser lenses to a spot about 0.4 nm to 5 nm in diameter. The beam passes through pairs of scanning coils or pairs of deflector plates in the electron column, typically in the final lens, which deflect the beam in the x and y axes so that it scans in a raster fashion over a rectangular area of the sample surface. When the primary electron beam interacts with the sample, the electrons lose energy by repeated random scattering and absorption within a teardrop-shaped volume of the specimen known as the interaction volume, which extends from less than 100 nm to around 5 μm into the surface. The size of the interaction volume depends on the electron's landing energy, the atomic number of the specimen and the specimen's density. The energy exchange between the electron beam and the sample results in the reflection of high-energy electrons by elastic scattering, emission of secondary electrons by inelastic scattering and the emission of electromagnetic radiation, each of which can be detected by specialized detectors. The beam current absorbed by the specimen can also be detected and used to create images of the distribution of specimen current. Electronic amplifiers of various types are used to amplify the signals which are displayed as variations in brightness on a cathode ray tube. The raster scanning of the CRT display is synchronized with that of the beam on the specimen in the microscope, and the resulting image is therefore a distribution map of the intensity of the signal being emitted from the scanned area of the specimen. The image may be captured by photography from a high resolution cathode ray tube, but in modern machines is digitally captured and displayed on a computer monitor.

4.4 Complex permeability measurement

For high frequency application, the desirable property of a ferrite is high permeability with low loss. One of the most important goals of ferrite research is to fulfill this requirement. The techniques of permeability measurement and frequency characteristics of the present samples are described in the following way. Measurements of permeability normally involve the measurements of the change in self-inductance of a coil in presence of the magnetic core. The behavior of a self-inductance can now be described as follows. We assume an ideal loss less air coil of inductance L_0. On insertion of a magnetic core with permeability μ, the inductance will be μL_0. The complex impedance Z of this coil [3] can be expressed as follows:

$$Z = R + jX = j\omega L_0 \mu = j\omega L_0 (\mu' - j\mu'') \tag{4.6}$$

Where the resistive part is $R = \omega L_0 \mu''$ (4.7)

and the reactive part is $X = \omega L_0 \mu'$ (4.8)

The RF. permeability can be derived from the complex impedance of a coil, *Z*, given by equation (4.6). The core is taken as toroidal to avoid demagnetizing effects. The quantity L_o is derived geometrically as shown in section 4.5.

4.5 Frequency characteristics of the present samples

The frequency dependent complex permeability spectra of mentioned ferrite sample were investigated using a Wayne Kerr Precision Impedance Analyzer (model no. 6500B) in the solid state physics laboratory, Bangladesh University of Engineering and Technology (BUET).which is shown in Fig.4.7. The complex permeability measurements on toroid shaped specimens were carried out at room temperature on all the samples in the frequency range 100 Hz - 120 MHz. The real

part ($\mu_i^{/}$) and imaginary part ($\mu_i^{//}$) of the complex permeability were calculated using the following relations [4]: $\mu_i^{/} = L_s / L_0$ and $\mu_i^{//} = \mu_i^{/} \tan\delta$, where L_s is the self-inductance of the sample core (Fig. 3.5) and $L_0 = \mu_o N^2 h \Big/ 2\pi(\ln \frac{r_o}{r_i})$ is derived geometrically. Here L_o is the inductance of the winding coil without the sample core, μ_0 is ithe permeability constant in the free space and has a value $4\pi \times 10^{-7} WA^{-1}$. N is the number of turns of the coil (N = 4), measurements of the toroidal sample, $r_o =$ outer radius, $r_i =$ inner radius, $h =$ height.

The relative quality factor is determined from the ratio RQF $= \frac{\mu_i^{/}}{\tan\delta}$.

Fig.4.6 winding of four turns on the sample core.

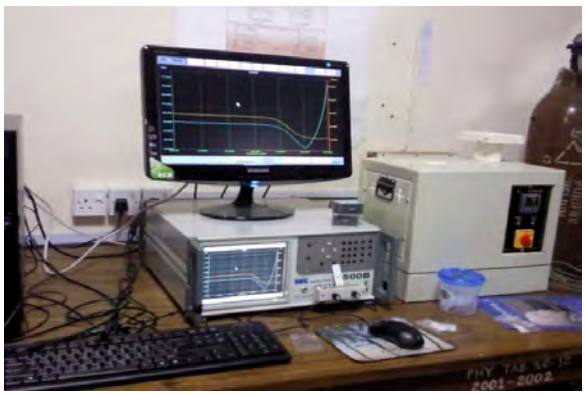

Fig.4.7 Wayne Kerr Impedance Analyzer (Model No. 6500B) in experimental Solid State Physics laboratory, BUET.

4.6 Transport properties

4.6.1 Dielectric Constant

The overall dielectric constant (ε') of an insulator material is given by the relation:

$$D = \varepsilon E_0 = \varepsilon_0 \varepsilon' E_0 \tag{4.9}$$

Where D represents the electric displacement, E the electric field in the dielectric, ε' the dielectric constant and ε_0 permittivity of vacuum. The ε' is an intrinsic property of a material and a measure of the ability of the material to store electric charge relative to vacuum. It is measured indirectly from the capacitance of a capacitor in which the material is used as electrode separator or dielectric.

The dielectric constant ε', total charge Q (coulombs) and capacitance C (farads) can be developed as follows:

$$\varepsilon' = \frac{D}{\varepsilon_0 E} = \frac{Q/S}{\varepsilon_0 V/d} \tag{2.9}$$

Therefore, $$Q = \varepsilon_0 \varepsilon' \frac{S}{d} V = CV \tag{4.10}$$

Where, $$C = \varepsilon_0 \varepsilon' \frac{S}{d} \tag{4.11}$$

$$C_0 = \varepsilon_0 \frac{S}{d} \tag{4.12}$$

And $$\varepsilon' = \frac{C}{C_0} = \frac{\varepsilon}{\varepsilon_0} \tag{4.13}$$

Here, *S* represents the area of the capacitive cell, *d* its thickness (or gap between the electrodes), C_0 and C the respective capacitance of the capacitor with air and material, V the voltage across the cell, ε the material permittivity (F/m). Thus, represents the ratio of the permittivity or charge storage capacity relative to air or vacuum as dielectric. A real capacitor can be represented with a capacitor and a resistor.

It is clear from equation 4.10 that for a given size capacitor and applied voltage, the higher the ε′ higher the capacitance of the capacitor. This is the only variable left with the material scientist to increase the value of capacitance per unit volume of capacitor for modern electronics applications.

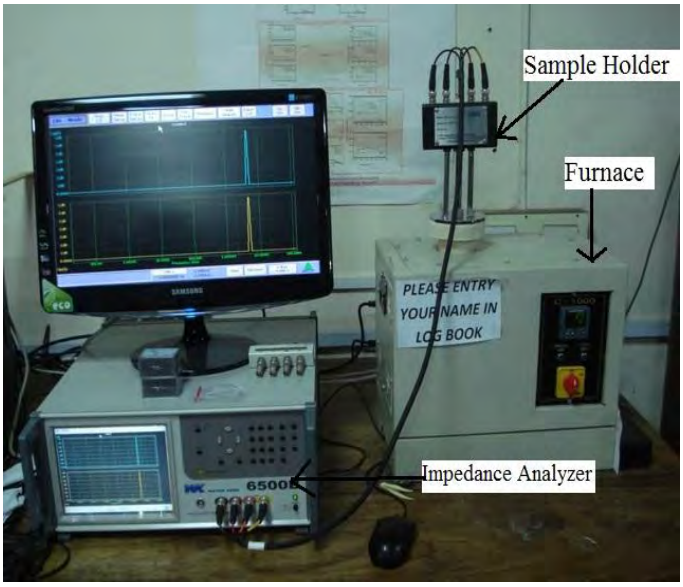

Fig.4.8 (a) Setup for temperature dependent measurement in experimental Solid State Physics laboratory, BUET.

4.6.2 Dielectric Loss

Friction is a macroscopic concept and its explanation in terms of models conceived at a microscopic level has presented difficulties in many branches of physics. Dielectric loss is a special type of friction and the classical and quantum statistical mechanical theories of dielectric loss present the familiar difficulties of principle encountered in a theory of dissipation. Every type of dissipation (dielectric loss) is connected with motions of charge carrier. The effect of their movements in an electric field is called polarization. The total polarization is the sum of various contributions, e.g. electronic polarization due to the relative displacement of electrons

and nuclei, dipolar polarization due to orientation of dipoles, and interfacial or Maxwell-Wagner polarization when there are boundaries between the components of a heterogeneous system. The occurrence of dielectric loss can generally be understood as follows: at very low frequencies the polarization easily follows the alternating field, thus its contribution to the dielectric constant is maximal, and no loss occurs. At very high frequencies the field alternates too fast for polarization to arise and there is no contribution to the dielectric constant, and no energy lost in the medium. Somewhere between these two extremes the polarization begins to lag behind the field, and energy is dissipated. An ideal dielectric would allow no flow of electronic charge, only a displacement of charge via polarization. If a plate of such ideal material was placed between the capacitive cell and a dc voltage was applied, the current through the circuit would decay exponentially to zero with time. But this would not be case if an alternating (sine wave) electric field were applied. In this case equation may be written as:

$$Q = CVe^{i\omega t} \tag{4.14}$$

Therefore

$$I = \frac{dQ}{dt} = i\omega CV = i\omega C_0 \varepsilon_0 \varepsilon' V \tag{4.15}$$

Here, I represent the current flow on discharge of the capacitor in time t. For real dielectric material, the current I has two vector components, real I_R and imaginary I_C.

The condition of a loss dielectric analogous of a resistance in parallel with the capacitor. The current I_c represent a (watt less) capacitive current proportional to the charge stored in the capacitor. It is frequency dependent and leads the voltage by 90^0. On the other hand, the current I_R is ac conduction current in phase with the voltage V, which represents the energy loss or power dissipated in the dielectric. The resultant

angle between the current and the voltage is θ somewhat less than 90^0. The current in real capacitor lags slightly behind what it would be in an ideal capacitor.

Equation can be written for real and imaginary part,

$$I = I_R + I_C \tag{4.16}$$

$$= \omega C_0 \varepsilon_0 \varepsilon' V + i\omega C_0 \varepsilon_0 \varepsilon'' V \tag{4.17}$$

By definition, $$\tan\delta = \frac{\varepsilon''}{\varepsilon'} \tag{4.18}$$

Dielectric loss often attributed to ion migration, ion vibration & deformation and electric polarization. Ion migration is particularly important and strongly affected by temperature and frequency. The losses due to ion migration increase at low frequency and the temperature increases.

The imaginary part of dielectric constant (ε″) of the sample was calculated using relation: ε″=ε′∗ tanδ; where tanδ is the dielectric loss tangent.

The ac conductivity was calculated according to the relation $\zeta_{ac} = d/(A \times R_{ac})$; here R_{ac} is the ac resistance. The electrical conductivity of most materials can be expressed as: $\zeta\ (\omega, T) = \zeta_{ac}(T) + \zeta_{ac}(\omega,T)$; where ζ_{dc} is the conductivity and depends only on temperature. The second term ζ_{ac} is the ac is the ac conductivity, which depends on temperature and frequency. The frequency dependent ζac is expressed by the empirical formula: $\zeta_{ac}(\omega, T) = A\omega^n$; where A and n are the constants which depend both on temperature and composition; n dimensionless, whereas A has units of $\zeta_{ac.}$

4.6.3 Impedance spectroscopy

AC measurement are often made with a wheatstone-bridge-type of apparratus (impedance analyzer or LCR meter) in which the resistance R and capacitance C of the sample are measured and balanced against variable resistors and capacitors. The impedance |Z| and the phase difference (θ) between the voltage and current are

measured as a function of frequency for the given sample and the technique is called impadence spectroscopy. Analysis of the data is carried out by flotting the imaginary part of impedance $Z' = |Z|\cos\theta$ against the real part $Z'' = |Z|\sin\theta$ on a complex plane called the impedance plot. An impedance plot with linear scale is used to analyze the equivalent circuit as follows. Impedance plot of pure resistor is a point on real axis and that of pure capacitor is a straight line coinciding with the imaginary axis. The impedance of a parallel RC combination is by the following relation:

$$Z^* = Z' - j\,Z'' = R / (1 + j\omega RC)$$

After simplification, one gets

$$(Z' - R/2)^2 + Z''^2 = (R/2)^2$$

This represents the equation of circle with radius R /2 and centre at (R /2, 0). Thus a plot of Z' vs Z'' (as a parametric function of Q) will result in a semicircle of radius R /2 and this plot is called Nyquist plot. The time constant of the simple circuit is defined as $\eta = RC = 1/\omega_n$. This corresponds to the relaxation time of the sample and the characteristic frequency lies at the peak of the semi-circle. In an ideal polycrystalline sample, the impedance plot exhibits an arc corresponding to the grain boundary behavior and a spike at the lowest frequency corresponding to the electrode effect.

4.6.4 Modulus spectroscopy

The complex modulus spectroscopy study gives the information regarding the distribution parameters of different micro regions in the polycrystalline materials, such as gain, grain boundary and electrode interface. Different mechanism involved in the relaxation as well as in ac conduction process can be resolved by plotting the modulus at different frequencies in the complex plane, and is found very effective in separating the contributions of various factors such as bulk effect, grain boundary effect, and interfaces. Also the use of modulus spectroscopy plot is particularly useful for

separating the components with similar resistance but different capacitance. Dielectric relaxation studies have been carried out in the complex modulus M* formalism. The real and imaginary part of electric modulus was obtained from the impedance data in accordance with the relation:

$$M' = \varepsilon'/ (\varepsilon'^2 + \varepsilon''^2) = \omega C_o Z'' \text{ and } M'' = \varepsilon'' / (\varepsilon'^2 + \varepsilon''^2) = \omega CoZ'.$$

4.7 DC magnetization measurement technique

The VSM (vibrating sample magnetometer) technique is used to measure the change of magnetization of materials as a function of an external field, which enables to identify their magnetic nature. It is a versatile and sensitive method of measuring magnetic properties developed by S. Foner [5] and is based on the flux change in a coil when the sample is vibrated near it. As explained earlier, para-, dia- and ferromagnetic materials will have a different reaction to the applied field. In ferromagnetic samples, a hysteresis loop is expected. The degree of bending of the M-H graph represents the amount of ferromagnetism in the examined sample. The principle of the VSM is, as its name reveals, based on the mechanical vibration of a magnetic sample in a homogeneous magnetic field, which will produce a change in the magnetic flux in the neighborhood of the sample. The sample is vibrating sinusoidally at small fixed amplitude with respect to stationary pick-up coils. According to Faradays law, an electromagnetic field will be induced, proportional to the rate of the flux change, as

$$V(t) \propto \frac{d\Phi}{dt} \qquad (4.19)$$

The resulting field change ∂B (t) at a point r inside the detection coils induces a voltage. The field B is given by the dipolar approximation, assuming small

dimensions of the magnetized sample in comparison to its distance from the detection coils

$$\vec{B}(r) = \frac{\mu_0}{4\pi} \{\frac{\vec{m}}{r^3} - \frac{3(\vec{m}\cdot\vec{r})\vec{r}}{r^3}\} \qquad (4.20)$$

Where, *m* is the magnetic moment of the magnetized sample.

4.7.1 Vibrating Sample Magnetometer (Micro Sense, EV9)

Fig.4.9 VSM machine set up at Material Science Division, AECD.

The Vibrating Sample Magnetometer (VSM) is designed to continuously measure the magnetic properties of materials as a function of temperature and field. In this type of magnetometer, the sample is vibrated up and down in a region surrounded by several pickup coils. The magnetic sample is thus acting as a time-changing magnetic flux, varying inside a particular region of fixed area. From Maxwell's law it is known that a time varying magnetic flux is accompanied by an electric field and the field induces a voltage in pickup coils. This alternating voltage signal is processed by a control unit system, in order to increase the signal to noise ratio. The result is a measure of the magnetization of the sample.

4.7.2 Working principle of VSM

If a sample is placed in a uniform magnetic field, created between the poles of an electromagnet, a dipole moment will be induced. If the sample vibrates with sinusoidal motion a sinusoidal electrical signal can be induced in suitable placed pick-up coils. The signal has the same frequency of vibration and its amplitude will be proportional to the magnetic moment, amplitude, and relative position with respect to the pick-up coils system. Figure 4.10 shows the block diagram of vibrating sample magnetometer. The sample is fixed to a sample holder located at the end of a sample rod mounted in an electromechanical transducer. The transducer is driven by a power amplifier which itself is driven by an oscillator at a frequency of 90 Hertz. So, the sample vibrates along the Z axis perpendicular to the magnetizing field. The latter induced a signal in the pick-up coil system that is fed to a differential amplifier. The output of the differential amplifier is subsequently fed into a tuned amplifier and an internal lock-in amplifier that receives a reference signal supplied by the oscillator.

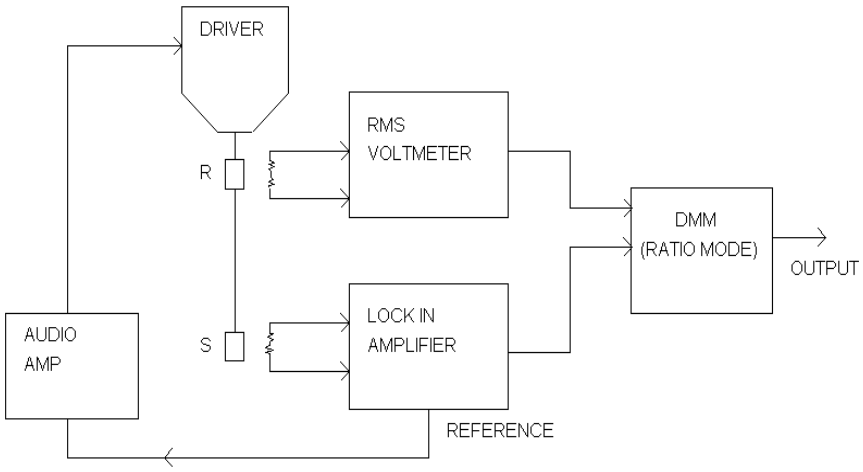

Fig.4.10 Block diagram of vibrating sample magnetometer.

The output of this lock-in amplifier, or the output of the magnetometer itself, is a DC signal proportional to the magnetic moment of the sample being studied. The electromechanical transducer can move along X, Y and Z directions in order to find the saddle point. Calibration of the vibrating sample magnetometer is done by

measuring the signal of a pure Ni standard of known saturation magnetic moment placed in the saddle point. The basic instrument includes the electromechanical system and the electronic system (including a personal computer). Laboratory electromagnets or superconducting coils of various maximum field strengths may be used.

The measurements of the field dependence of the magnetization for bulk materials were performed using the VSM Micro Sense (model EV9), The EV9 Vibrating Sample Magnetometer can reach fields up to 26kOe at a sample space of 5 mm and 21.5kOe with the temperature chamber in place. The VSM was able to deliver fields up to 2 Tesla. The VSM was able to detect magnetic moments down to 0.5 emu. Since only room temperature measurements were performed, a cryostat assembly was not needed.

References

[1] Kittel, C., "Introduction to Solid State Physics", 7th edition, Jhon Wiley & Sons, Inc., Singapore 1996.

[2] Gadkari, A. B., Shinde, T. J., Vasambekar, P. N.; "Structural and magnetic properties of nanocrystalline Mg-Cd ferrites prepared by oxalate co-precipitation method," J. Mater Sci: Mater Electron, Vol. 21(1), pp. 96-103, 2010.

[3] Goldman, A. Handbook of Modern Ferromagnetic Materials, Kulwer Acad. Pub, Boston, U.S.A 1999.

[4] Akther Hossain, A. K. M., "Investigation of colossal magnetoresistance in bulk and thick film magnetites", *Ph. D. Thesis*, Imperial College, London, 1998.

[5] Foner, S., "Versatile and sensitive Vibrating Sample Magnetometer", Rev. Sci. Instr. Vol. 30(7), pp. 548-557, 1959.

CHAPTER 5

RESULTS AND DISCUSSION

In this section structural and surface morphology of $Co_{0.4}Cu_{0.2}Zn_{0.4}Gd_xFe_{2-x}O_4$ are investigated. The gadolinium substituted polycrystalline $Co_{0.4}Cu_{0.2}Zn_{0.4}Gd_xFe_{2-x}O_4$ ranging from x=0.000 to x=0.100 have been prepared been prepared by standard solid state reaction technique. XRD patterns confirm single phase and formation of cubic structure. The magnetic properties such as complex initial permeability of the ferrites investigated in the frequency range (10^4 kHz -120 MHz) by Wayne Kerr Impedance Analyzer (model no.6500B). The DC magnetization and transport properties of the sample at T_s= 1100 ºC are also studied. The influence of Gd^{3+} ion substitution and sintering temperature on these parameters of $Co_{0.4}Cu_{0.2}Zn_{0.4}Gd_xFe_{2-x}O_4$ ferrites are discussed.

5.1 XRD analysis of the polycrystalline $Co_{0.4}Cu_{0.2}Zn_{0.4}Gd_xFe_{2-x}O_4$

Room temperature XRD patterns for various $Co_{0.40}Cu_{0.20}Zn_{0.40}Gd_xFe_{2-x}O_4$ with x=0.000, x=0.025, x=0.050, x=0.075 and 0.100 sintered at 1100˚C are shown in fig.5.1. All peaks observed in XRD patterns are identified with their miller indices indicate single phase and formation of cubic spinel structure having no impurity peak

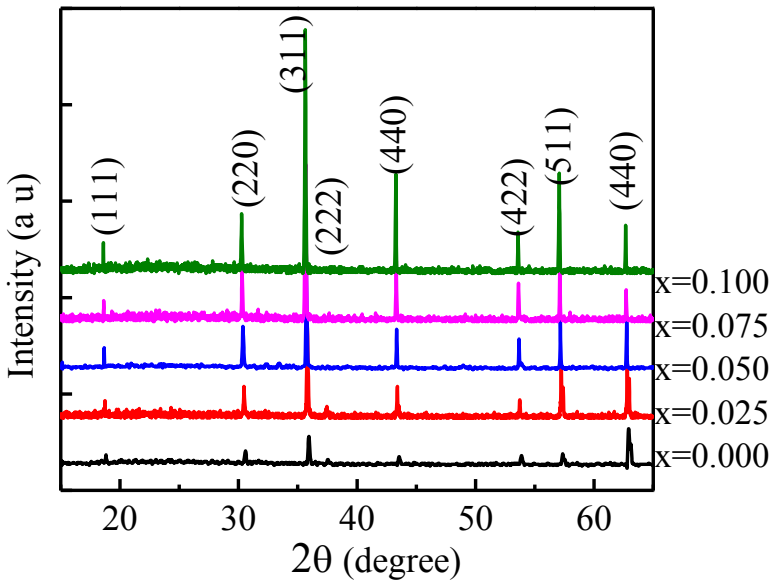

Fig.5.1 The X-ray diffraction patterns of $Co_{0.4}Cu_{0.2}Zn_{0.4}Gd_xFe_{2-x}O_4$ sintered at 1100 ºC in air.

is formed as all the peaks in pattern match well with characteristic reflections reported as before [1]. Peaks of the observed diffraction pattern have been well indexed to the

crystal plane of spinel ferrite (111), (220), (311), (222), (440), (422), (511), and (440) plane respectively. The positions of the peaks are in good agreement with the earlier reported value [2, 3].

5.2 Lattice Constants of the polycrystalline $Co_{0.4}Cu_{0.2}Zn_{0.4}Gd_xFe_{2-x}O_4$

The values of lattice parameters, *a*, obtained from each crystal plane are plotted against Nelson-Riley function (equation 4.3 chapter 4). The values of lattice parameters were estimated from the extrapolation of these lines to F (θ) = 0 or θ = 90°. From the lattice parameter, *a* Vs F (θ) curve, precise lattice constant, 'a_o' is determined for each composition. Fig. 5.2(a) shows *a* Vs F (θ) curve for various $Co_{0.4}Cu_{0.2}Zn_{0.4}Gd_xFe_{2-x}O_4$ sintered at 1100^0C. Lattice constants of other samples are calculated in a similar way. The lattice constant, a_o of various $Co_{0.4}Cu_{0.2}Zn_{0.4}Gd_xFe_{2-x}O_4$ are plotted as a function of Gd content, as shown in Fig. 5.3. In the present case the lattice constant varies from 8.4127 Å to 8.4276 Å as presented in Table 5.1.

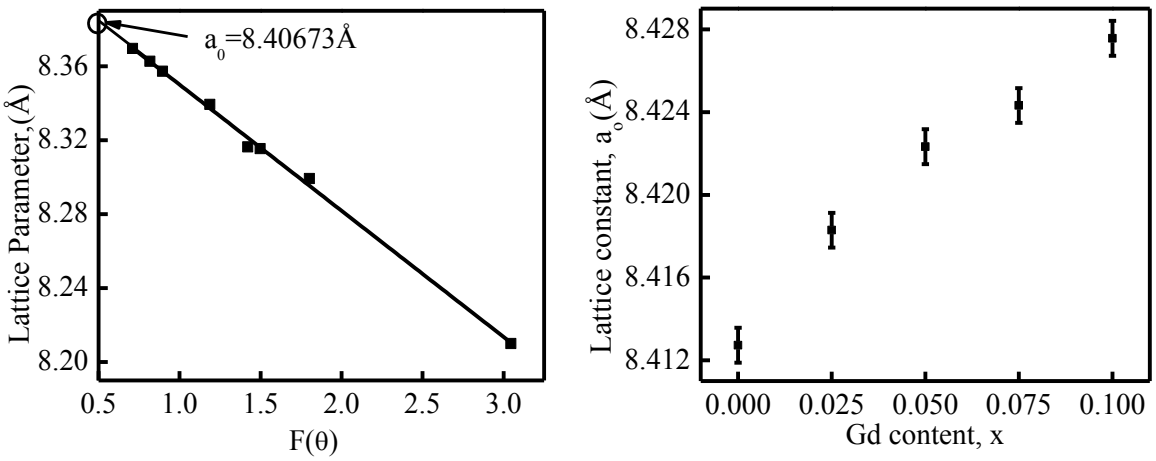

Fig.5.2 (a) Variation of lattice parameter with F(θ) and (b) Variation of the lattice constant a_o with Gd content.

It is clear from Fig. 5.3 that the lattice constant, a_o increases with the increase of Gd^{3+} content that follows Vegard's law in the whole composition range under present

investigation as shown by solid line. The values of lattice constant for various $Co_{0.4}Cu_{0.2}Zn_{0.4}Gd_xFe_{2-x}O_4$ are listed in the Table 5.1. This increase in lattice constant with Gd^{3+} content can be explained in the basis of ionic radii. The ionic radii of the cataions used in $Co_{0.4}Cu_{0.2}Zn_{0.4}Gd_xFe_{2-x}O_4$ are 0.91Å (Gd^{3+}) and 0.64 Å (Fe^{3+}) [5]. Here Fe^{3+} is substituted by Gd^{3+}. So increase in lattice constant a_o is expected with increasing Gd^{3+} content. The mean ionic radius of the compositions under investigation has the nominal chemical formula $Co_{0.4}Cu_{0.2}Zn_{0.4}Gd_xFe_{2-x}O_4$ Therefore, the mean ionic radius of the variant ions for composition $Co_{0.4}Cu_{0.2}Zn_{0.4}Gd_xFe_{2-x}O_4$ can be written as

$$r_{(variant)} = xr_{Gd} + (2\text{-}x)r_{Fe} \qquad (1)$$

Where r_{Gd} is the radius of Gd^{3+} (= 0.91Å) and r_{Fe} is the ionic radius of Fe^{3+} (=0.64Å) [5]. The variation of $r_{(variant)}$ with Gd content is shown in Fig. 5.3, where it increases with increasing Gd content.

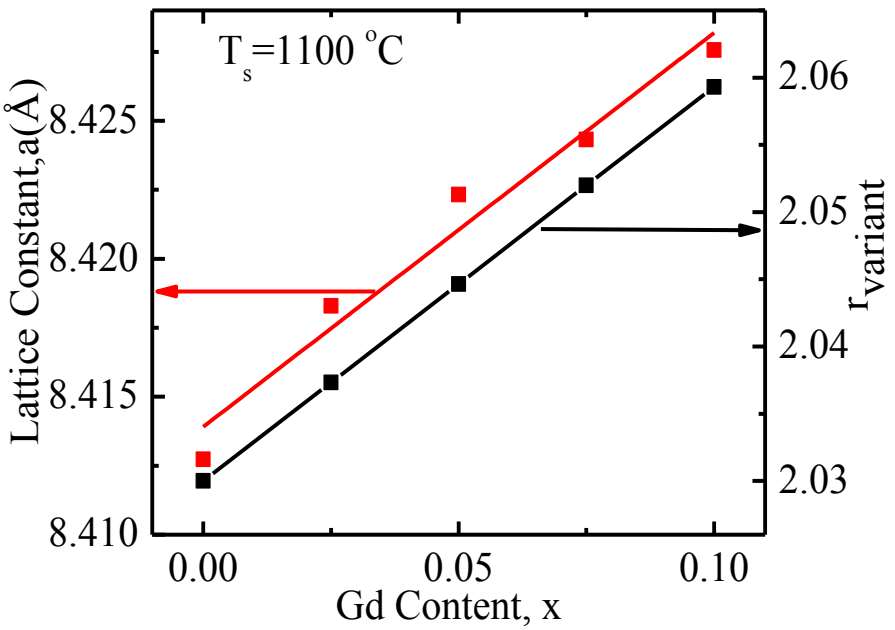

Fig.5.3 Variation of the lattice constant a_o, and $r_{varient}$ as a function of Gd content for $Co_{0.4}Cu_{0.2}Zn_{0.4}Gd_xFe_{2-x}O_4$ sintered at 1100 ºC in air.

Table 5.1 The lattice constant, density, porosity, grain size, natural resonance frequency, maximum Quality factor and initial permeability of the various $Co_{0.4}Cu_{0.2}Zn_{0.4}Gd_xFe_{2-x}O_4$ sintered at various temperatures with fixed dwell time 3h.

x	T_s (^0C)	a_0 (A^0)	$P_{x\text{-}ray}$ (g/cm^3)	P_{bulk} (g/cm^3)	P (%)	Grain Size (μm)	Q_{max}	μ_i' (at10kHz)
0.000	1000	8.4127	5.31	4.73	11	0.85	1648	33
	1050			4.75	11	0.85	1889	33
	1100			4.81	9	1.77	1912	35
	1150			4.78	10	1.49	1274	27
0.025	1000	8.4183	5.36	4.78	11	0.99	2233	34
	1050			4.82	10	1.47	2494	34
	1100			4.87	9	2.08	2628	36
	1150			4.84	10	1.92	1318	25
0.050	1000	8.4223	5.42	4.84	11	1.77	2452	35
	1050			4.88	10	1.83	2525	35
	1100			4.93	9	2.81	3395	38
	1150			4.91	9	2.74	2049	30
0.075	1000	8.4243	5.47	4.89	11	1.54	1898	33
	1050			4.94	10	1.62	2499	34
	1100			4.99	9	2.29	2714	35
	1150			4.96	9	2. 21	1787	27
0.100	1000	8.4276	5.51	4.93	11	1.50	1737	32
	1050			4.99	9	1.60	2414	33
	1100			5.05	8	2.26	2521	34
	1150			5.01	8	2.16	1673	25

5.3 Density and porosity of the polycrystalline $Co_{0.4}Cu_{0.2}Zn_{0.4}Gd_xFe_{2-x}O_4$

Density plays an important role in controlling the properties of polycrystalline ferrites. A significant increase in the bulk density is observed with the *Gd* content (as shown in fig.5.5). Theoretical density, ρ_{th}, bulk density, ρ_B and porosity, P, of the various $Co_{0.4}Cu_{0.2}Zn_{0.4}Gd_xFe_{2-x}O_4$ are tabulated in the Table 5.1. The ρ_{th} increases with increasing lattice constant, a_o in the *Gd* substituted various $Co_{0.4}Cu_{0.2}Zn_{0.4}Gd_xFe_{2-x}O_4$. It increases because the molecular weight of the each sample increases significantly with the addition Gd^{3+} content. Both theoretical and bulk density increase in a similar fashion and porosity decreases with the increase of Gd content in $Co_{0.4}Cu_{0.2}Zn_{0.4}Gd_xFe_{2-x}O_4$ for a fixed sintering temperature, as shown in Fig. 5.4.

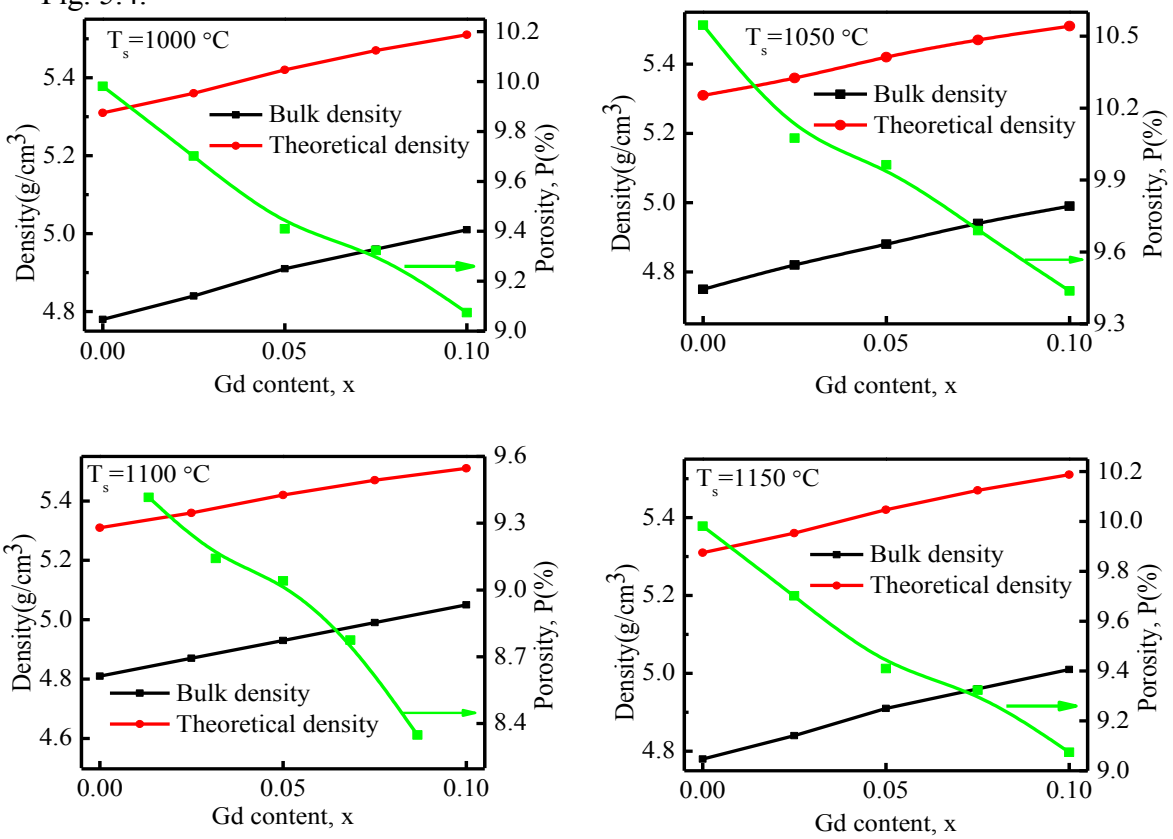

Fig.5.4 The variation of theoretical density (ρ_{th}) and bulk density (ρ_B) and porosity (P) with Gd content in $Co_{0.4}Cu_{0.2}Zn_{0.4}Gd_xFe_{2-x}O_4$.

Fig.5.6 shows that the variation of ρ_{Bulk} and P with the variation of sintering temperature for $Co_{0.4}Cu_{0.2}Zn_{0.4}Gd_xFe_{2-x}O_4$. It is observed that the density of all samples increases with increasing sintering temperature from 1000 to 1100 °C and then it decreases for further increase in sintering temperature. On the other hand, porosity (P) of all samples decreases with increasing sintering temperature up to 1100 °C and an increasing trend is shown beyond it. The increase in density with sintering temperature is expected. It is also observed that the ρ_{th} of each sample is greater than that of ρ_{Bulk} because there may be some pores which were formed and developed during sample preparation or the sintering process in the bulk sample [6, 7].

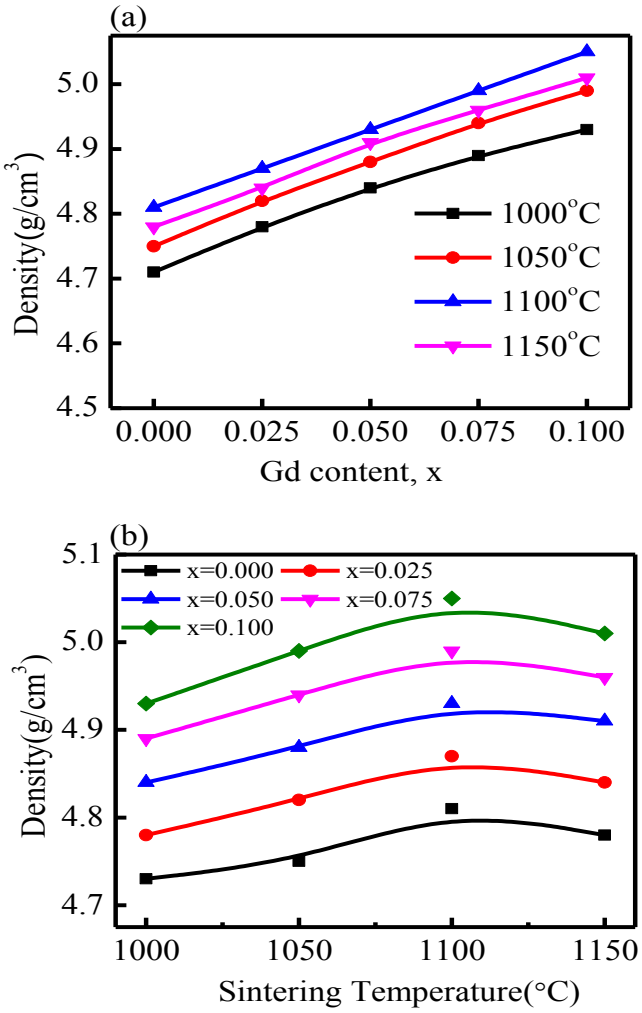

Fig.5.5 (a) Variation of density with respect to Gd content, x and (b) sintering temperature (°C).

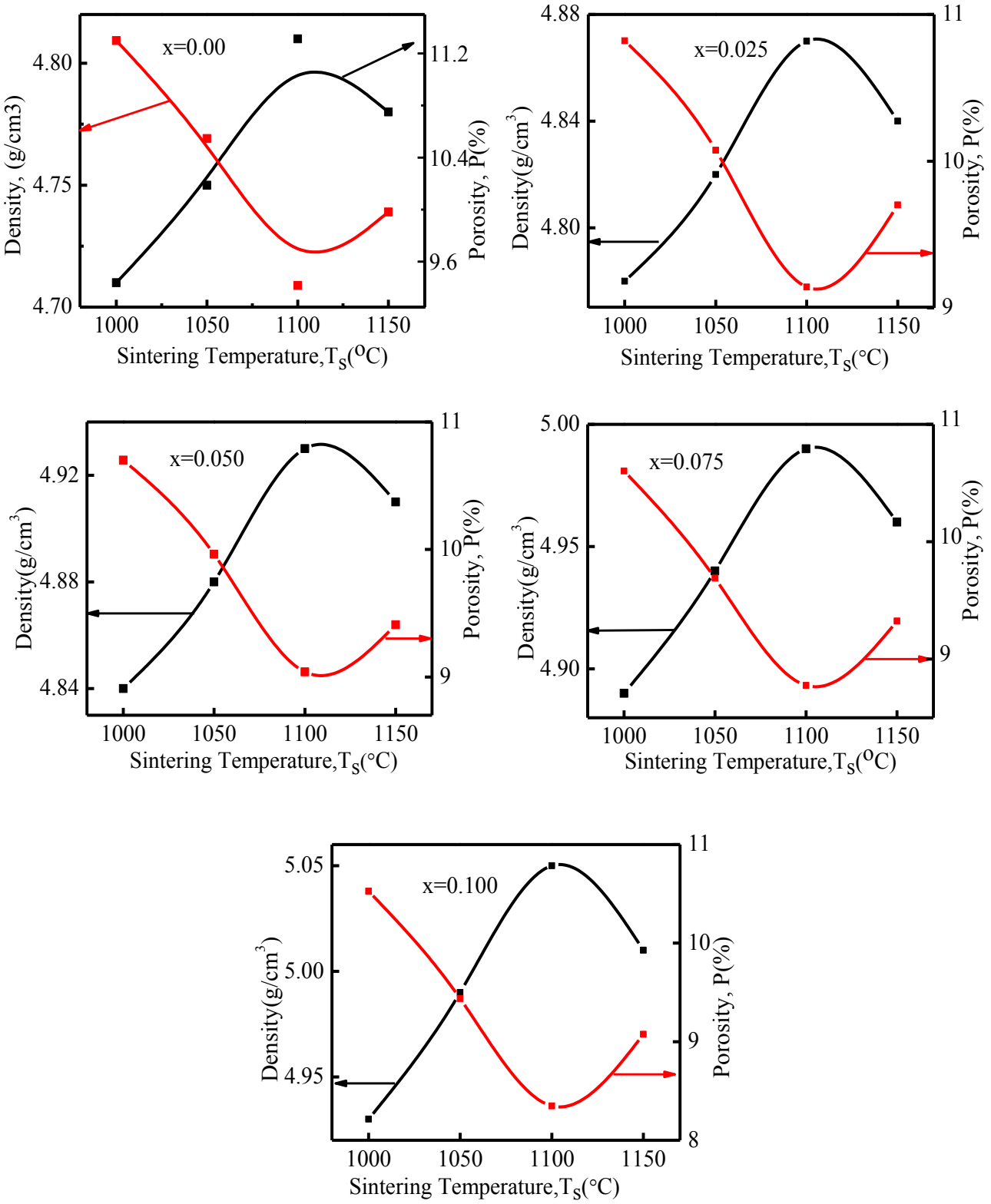

Fig.5.6 The variation of density and porosity with T_s for $Co_{0.4}Cu_{0.2}Zn_{0.4}Gd_xFe_{2-x}O_4$ at x=0.000, x=0.025, x=0.050, x=0.075 and x=0.100 in air.

The effect of T_s on ρ_B and P may be explained in the following ways-

The P of ferrite samples usually results from two sources, i.e. intragranular and intergranular, depending on whether pores remain within the grains or pores lie in the grain boundaries. Therefore, total P may be written as [8]

$$\text{Porosity: } P = P_{intra} + P_{inter}$$

i) During the sintering process, the thermal energy generates a force that drives the grain boundaries to grow over pores, thereby decreasing the pore volume and densifying the samples.

ii) When the grain growth rate is very high, pores are left behind the rapidly moving grain boundaries and are trapped within the grains. This intragranular P is practically impossible to eliminate, leading to poor magnetic properties [8]. The discontinuous growth of grain rises with temperature [8].

At higher T_s, the ρ_B decreases because the intragranular P increases resulting from discontinuous grain growth. Such a conclusion is in agreement with that previously reported in case of *Ni-Zn* ferrites [9].

5.4 Microstructures of $Co_{0.40}Cu_{0.20}Zn_{0.40}Gd_xFe_{2-x}O_4$

Structural and magnetic properties sensitively depend on the microstructure of ferrites. The average grain size of various $Co_{0.40}Cu_{0.20}Zn_{0.40}Gd_xFe_{2-x}O_4$ with the variation of sintering temperatures1000 and 1150 ^oC, are listed in Table 5.1. Grain size is an important parameter affecting the magnetic properties of ferrites. Grain growth is closely related to the grain boundary mobility. Recrystallization and grain growth involve the movement of grain boundaries. The grain growth, being a result of inter-particle mass transport, appears to be dominated by the diffusion mechanism, lattice and grain boundary diffusion. The behavior of grain growth reflects the

competition between the driving force for grain boundary movement and the retarding force exerted by pores [10]. When the driving force of the grain boundary in each grain is homogeneous, the sintered body attains a uniform grain size distribution. Abnormal grain growth occurs if this driving force is inhomogeneous. Moreover, the strength of the driving force depends upon the diffusivity of individual grains, sintering temperature and porosity. The sem of $Co_{0.40}Cu_{0.20}Zn_{0.40}Gd_xFe_{2-x}O_4$ sintered at 1000 to 1150 ºC are shown in Figs. 5.7 to 5.10 respectively. The average grain size (D) increases with increasing Gd content in the $Co_{0.40}Cu_{0.20}Zn_{0.40}Gd_xFe_{2-x}O_4$ up to x=0.050 then a decreasing trend is observed for x= 0.075 and 0.100. It may be considered that all Gd^{3+} ions enter into the spinel lattice during sintering and activate the lattice diffusion. The average grain size increases gradually with increase of Gd^{3+} may be due to the fact that melting point of Gd^{3+} (1585K) is less than that of Fe^{3+} (1808K) and the decrease in grain size beyond x=0.075 perhaps related to complicated chemistry of Gd^{3+} (higher concentration) with other materials. For x=0.075 and x=0.100 the formation of exaggerated grains of non-uniform size is seen to occur. The uniformity and the grain size and the average grain diameter can control properties such as the magnetic permeability. The average grain diameter (D) of the samples is determined by linear intercept technique [8].

It is also found that the sintering temperatures have influence on grain size for a particular composition. It is noticed that the average grain size of all samples increases with the sintering temperatures which is shown in Table 5.1. During the early stage of sintering temperature, the volume fraction of pores is large and the grain growth is inhibited. Once the porosity has decreased as the sintering temperature

increases many of the small pores disappear. The grains that grow consume their neighbor and become larger.

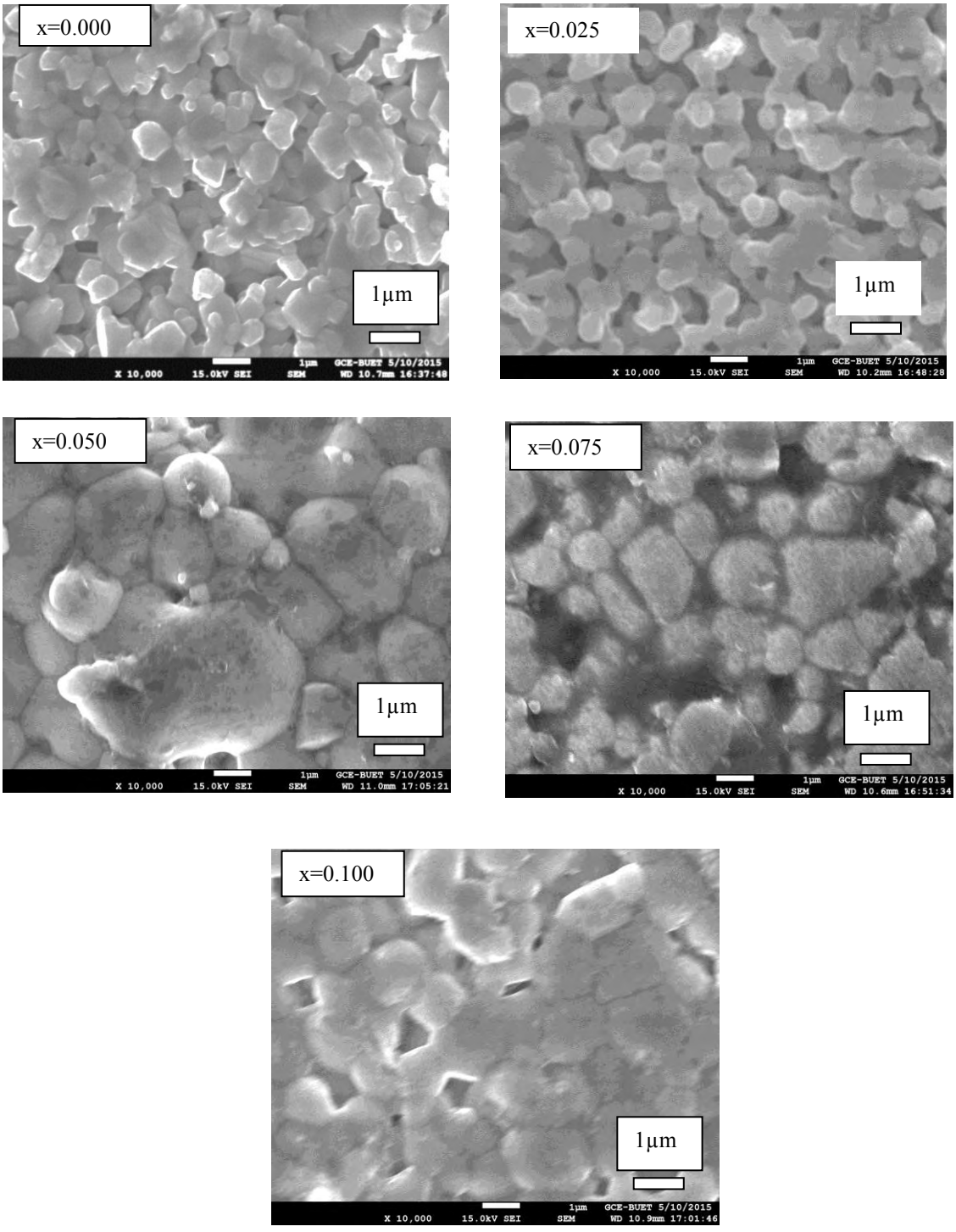

Fig.5.7 SEM for polycrystalline $Co_{0.40}Cu_{0.20}Zn_{0.40}Gd_xFe_{2-x}O_4$ for x=0.000, 0.025, 0.050, 0.075 and 0.100 at sintering temperature 1000 ºC.

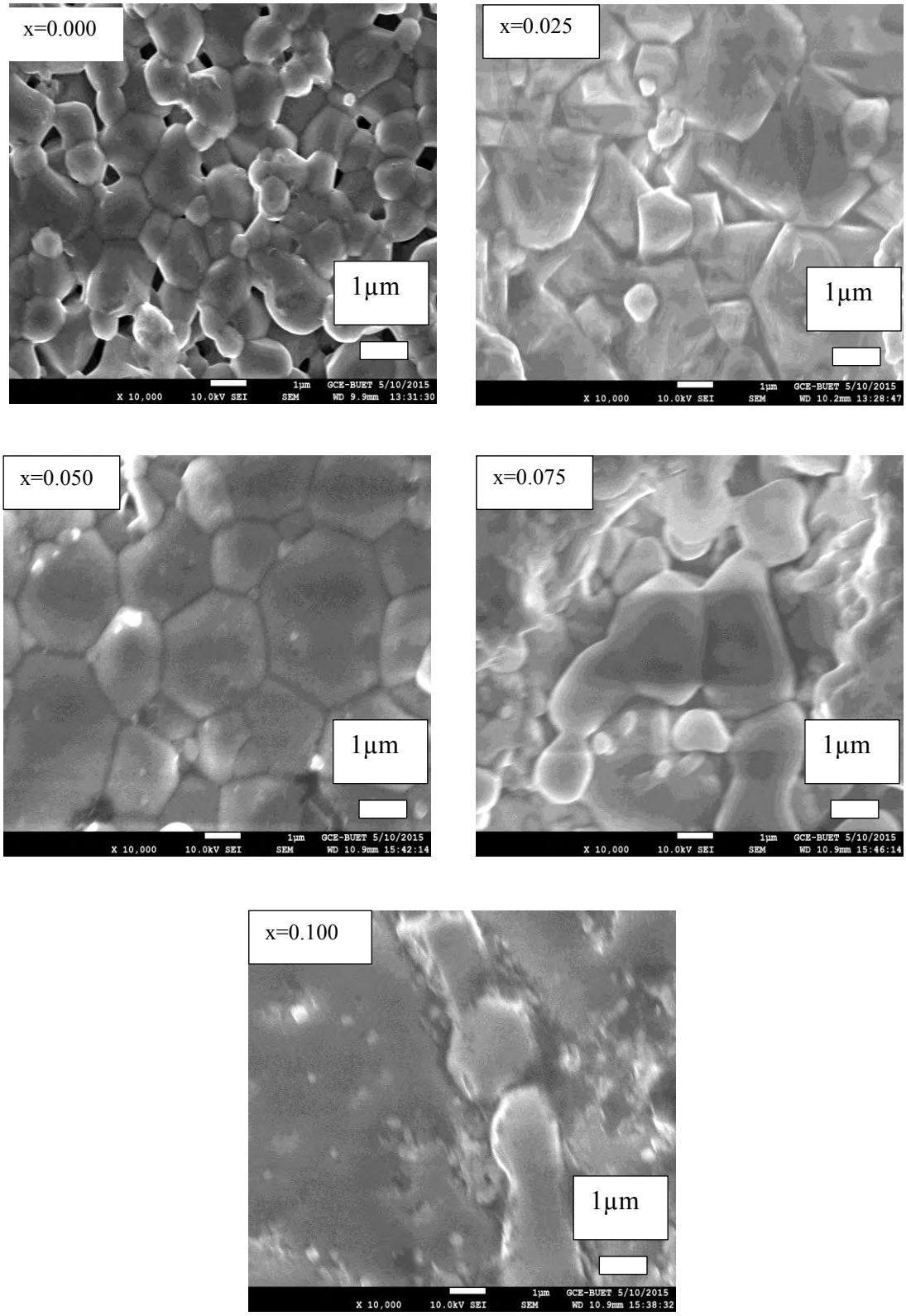

Fig.5.8 SEM for polycrystalline $Co_{0.40}Cu_{0.20}Zn_{0.40}Gd_xFe_{2-x}O_4$ for x=0.000, 0.025, 0.050, 0.075 and 0.100 at sintering temperature 1050 ºC.

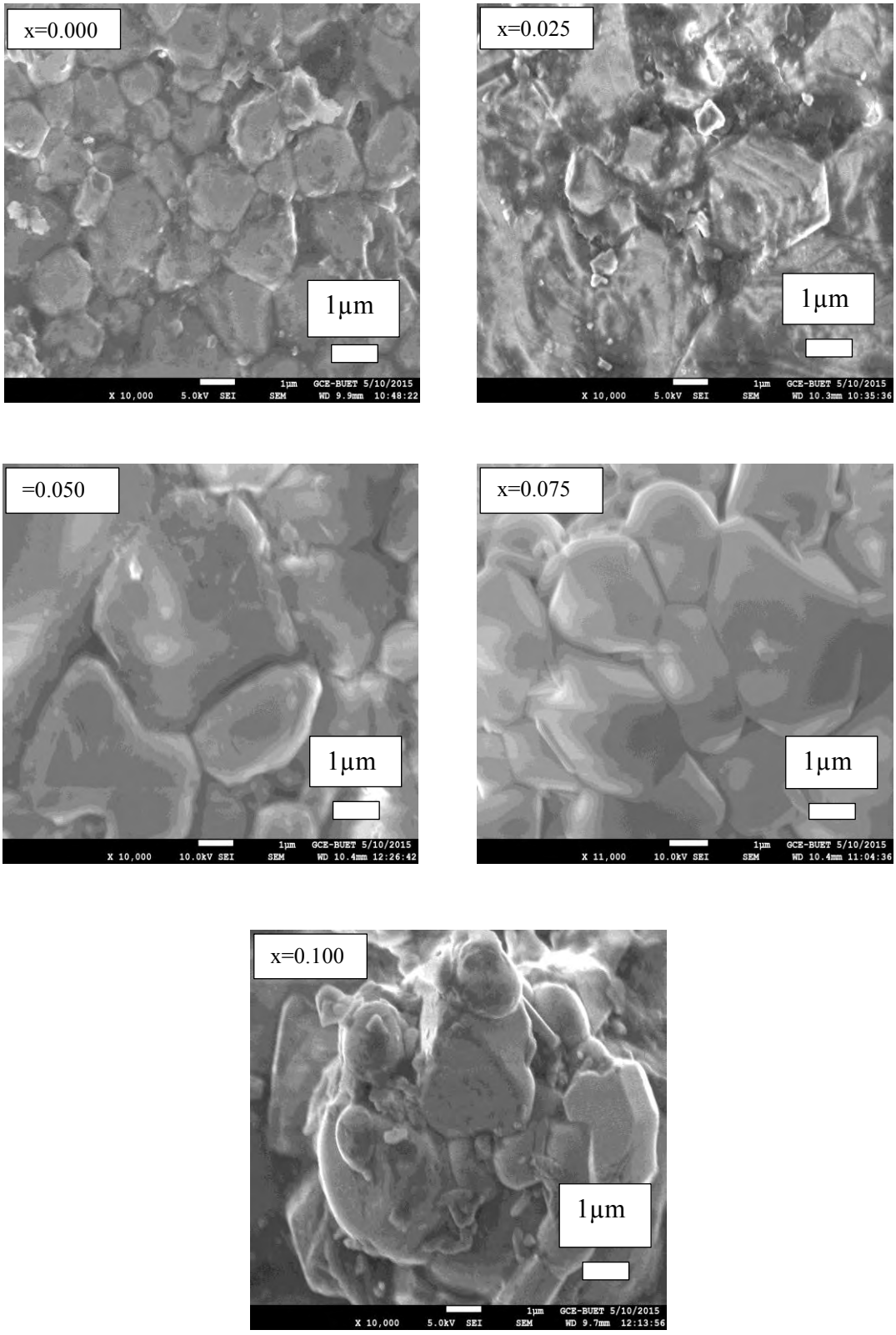

Fig.5.9 SEM for polycrystalline $Co_{0.40}Cu_{0.20}Zn_{0.40}Gd_xFe_{2-x}O_4$ for x=0.000, 0.025, 0.050, 0.075 and 0.100 at sintering temperature 1100 ºC.

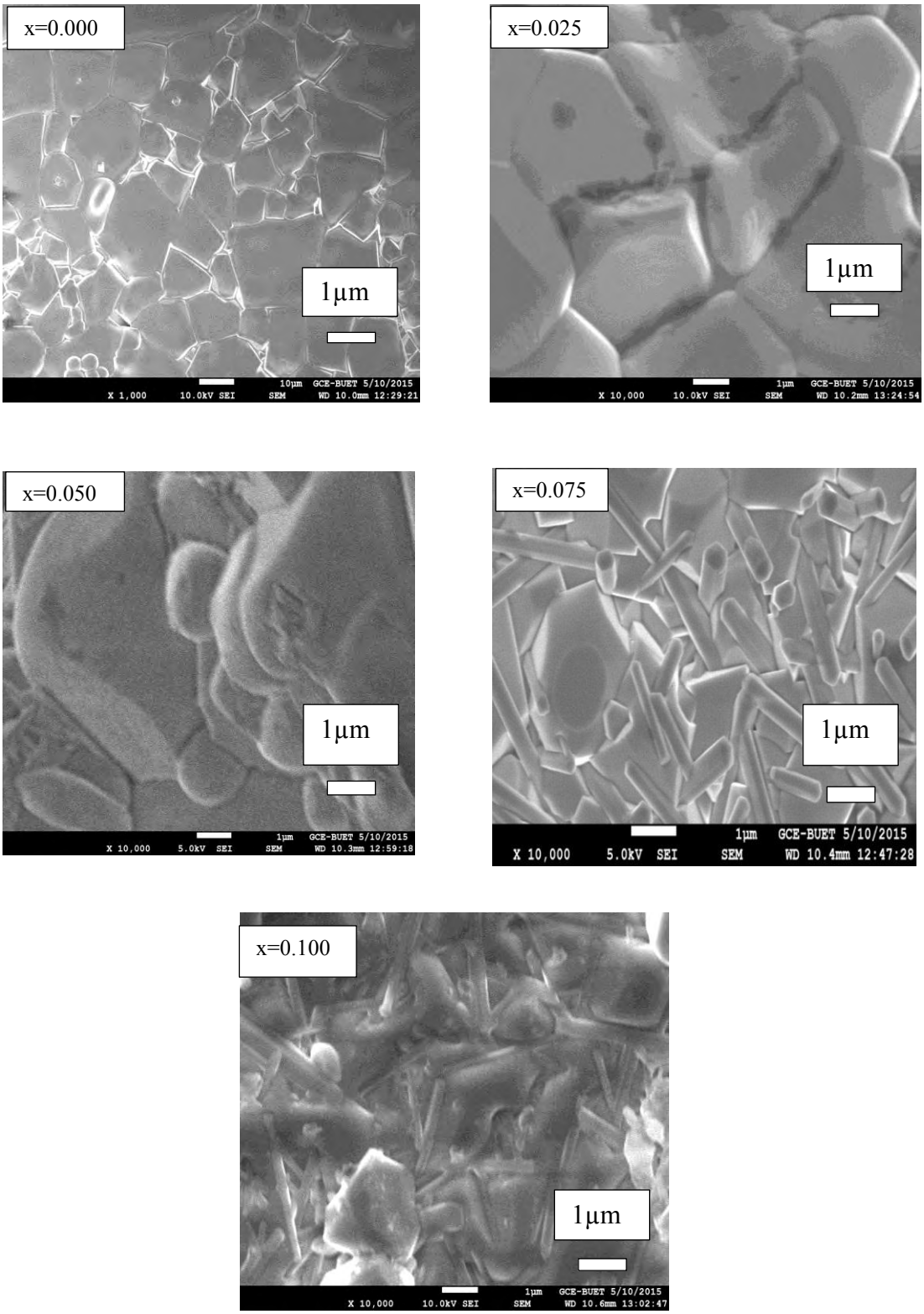

Fig.5.10 SEM for polycrystalline $Co_{0.40}Cu_{0.20}Zn_{0.40}Gd_xFe_{2-x}O_4$ for x=0.000, 0.025, 0.050, 0.075 and 0.100 at sintering temperature 1150 ºC.

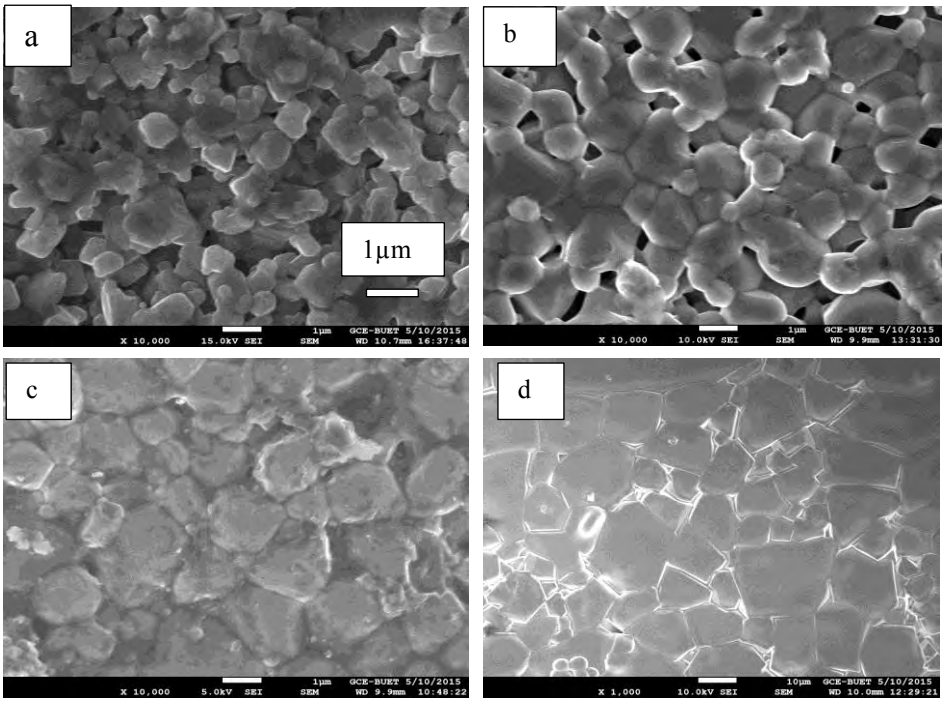

Fig.5.11 SEM for polycrystalline $Co_{0.40}Cu_{0.20}Zn_{0.40}Gd_xFe_{2-x}O_4$ for (a) T_s=1000, (b) 1050, (c) 1100 and (d) 1150 ºC for x=0.000.

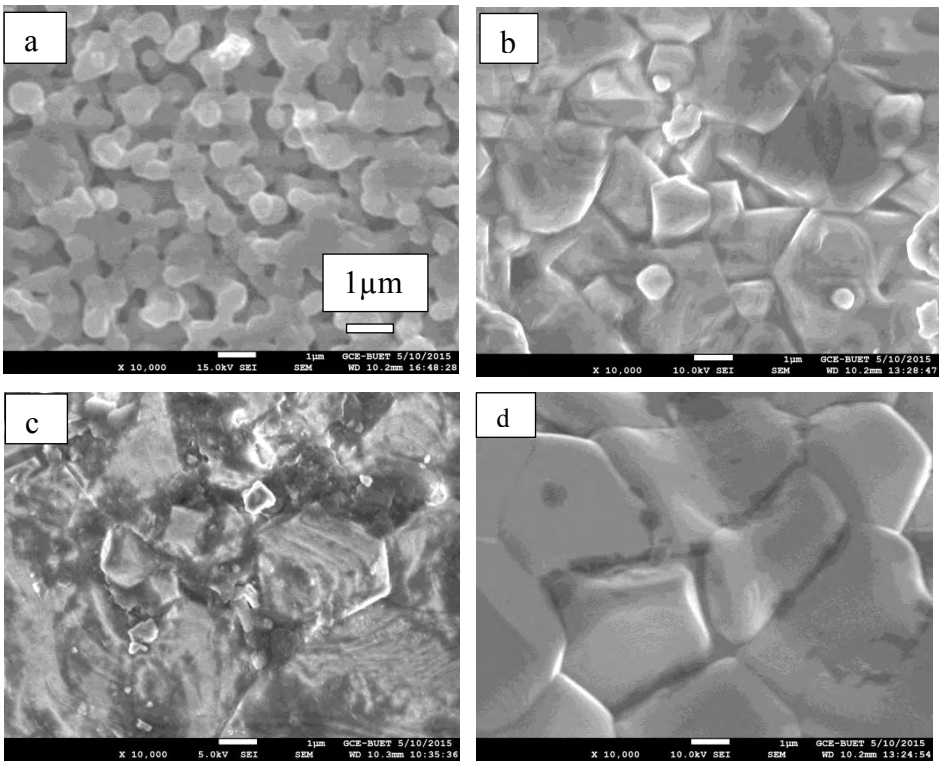

Fig.5.12 SEM for polycrystalline $Co_{0.40}Cu_{0.20}Zn_{0.40}Gd_xFe_{2-x}O_4$ for (a) T_s=1000, (b) 1050, (c) 1100 and (d) 1150 ºC for x=0.025.

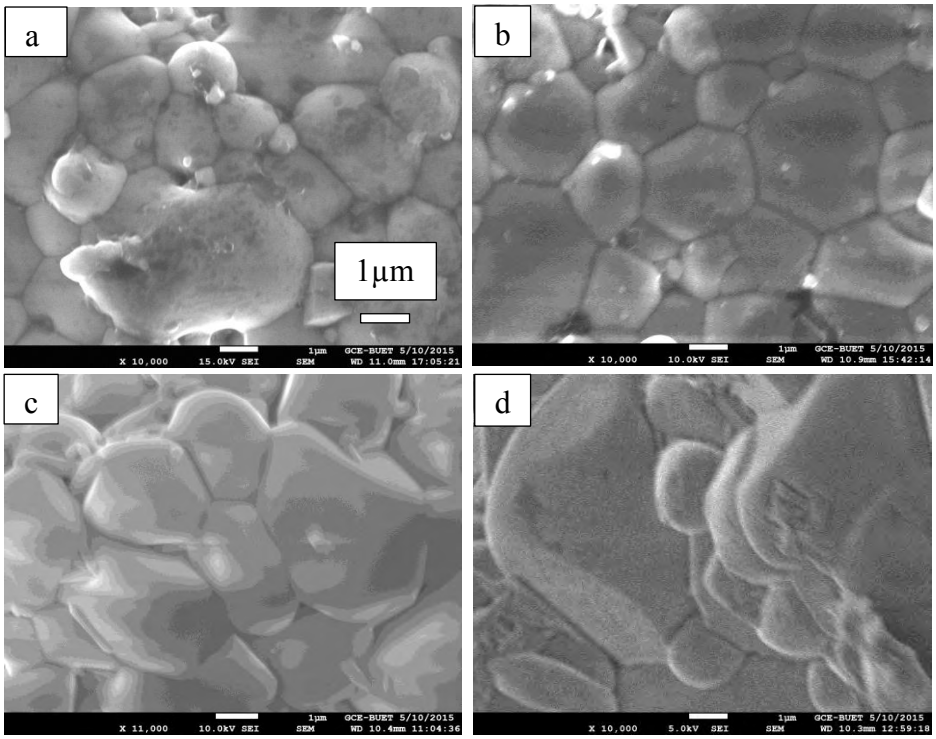

Fig.5.13 SEM for polycrystalline $Co_{0.40}Cu_{0.20}Zn_{0.40}Gd_xFe_{2-x}O_4$ for (a) T_s=1000, (b) 1050, (c) 1100 and (d) 1150 ºC for x=0.050.

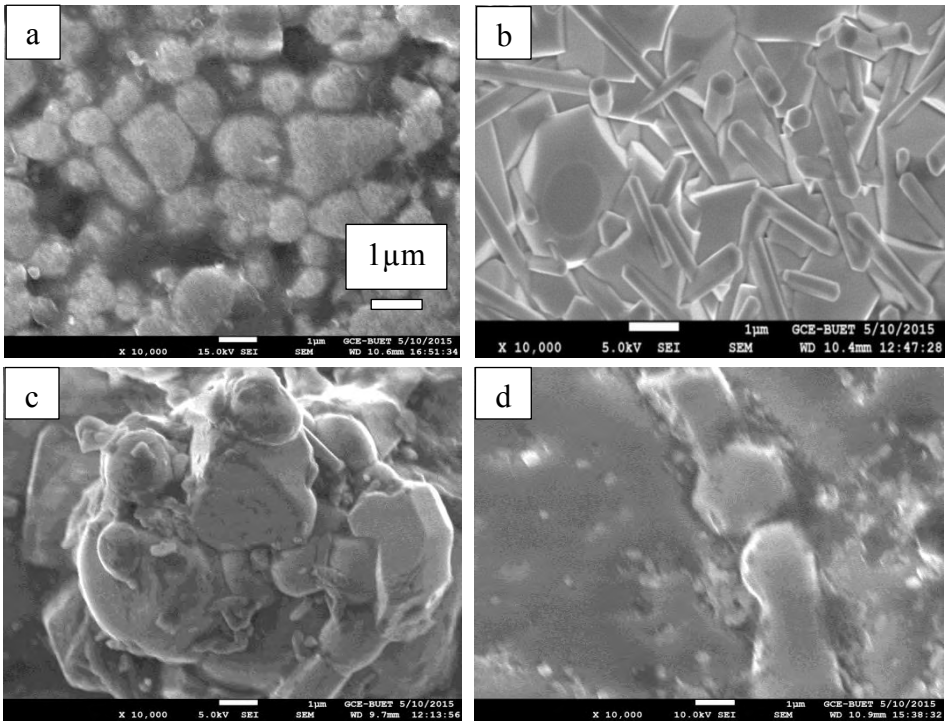

Fig.5.14 SEM for polycrystalline $Co_{0.40}Cu_{0.20}Zn_{0.40}Gd_xFe_{2-x}O_4$ for(a) T_s=1000, (b) 1050, (c) 1100 and (d) 1150 ºC for x=0.075.

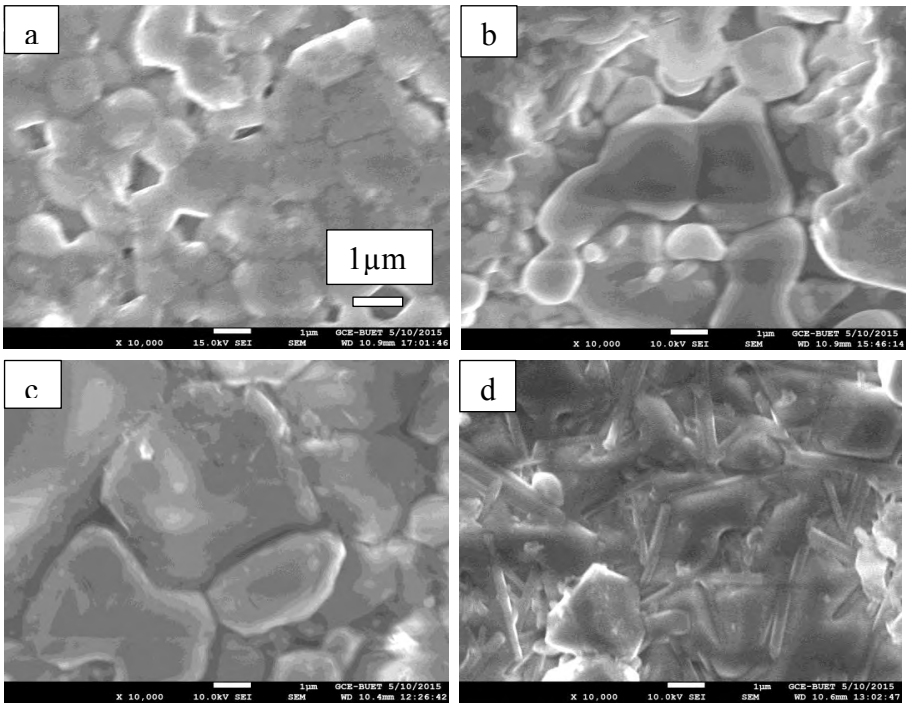

Fig.5.15. SEM for polycrystalline $Co_{0.40}Cu_{0.20}Zn_{0.40}Gd_xFe_{2-x}O_4$ for (a) T_s=1000,(b) 1050, (c)1100 and(d)1150 ºC for x=0.100.

5.5 Frequency dependence of complex permeability

The complex initial permeability spectra for $Co_{0.40}Cu_{0.20}Zn_{0.40}Gd_xFe_{2-x}O_4$ compositions sintered at various sintering temperatures as a function of frequency are shown in Fig5.16, 5.17.and 5.18. The complex initial permeability is given by $\mu_i^* = \mu_i^{/} - i\mu_i^{//}$, where $\mu_i^{/}$ and $\mu_i^{//}$ are the real and imaginary parts of initial

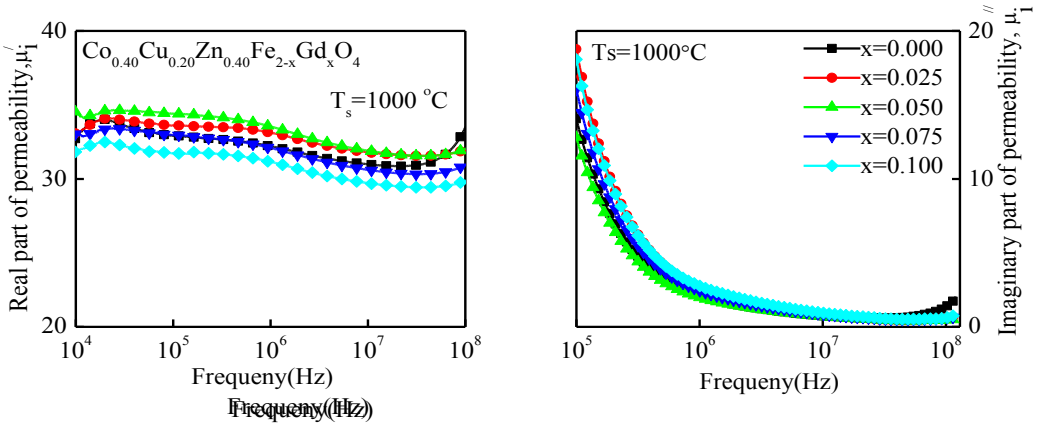

Fig.5.16 The variation of $\mu_i^{/}$ and $\mu_i^{//}$ spectra for $Co_{0.40}Cu_{0.20}Zn_{0.40}Gd_xFe_{2-x}O_4$ sintered at T_s=1000 ºC.

permeability respectively. The real permeability $\mu_i^{/}$ describes the stored energy expressing the component of magnetic induction B in phase with the alternating magnetic field H. The imaginary permeability $\mu_i^{//}$ describes the dissipation of energy expressing the component of B at 90° out of phase with the alternating magnetic field. It is found that the real ($\mu_i^{/}$) and imaginary ($\mu_i^{//}$) permeability increase with increase in Gd^{3+} substitution up to x=0.050 in $Co_{0.40}Cu_{0.20}Zn_{0.40}Gd_xFe_{2-x}O_4$ because of increase in density and grain size with Gd^{3+} content. Beyond this value of x, permeability decreases with increasing Gd^{3+}content due to non collinear spin arrangements [11]. The $\mu_i^{/}$ values increase with the increase of sintering temperature up to 1100 °C and above 1100 °C a decreasing trend is observed.

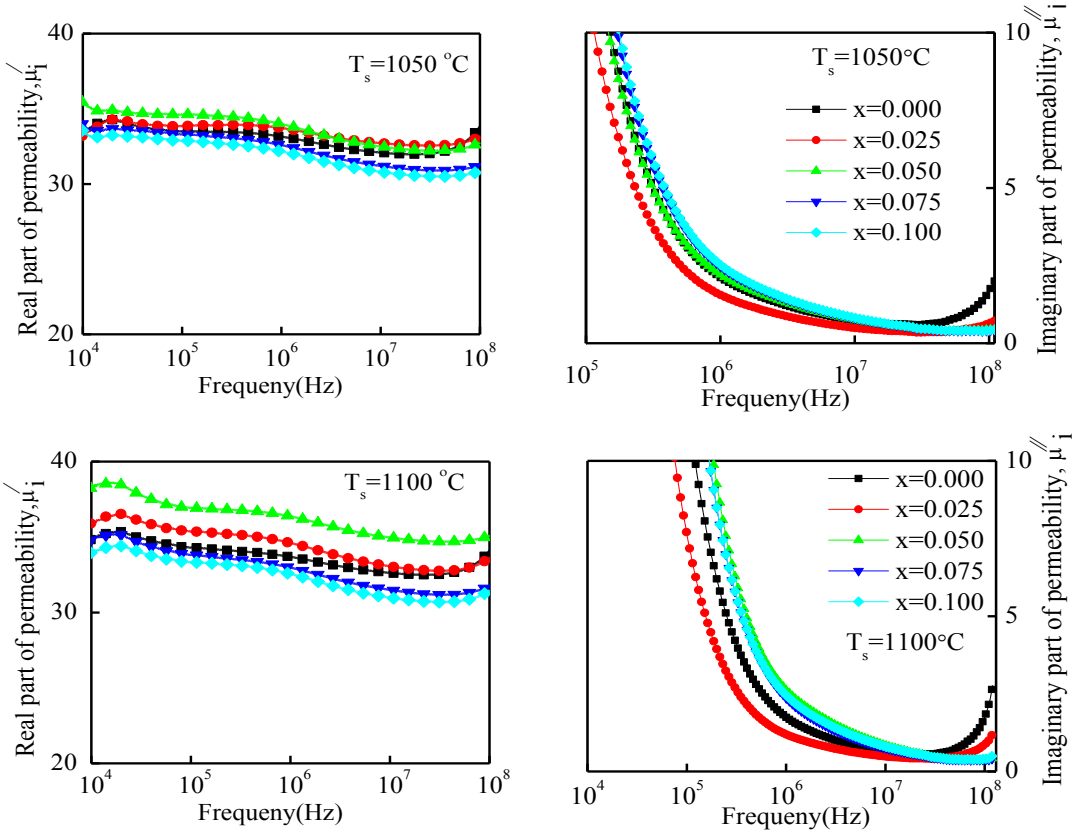

Fig.5.17 The variation of $\mu_i^{/}$ and $\mu_i^{//}$ spectra for $Co_{0.40}Cu_{0.20}Zn_{0.40}Gd_xFe_{2-x}O_4$ sintered at T_s=1050, 1100 °C.

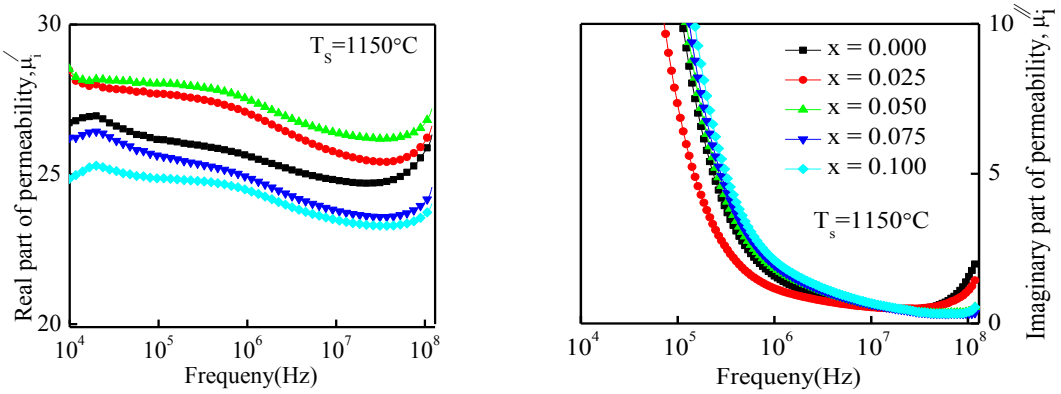

Fig.5.18 The variation of μ_i' and μ_i'' spectra for $Co_{0.40}Cu_{0.20}Zn_{0.40}Gd_xFe_{2-x}O_4$ sintered at T_s=1150 °C.

The increasing value of μ_i' with the increase of sintering temperature after doping Gd^{3+} content up to 1100 °C is due to the lower porosity for the samples sintered at higher temperature. The porosity causes hindrance to the domain wall motion. As the sintering temperature increases, pores and voids are reduced with increasing sintering temperature. The values of μ_i' decreases above 1100 °C because the sample heated higher sintering temperatures (above optimum) contain increasing numbers of pores with in the grains with results to a decrease in permeability. Similar trend was obtained by Guillard [12] in Mn-Zn ferrites.

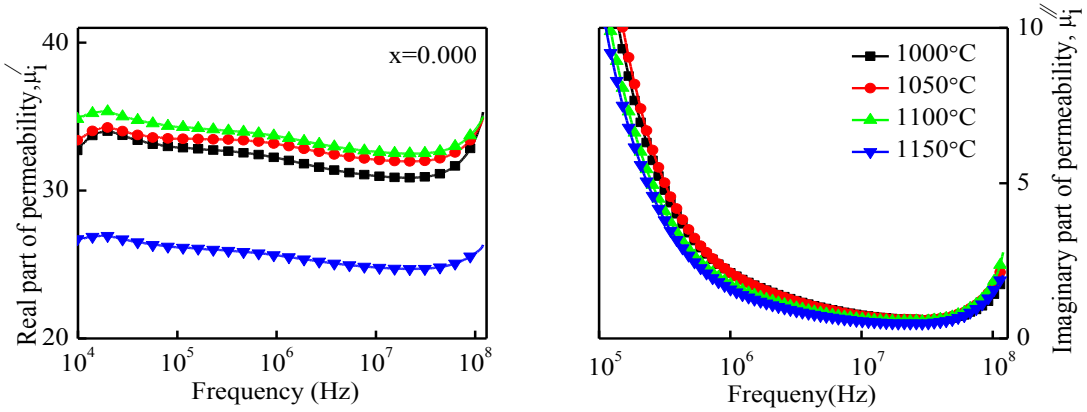

Fig.5.19 The variation of μ_i' and μ_i'' spectra for $Co_{0.40}Cu_{0.20}Zn_{0.40}Gd_xFe_{2-x}O_4$ various sintering temperature at x=0.000.

The initial permeability of ferrite material depends on many factors like reversible domain wall displacement, domain wall bulging as well as microstructural features viz., average grain size, intra-granular porosity, etc. [13]. In a demagnetized magnetic material, there are a number of Weiss domains with Block walls separating two domains. These walls are bound to the equilibrium positions. The whole permeability phenomena can be explained as below .The permeability of polycrystalline ferrite is related to two different magnetizing mechanisms: spin rotation and domain wall motion [14, 50, 15-16],

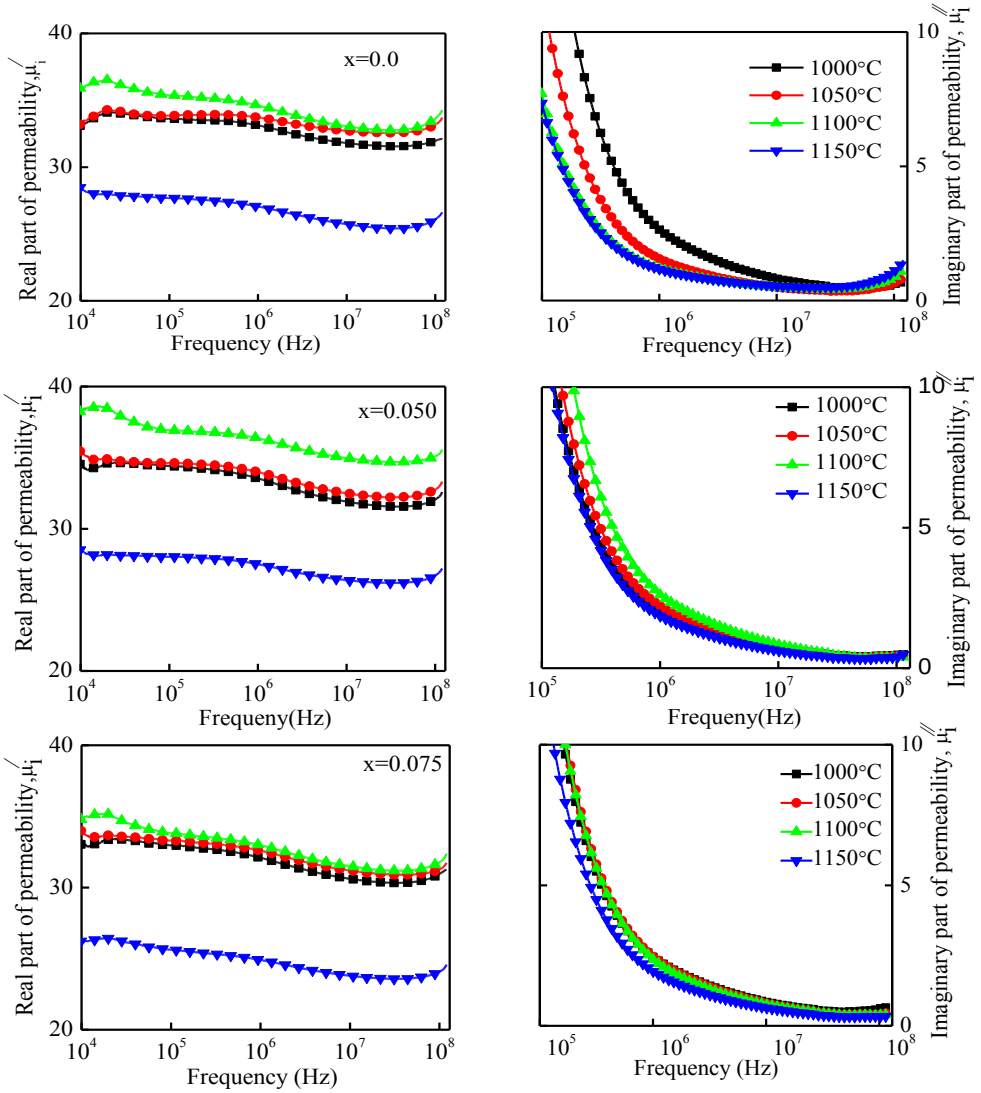

Fig.5.20 The variation of $\mu_i^{/}$ and $\mu_i^{//}$ spectra for $Co_{0.40}Cu_{0.20}Zn_{0.40}Gd_xFe_{2-x}O_4$ various sintering temperature at x= 0.025, 0.050.and 0.075.

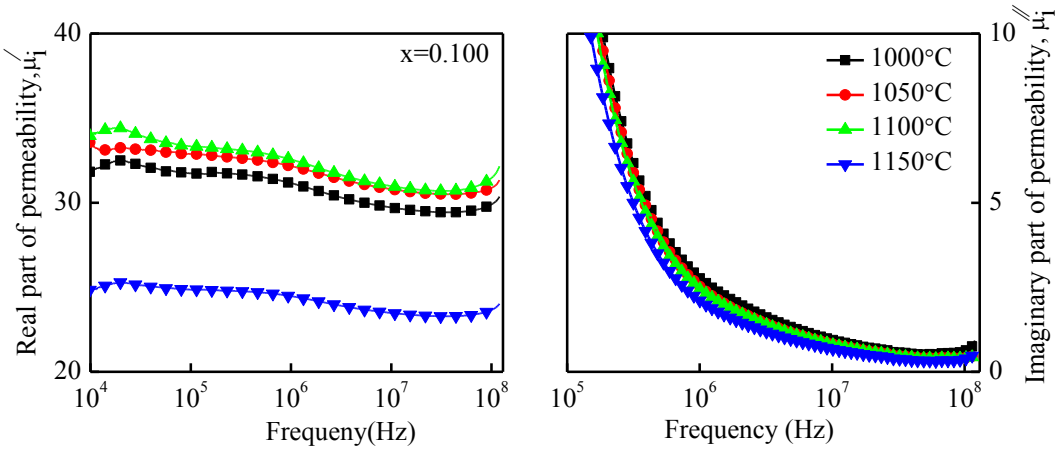

Fig.5.21 The variation of $\mu_i^{/}$ and $\mu_i^{//}$ spectra for $Co_{0.40}Cu_{0.20}Zn_{0.40}Gd_xFe_{2-x}O_4$ various sintering temperature at x= 0.100.

Which can be described as follows: $\mu_i = 1 + \chi_w + \chi_{spin}$ where χ_w is the domain wall susceptibility; χ_{spin} is intrinsic rotational susceptibility. χ_w and χ_{spin} may be written as : $\chi_w = 3\pi M_s^2 D/4\gamma$ and $\chi_{spin} = 2\pi M_s^2/K$ with M_s saturation magnetization, K the total anisotropy, D the average grain diameter, and γ the domain wall energy. The $\mu_i^{/}$ is a function of grain size. As the grain size increases with Gd content, the $\mu_i^{/}$ also increases. The domain wall motions are affected by grain size and enhance with the increase of grain size thus the $\mu_i^{/}$ increases. Therefore in the present case, variation of the initial permeability is strongly influenced by its grain size and porosity. The magnetic spectra reflect the properties of inductors [17].

Moreover, the magnetic properties of soft ferrite are strongly influenced by its composition, additives and microstructures of the material. Among all these factors, the microstructures have great influence on magnetic properties. It is generally believed that larger the grain sizes, the higher the saturation magnetization and initial permeability. In microstructure studies of the present ferrite system it is also observed that average grain size increases with Gd^{3+} content up to the same optimum, x=0.050

and sudden decrease is observed beyond it. Therefore in the present case, variation of the initial permeability is strongly influenced by its grain size and *DC* magnetization property. In ferrites, two resonance peaks are normally observed: one at lower frequency (10-100MHz) which is due to the domain wall oscillations [18, 19] and the other at higher frequencies (~1GHz) due to Larmour precession of electron spins [20]. In the present case, the resonance frequency of domain wall oscillations is not found for this composition.

The magnetization caused by domain wall movement requires less energy than that required by domain rotation. As the number of walls increases with the grain sizes, the contribution of wall movement to magnetization is increased. In our experiment, the grain size is enriched by more content of Gd^{3+} in the samples up to a certain level. Similar result reported for others materials by Hossain *et. al* [21].

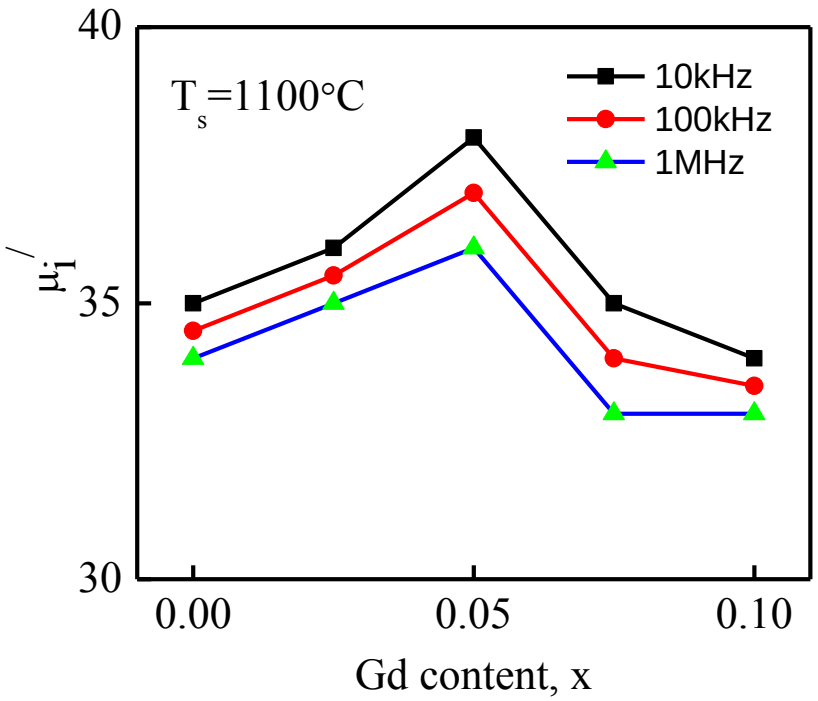

Fig.5.22 Variation of real part of initial permeability of various $Co_{0.40}Cu_{0.20}Zn_{0.40}Gd_xFe_{2-x}O_4$ at different frequencies sintered at 1100 °C with Gd content.

It is clearly noticeable that the maximum initial permeability of $Co_{0.40}Cu_{0.20}Zn_{0.40}Gd_xFe_{2-x}O_4$ is obtained at the 1100 °C, so that at higher sintering temperature an increasing trend is observed. Fig.5.21 shows the variation of permeability at different frequencies with Gd^{3+} content in $Co_{0.40}Cu_{0.20}Zn_{0.40}Gd_xFe_{2-x}O_4$. It shows a decreasing trend in permeability with the increase of Gd^{3+}content. This is because at higher frequencies insoluble nonmagnetic impurities between the grains and intragranular pores act as pinning points and increasingly hinder the motion of spin and domain walls thereby decreasing their contribution to permeability and also increasing the loss [22].

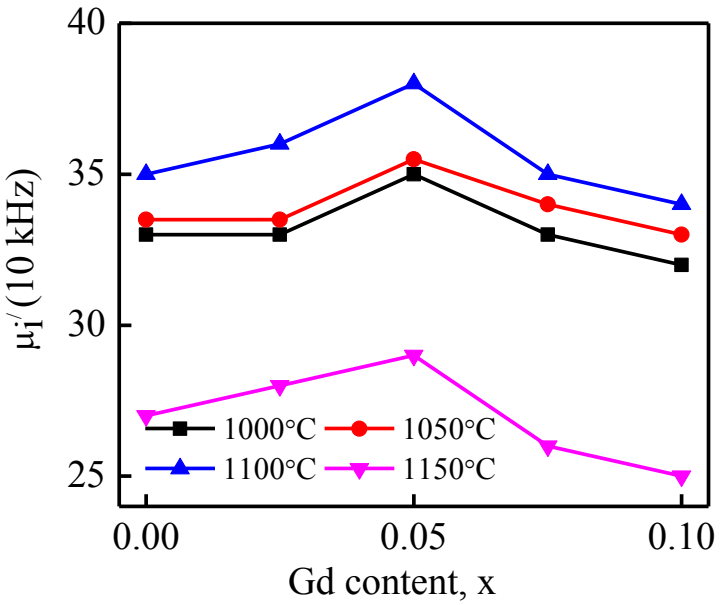

Fig.5.23 Variation of real part of initial permeability at 10 kHz of various $Co_{0.40}Cu_{0.20}Zn_{0.40}Gd_xFe_{2-x}$ at different sintering temperature with Gd content.

Fig.5.23 shows the variation of permeability at 10 kHz with Gd^{3+} content for $Co_{0.40}Cu_{0.20}Zn_{0.40}Gd_xFe_{2-x}O_4$ ferrites sintered at 1000, 1050, 1100 and 1150 °C in air. It is clear from the fig.5.30 that permeability increases as the sintering temperature increases from 1000 to 1100 °C. The higher sintering temperatures result in the increase in the density of the specimen which facilitates the movement of the spins as

the numbers of pores which impede the wall motion are reduced. Increase in the sintering temperature also results in a decrease in the internal stresses, which reduce the hindrance to the movement of the domain walls resulting thereby in the increased value of $\mu_i^{/}$ [8].

5.6 Relative quality factor

The relative quality factor (*Q-factor*) versus frequency plots of all the samples sintered at 1000, 1050, 1100, and 1150 °C are shown in Fig. 5.24. The relative quality factors, Q ($=\mu_i^{/}/\tan\delta$) were calculated by the ratio of the real part of initial permeability and magnetic loss tangent measured on the coil wound toroidal samples. The variation of the relative quality factor with frequency showed almost similar trend for all the samples.

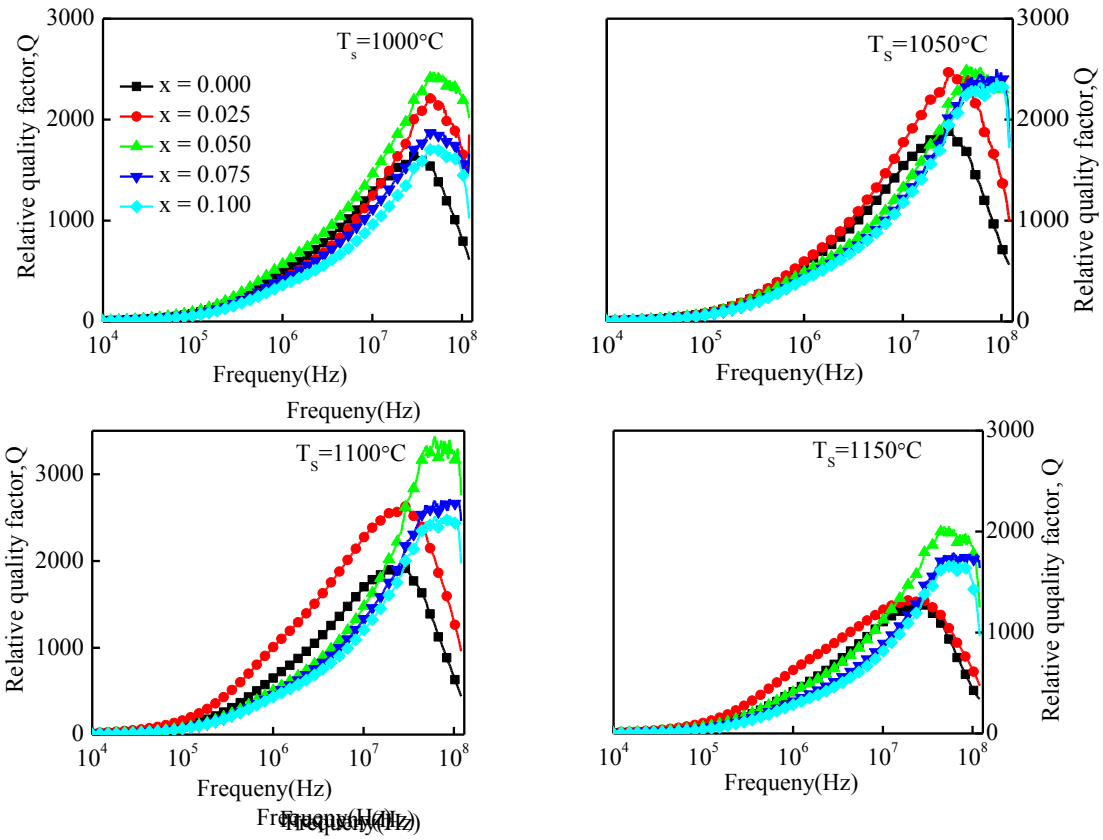

Fig.5.24 The variations of Relative Quality factors (*Q*-factor) with frequency for $Co_{0.40}Cu_{0.20}Zn_{0.40}Gd_xFe_{2-x}O_4$ sintered at 1000 °C, 1050 °C, 1100 °C, and 1150 °C in air.

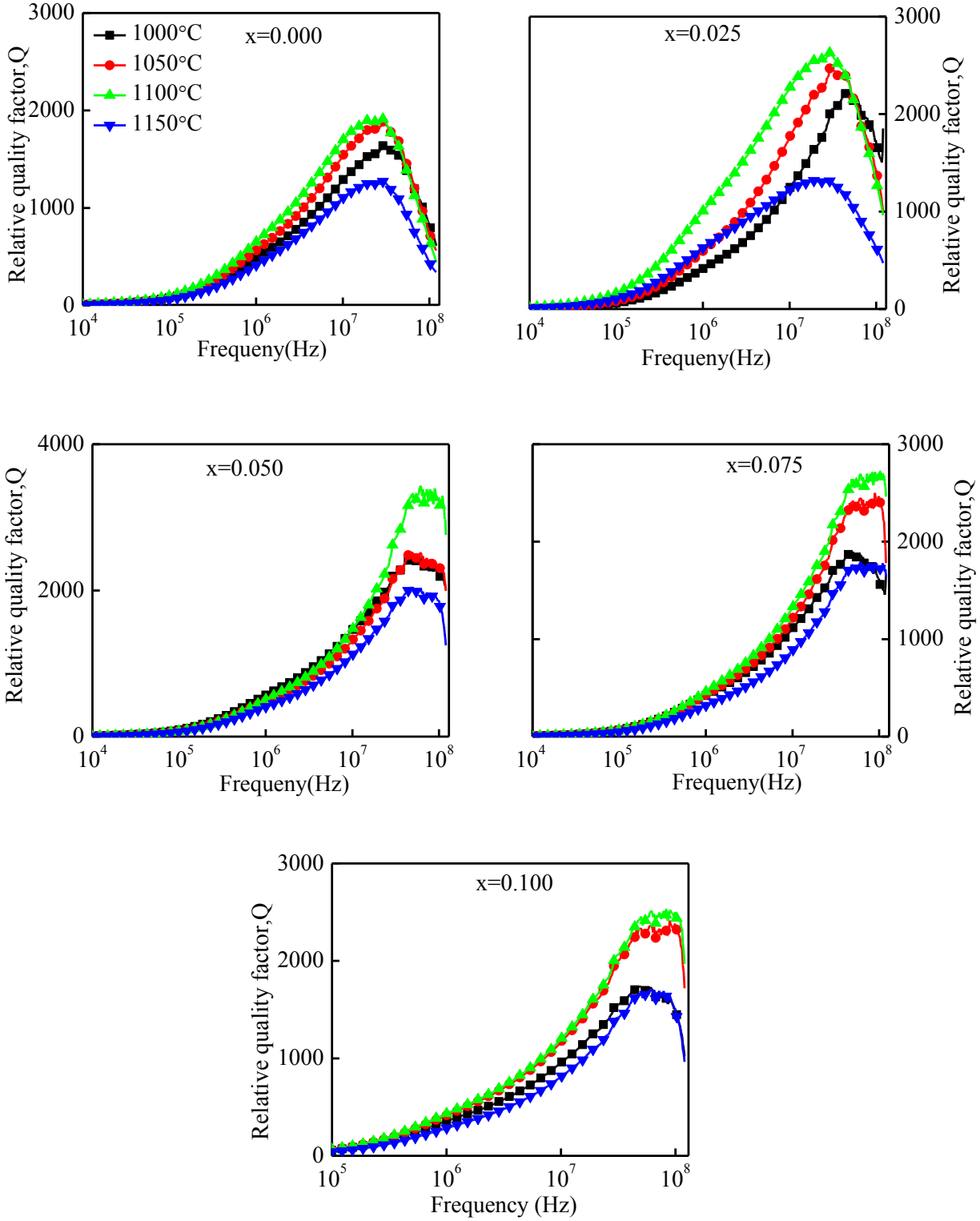

Fig.5.25 The variations of Relative Quality factors (Q-factor) with frequency for $Co_{0.40}Cu_{0.20}Zn_{0.40}Gd_xFe_{2-x}O_4$ at x=0.000, 0.025, 0.075 and 0.100 in air.

Calculated *Q-factor*s for various $Co_{0.40}Cu_{0.20}Zn_{0.40}Gd_xFe_{2-x}O_4$ sintered at various temperatures are listed in Table 5.1. It can be seen that the value of *Q*-factor increases with an increase of frequency. It is also observed from the Fig 5.24 that the maximum value of *Q-factor, Q_{max}* increases with increasing Gd contents from x=0.000 to x=0.050, then it decreases. By increasing Gd content, the RQF increases and the peak associated with the RQF shifting to higher frequencies. Similar variation is observed for $Co_{0.40}Cu_{0.20}Zn_{0.40}Gd_xFe_{2-x}O_4$ sintered at other temperatures as well.

It shows a similar trend of $\mu_i^{/}$ of the present system as it is proportional to the *Q*-factor from the relation: $Q = \mu_i^{/} / tan\delta$. Among all the studied samples, highest value of *Q*-factor (= 2714) is observed for $Co_{0.40}Cu_{0.20}Zn_{0.40}Gd_xFe_{2-x}O_4$ sintered at 1100 °C, similar to $\mu_i^{/}$. Above 1100 °C, *Q-factor* is found to decrease because at higher sintering temperature, abnormal grain growth occurs which creates trapped pores inside the grain. This increasing amount of pores influences the loss factor and turns into higher value which results a lower value of *Q*-factor.

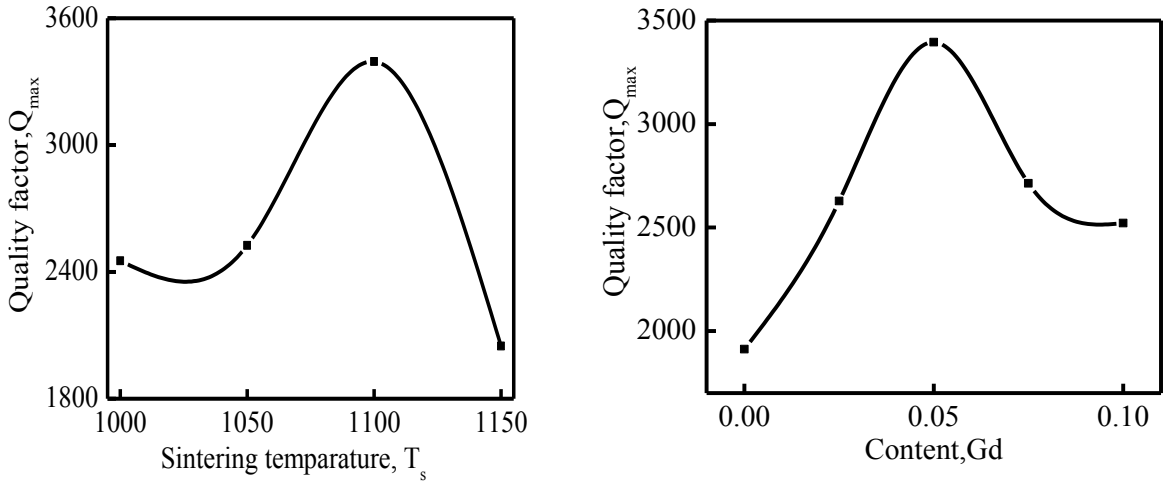

Fig.5.26 The variations Q_{max} of $Co_{0.40}Cu_{0.20}Zn_{0.40}Gd_xFe_{2-x}O_4$ with sintering temperature and Gd content.

5.7 Frequency dependence of loss factor

The ratio of $\mu_i^{/}$ and $\mu_i^{//}$ representing the losses in the material are a measure of the inefficiency of the magnetic system. Obviously this parameter should be as low as possible.

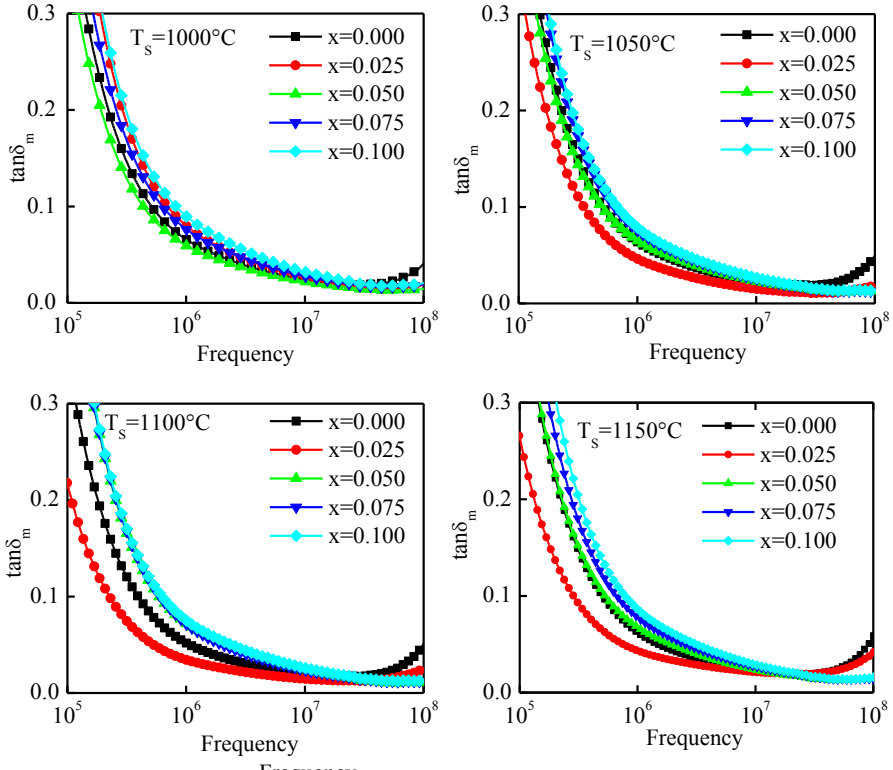

Fig.5.27 The variations of Loss factor with frequency for $Co_{0.40}Cu_{0.20}Zn_{0.40}Gd_xFe_{2-x}O_4$.

The magnetic losses, which cause the phase shift, can be split up into three components: hysteresis losses, eddy current losses and residual losses. This gives the formula $\tan\delta_m = \tan\delta_h + \tan\delta_e + \tan\delta_r$. The variation of loss factor, $\tan\delta_m$ ($=\mu_i^{//}/\mu_i^{/}$) with frequency for all samples has been studied. Fig.5.27 shows the variations of loss factors with frequency for $Co_{0.40}Cu_{0.20}Zn_{0.40}Gd_xFe_{2-x}O_4$ sintered at 1000, 1050, 1100 and 1150 °C respectively. It is clear from these figures that the $\tan\delta_m$ decreases with increasing Gd^{3+} content. The lag of dipole motion with respect to the applied magnetic field is responsible for magnetic loss and this is accredited to lattice imperfections [54].

5.8 DC magnetization $Co_{0.40}Cu_{0.20}Zn_{0.40}Gd_xFe_{2-x}O_4$

The magnetization (M) as a function of applied magnetic field (H) for various $Co_{0.40}Cu_{0.20}Zn_{0.40}Gd_xFe_{2-x}O_4$ (with x = 0.000-0.100 at a step of 0.025) measured at room temperature (300K) are shown in Fig.5.28. The magnetization of all samples increases linearly with increasing the applied magnetic field up to 0.1T. Beyond this applied field magnetization increases slowly and then saturation occurs. It indicates that all the samples are in ferromagnetic state. The saturation magnetization, $M_{S,}$ for all sample are determined by the extrapolation of magnetization curve to $\mu_{\circ}H = 0$.

It is seen that the variation of M_S for various $Co_{0.40}Cu_{0.20}Zn_{0.40}Gd_xFe_{2-x}O_4$ slightly increases up to x = 0.050 and then it decreases with increasing Gd-content. Using these values of M_S, the number of Bohr magneton, n_B, has been calculated by using the relation, $n_B = \frac{MM_s}{N_A\mu_B}$ 3],

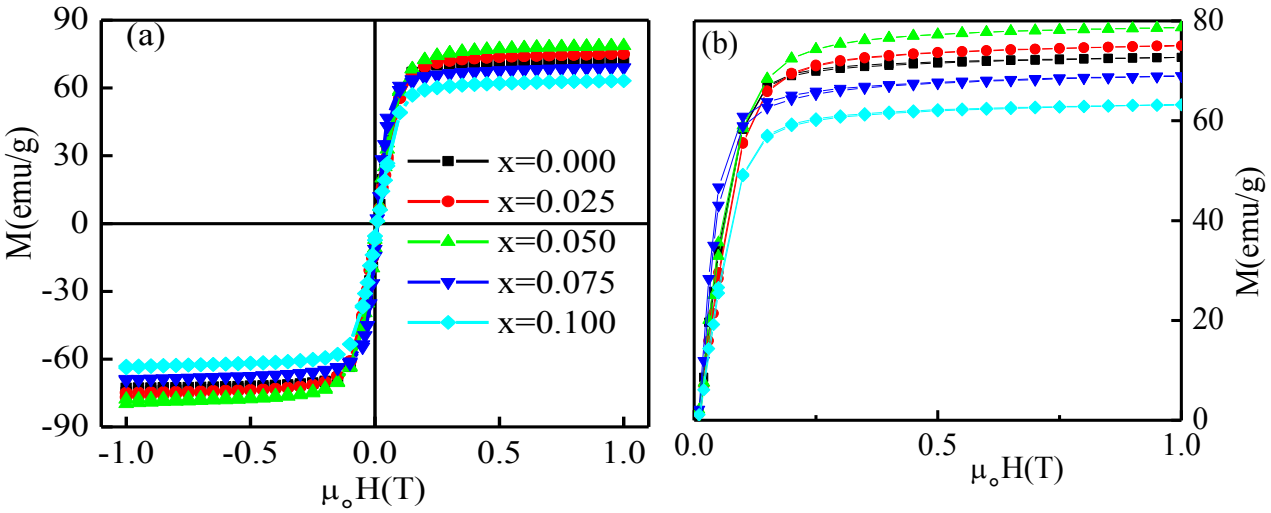

Fig.5.28 The variation of magnetization with applied magnetic field for various $Co_{0.40}Cu_{0.20}Zn_{0.40}Gd_xFe_{2-x}O_4$ sintered at 1100 °C.

Where M is the molecular weight, N_A is the Avogadro"s number and μ_B is the Bohr magneton. This formula is used to extract the microscopic magnetic information from

the bulk magnetization measurements. The variation of n_B with Gd-content is shown in Figure 5.29. It is found that the value of n_B follows the similar trend that of M_S with Gd content because both n_B and M_S are correlated to each other.

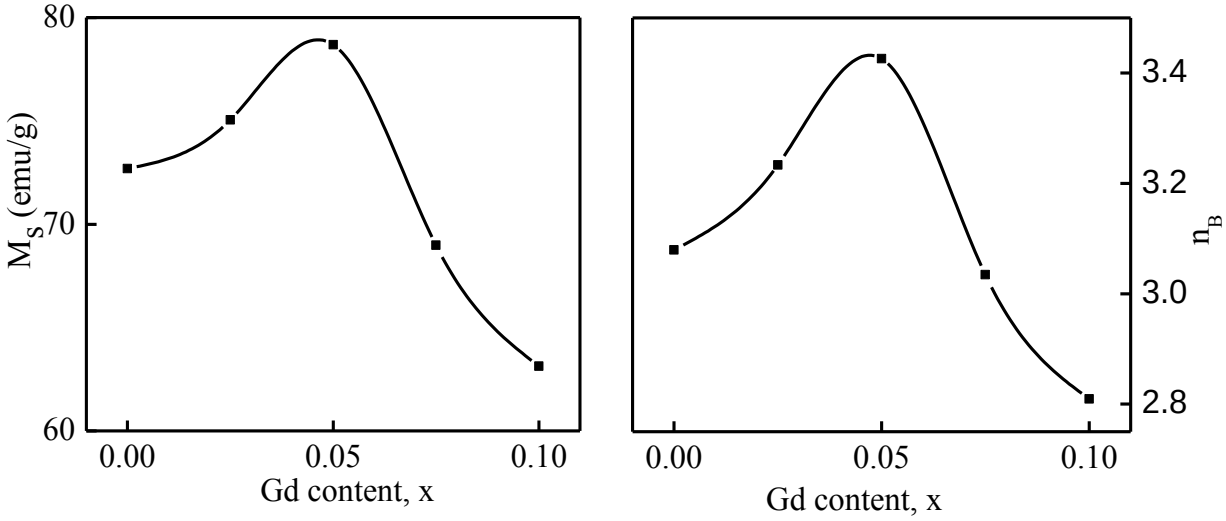

Fig.5.29 The variation of M_s and n_B with *Gd* content, x, in $Co_{0.40}Cu_{0.20}Zn_{0.40}Gd_xFe_{2-x}O_4$ sintered at 1100 °C in air.

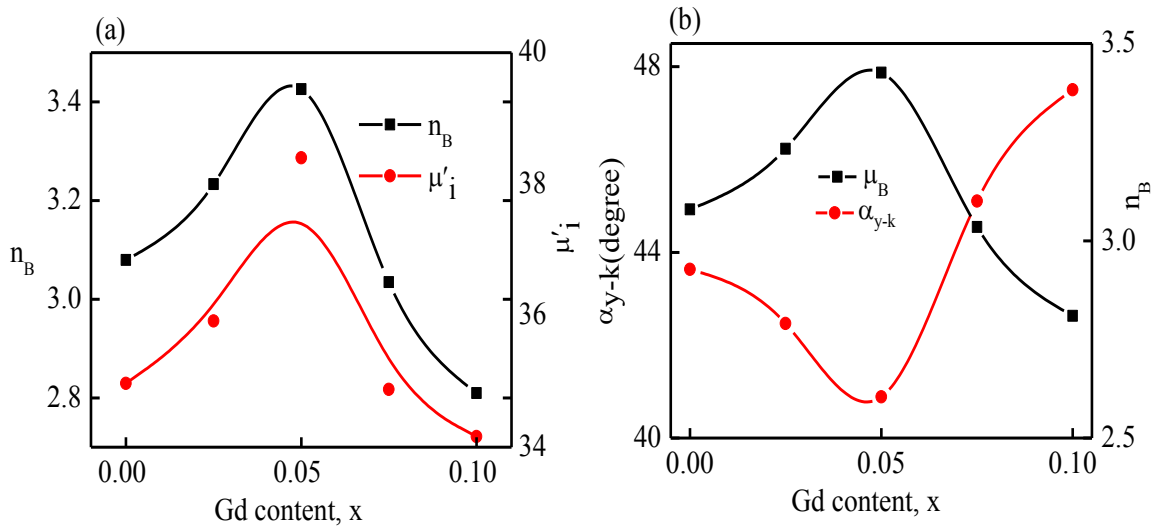

Fig.5.30 The variation of **(a)** number of Bohr magneton, n_B and initial permeability, μ_i' (at 10^4Hz) and (b) α_{y-k} and n_B with Gd content in $Co_{0.40}Cu_{0.20}Zn_{0.40}Gd_xFe_{2-x}O_4$ sintered at 1100 °C in air.

The observed variation in M_S can be explained on the basis of cation distribution and exchange interaction between A and B sites. According to the site occupancy preference [24] it is well known that Co^{2+} and Gd^{3+} prefer octahedral (B) site occupation whereas Zn^{2+} prefer tetrahedral (A) site. Lakhani *et al.* [25] reported that 6–24% of Cu^{2+} ions occupy the *A*-sites depending on the preparative parameters. Fe^{3+} can exist at both sides though they have preference for the octahedral site. Therefore, the cation distribution of various $Co_{0.40}Cu_{0.20}Zn_{0.40}Gd_xFe_{2-x}O_4$ ferrites assumed as

$$(Zn^{2+}_{0.4}Fe^{3+}_{0.9})_A\,[Co^{2+}_{0.2}Cu^{2+}_{0.4}Gd_x\,Fe^{3+}_{1.4-x}]_B\,O_4$$

where the brackets ( ) and [ ] denote A- and B-sites, respectively. In ferrites, the magnetic moment arises mainly from the parallel uncompensated electron spin of individual ion. The intensity of magnetization can thus be explained by considering the metal ion distribution and antiparallel spin alignment of the two sublattice sites as given by Neel‟s model [26]. Néel considered three kinds of exchange interactions between unpaired electrons of two ions lying: (i) both ions at A sites (AA interaction), (ii) both ions at B sites (BB interaction), and (iii) one at A site and the other at B site (AB interaction). AB interaction strongly predominates over AA and BB interactions. The AB interaction aligns all the magnetic spins at A site in one direction and those at B site in opposite direction. A-B super exchange interaction is the strongest one of them and the saturation magnetization is given by the vector sum of the magnetic moments of the individual A and B sublattices i.e. $M_S = M_B - M_A$.

Therefore saturation magnetization is expected to increase as Gd content increases. If ferromagnetic gadolinium prefers to occupy only B sublattices, an increase in saturation magnetization is expected with the replacement of octahedral

Fe^{3+} ion. The gadolinium entry at B-sites at lower concentrations may be expected as the available octahedral site radius is in the order of the substituent ion. In such a case, the observed decrease in magnetization might be attributed to some factors other than the magnetic moments of the ions and the super exchange interactions among them. The fall in magnetization on the addition of gadolinium, the A-B exchange interaction gets weakened while B-B sublattice interaction becomes strong, which in turn disturbs the parallel arrangement of spin magnetic moments on the B- site and hence canting of spin occurs. The canting of the spins gives rise to Yafet-Kittle angle (α_{Y-K}) which is compared to the strength of A-B and B-B exchange interaction [27, 28, 29]. Thus decrease in the magnetic moment beyond $x = 0.050$, indicates the possibility of a non-collinear spin arrangement [11, 30]. The net magnetic moment of the lattice is therefore the difference between the magnetic moments of B and A sublattices, i.e, M = M_B-M_A which can be given by,

$$M_B - M_A = (8.4 + 2x)\,\mu_B - 3\,\mu_B = (5.4 + 2x)\,\mu_B$$

where, $M_B = 0.2\times 1\mu_B + x\times 7\mu_B + 0.4\times 3 + (1.4-x)\times 5\mu_B = (8.4+2x)\,\mu_B$ and $M_A = 0.4\times 0\mu_B + 0.6\times 5\mu_B = 3\,\mu_B$.

Figure 5.27(b) shows α_{Y-K} and number of Bohr magneton (n_B) as a function of Gd content. The α_{Y-K} is calculated at room temperature by using formula [27,25]: $n_B = M_B(x)\cos\alpha_{Y-K} - M_A(x)$. The values of α_{Y-K}, n_B, M_S and saturation magnetizing field ($\mu_0 H_S$) are enlisted in Table 5.2. It is seen that the α_{Y-K} increases for samples with Gd content, x > 0.015. Thus, one can conclude that the increase in α_{Y-K} is attributed to the increased favour of triangular spin arrangement on B-sites

[28]. This leads to reduce the A-B exchange interaction and subsequent decreases in M_S.

Table 5.2 Saturation magnetizing field ($\mu_0 H_S$), saturation magnetization (M_S), number of Bohr magneton (n_B) and Yafet-Kittle angle (α_{Y-K}) for polycrystalline $Co_{0.40}Cu_{0.20}Zn_{0.40}Gd_xFe_{2-x}O_4$.

x	Cation distribution	M_s (emu/g)	$\mu_o H_s$ (T)	n_B (μ_B)	α_{Y-K} (degree)
0.000	$(Zn^{2+}_{0.40}Fe^{3+})[Co^{2+}_{0.40}Cu^{2+}_{0.20}Fe^{3+}]$	72.7	0.2381	3.08	44
0.025	$(Fe^{3+}_{0.60}Zn^{2+}_{0.40})[Co^{2+}_{0.40}Cu^{2+}_{0.02}Gd^{2+}_{0.025}Fe^{3+}_{1.375}]$	75.1	0.3345	3.23	42
0.050	$(Fe^{3+}_{0.60}Zn2^{+}_{0.16})[Co^{2+}_{0.40}Cu^{2+}_{0.02}Gd^{2+}_{0.050}Fe^{3+}_{1.35}]$	78.7	0.3095	3.43	41
0.075	$(Fe^{3+}_{0.60}Zn^{2+}_{0.24})[Co^{2+}_{0.40}Cu^{2+}_{0.02}d^{2+}_{0.075}Fe^{3+}_{1.325}]$	69.0	0.2912	3.04	45
0.100	$(Fe^{3+}_{0.60}Zn^{2+}_{0.32})[Co^{2+}_{0.40}Cu^{2+}_{0.02}Gd^{2+}_{0.100}Fe^{3+}_{1.30}]$	63.0	0.2658	2.81	47

5.9 Dielectric study

In Figure.5.31, the effect of frequency on the ε' and ε'' are shown for the sample sintered at 1100 °C. It can be seen from the figure.5.31 that both ε' and ε'' decrease with increase of frequency. This is normal behavior of ferrites, which was observed before Mg-Zn [31] and Co-Zn ferrite [32] at room temperature. The dielectric properties of ferrites strongly depend on several factors, including the method of preparation, chemical composition, and grain size. It is clearly evident from these figures that the ε' initially decreases rapidly in the low frequency region but at very high frequencies its value becomes so small that it becomes independent of applied frequency for both samples. The sharp decrease in the values of ε' at lower frequencies can be understood on the basis of Maxwell- Wagner two layer model [33] in agreement with Koop's phenomenological theory [34]. Accordingly, the dielectric structure of ferrites is made up of well conducting layer of grains followed by poorly

conducting layer of grain boundaries. The high value of dielectric constant comes from the space charge polarization produced at the grain boundary. The polarization mechanism involves the exchange of electrons between the ions of the same element, which are present in more than one valence state and are distributed randomly over crystallographic equivalent sites. Here the exchange of electrons mainly takes place between Fe^{3+}–Fe^{2+} present at octahedral sites (B-site). During this exchange mechanism the electrons have to pass through the grains and grain boundary of the dielectric medium. Owing to high resistance of the grain boundary, the electrons accumulate at the grain boundary and produce space charge polarization. It is well known that the grain boundaries are more effective at low frequency and grains are effective at high frequency [34–36]. Hence due to the grain boundary affect the dielectric constant decreases rapidly in the low frequency region. At high frequency the grains come into action and also the hopping of electrons cannot follow the high frequency ac field, thus resulting in a decrease in polarization. Consequently, the dielectric constant remains small and constant. Furthermore, the decrease in $\varepsilon^{/}$ and $\varepsilon^{//}$ with increase in frequency is due to the fact that the polarization decreases with increasing frequency then reaches a constant value. The observed variation in $\varepsilon^{/}$ and $\varepsilon^{//}$ may be understood on the basis of space charge polarization, which is due to the inhomogeneous structure governed by the number of space charge carriers and the resistivity of the samples [37, 38]. The space charge polarization resulting from electron displacement on the application of electric field and subsequent charge build up at the insulating grain boundary is a major contributor to the dielectric properties in ferrites. The decrease in $\varepsilon^{/}$ and $\varepsilon^{//}$ is rapid at low frequencies and becomes slow at high frequencies.

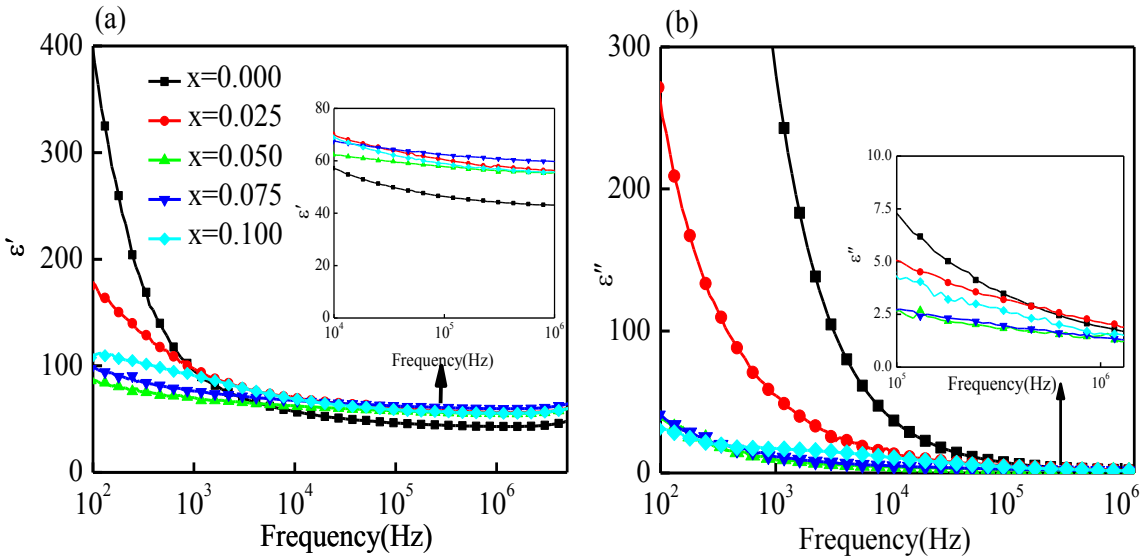

Fig. 5.31 The variation of the real part of dielectric constant ($\varepsilon^{/}$) and imaginary part of the dielectric constant ($\varepsilon^{//}$) with frequency for various $Co_{0.40}Cu_{0.20}Zn_{0.40}Gd_xFe_{2-x}O_4$ at room temperature sintered at 1100 ºC.

Fig-5.32 shows the variation of $\tan\delta_E$ with frequency for $Co_{0.40}Cu_{0.20}Zn_{0.40}Gd_xFe_{2-x}O_4$ at room temperature. The values of $\tan\delta_E$ decreases with the increase of Gd content in $Co_{0.40}Cu_{0.20}Zn_{0.40}Gd_xFe_{2-x}O_4$. The $\tan\delta_E$ in ferrites is considered to originate from two mechanisms: electron hopping and charge defect dipoles. The former contributes to $\tan\delta_E$ in the low frequency region, while in the high frequency range: $\tan\delta_E$ mainly results from the response of the defect dipoles to the ac applied field. These dipoles in ferrites are formed due to change in cation sites, such as Fe^{3+}/Fe^{2+}, during the sintering process. The decrease of tanδ could not be accounted for using Koop"s model [39].

The frequency dispersion of dielectric loss is observed both in the low and high frequency regions. In the low frequency region which corresponds to high resistivity where grain boundary requires more energy to exchange electron between Fe^{2+} and Fe^{3+} ions. Thus the energy loss is high. This loss factor is attributed to

domain wall resonance [40]. Similar behavior has been observed in the dielectric loss vs frequency plots for ferroelectric-ferrite composite by Rahman et al. [40].

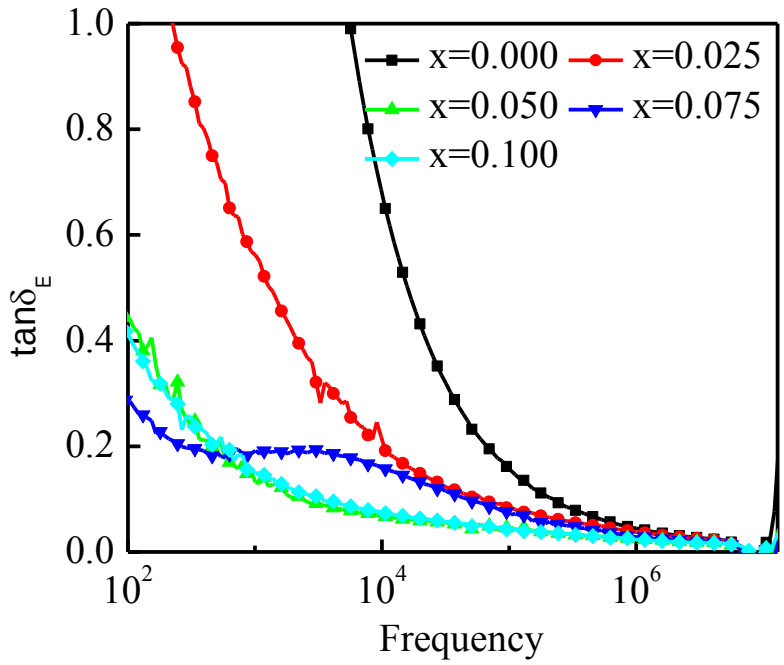

Fig. 5.32 The loss tangent ($\tan\delta_E$) variation with frequency for various $Co_{0.40}Cu_{0.20}Zn_{0.40}Gd_xFe_{2-x}O_4$ at room temperature sintered at 1100 ºC.

At high frequencies, the dielectric loss decreases due to the suppress ion of domain wall motion. When the hopping frequency of electrons between different ionic sites becomes nearly equal to the frequency of the applied field, maximum dielectric loss is observed [41].

5.10 Modulus study

The complex electric modulus approach began when the reciprocal complex permittivity was discussed as an electrical analogue to the mechanical shear modulus [42]. The complex modulus formalism is a very essential and convenient tool to determine, analyze and interpret the dynamical aspects of electrical transport process

in the material, such as the parameters (carrier/ion hopping rate, conductivity relaxation time, etc.) with the smallest capacitance at high frequencies occurring in a dielectric system and thereby large values of permittivity at low frequencies is minimized. From the physical point of view, the electrical modulus corresponds to the relaxation of the electric field in the materials when the electric displacement remains constant. The usefulness of the modulus representation in the analysis of the relaxation properties has been demonstrated for polycrystalline ceramic [42–44]. Electric modulus M^* is defined as

$$M^* = \frac{1}{\epsilon^*} = \frac{\epsilon^{/}}{(\epsilon^{/2}+\epsilon^{//2})} + i\,\frac{\epsilon^{//}}{(\epsilon^{/2}+\epsilon^{//2})} = M^{/} + iM^{//}$$

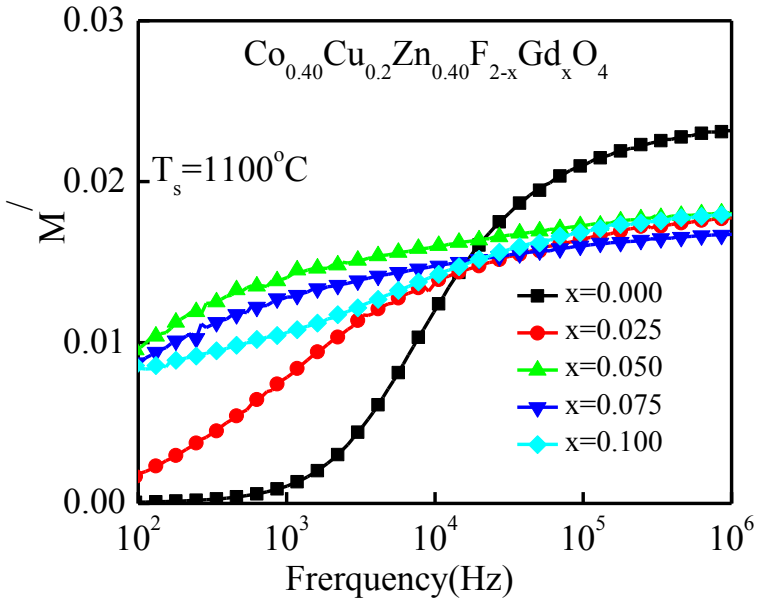

Fig. 5.33 Variation of real part ($M^{/}$) of electric modulus with frequency for various $Co_{0.40}Cu_{0.20}Zn_{0.40}Gd_xFe_{2-x}O_4$.

The variation of real part of electric modulus ($M^{/}$) as a function of frequency for various composition is given in Fig.5.33. The value of $M^{/}$ is very low in the low frequency region. As frequency increases the value of $M^{/}$ increases and reaches a

maximum value at higher frequencies for all compositions due to the release of space charge polarization. Also at lower frequencies $M^{/}$ approaches nearly to zero, confirming the presence of an appreciable space charge polarization at room temperature. The value of $M^{/}$ shows increasing trend from the low frequency value towards the high frequency values as Gd content increases implies the reduction of $\varepsilon^{/}$ in the intrinsic grains [45, 39].

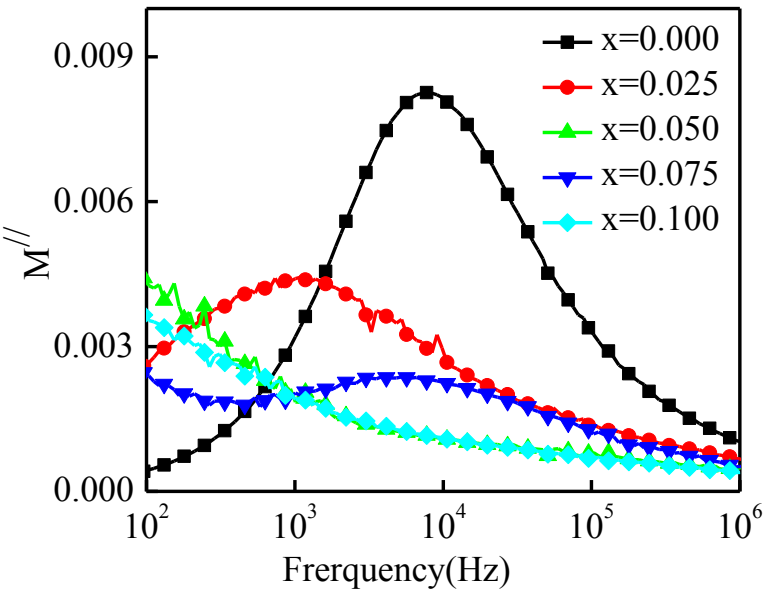

Fig.5.34 Variation of imaginary part ($M^{//}$) of electric modulus with frequency for various $Co_{0.40}Cu_{0.20}Zn_{0.40}Gd_xFe_{2-x}O_4$ at 1100 ºC.

Fig. 5.34 shows the imaginary parts of electric modulus ($M^{//}$) as a function of frequency at various compositions. $M^{//}$ possessed a low value at low frequencies for all compositions. This is probably due to the large value of capacitance at low frequencies. It may be noted from Fig. 5.34 that the position of the peak shifts to lower frequencies as the Gd content is increased which implies that the dielectric relaxation is deactivated with compositions, in which a hopping process of charge

carriers is distributed [46]. $M^{//}$ shows a single asymmetric peak for all the studied compositions, indicating the non-exponential decay of the field.

5.11 Impedance study

The impendence spectrum is relatively new and powerful method of characterizing the electrical properties of materials with their microstructures. The transport properties of polycrystalline materials are greatly influenced by the microstructure, and impedance analysis is a very good technique that usually contains feature(s) which can be directly related to microstructure. In DC measurement the electrical conductivity is actually the sum of electronic contribution from grains, inter-grain boundaries, surface electrodes contacts, etc. While the use of AC measurement at different frequencies makes it possible to discriminate the individual contribution from the overall conduction. Impedance spectroscopy study is the plot of specific complex impedance (impedance per unit length and cross-sectional area), which is useful if various parameters from the different samples are to be compared. To get more insight into the electrical properties, we have studied the impedance spectra (the real part, $Z^{/}$ and the imaginary part, $Z^{//}$) for all samples at room temperature. Figs. 5.35 (a and b) show that $Z^{/}$ and $Z^{//}$ decrease with increasing frequency. The decrease in the values of $Z^{/}$ and $Z^{//}$ with increasing frequency shows that the ac conductivity of the $Co_{0.40}Cu_{0.20}Zn_{0.40}Gd_xFe_{2-x}O_4$ increases as the frequency increases. The frequency dependence $Z^{/}$ indicates dielectric relaxation process as shown in Fig.5.35 [50]. It is also observed that the value of $Z^{/}$ for all compositions coincide at higher frequencies which indicates possible absence of space charge polarization. The higher impedance value at lower frequency is due to the larger space charge polarization.

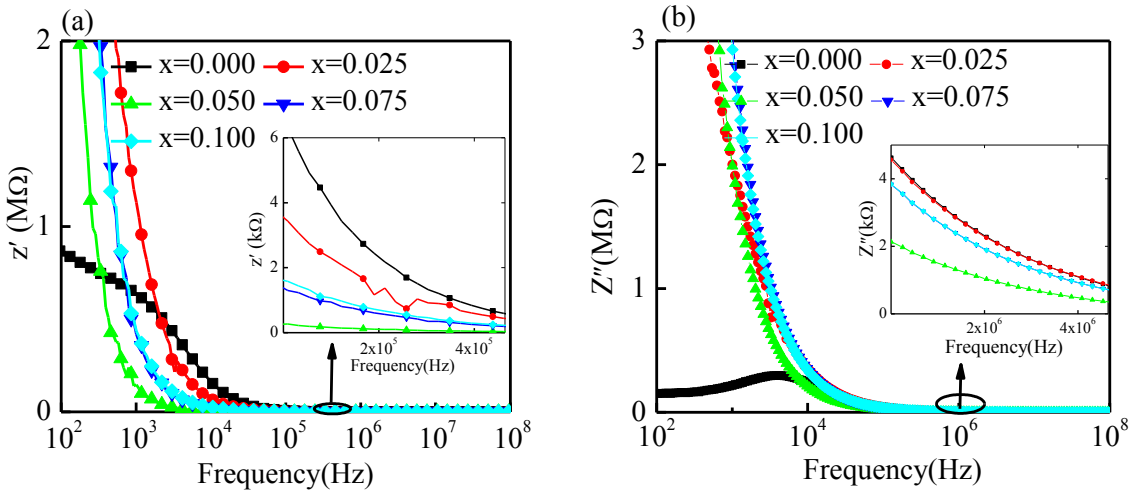

Fig.5.35 Variation of (a) real part ($Z^{/}$) and (b) imaginary part ($Z^{//}$) of impedance with frequency of $Co_{0.40}Cu_{0.20}Zn_{0.40}Gd_xFe_{2-x}O_4$ sintered at 1100 ºC.

The complex impedance plot behavior depends upon the grain size and grain boundary thickness. For smaller grains sample only one semicircle is observed and larger grain samples show two semicircles, that corresponds to grain boundary and grains resistance separately [47, 48]. Size of the semicircle changes with grain size and is the measure of the magnitude of resistance. A single semicircle in $Z^{/}$ vs $Z^{//}$ plot indicates the grain effects and the second semicircle indicates the presence of grain boundary effects. If a third semicircle is present, it indicates the electrode effects. A Nyquist plot typically comprises of two successive semicircles: first semicircle is due to the contribution of the grain boundary at low frequency and second is due to the grain or bulk properties at high frequency of the materials [49]. The pattern in the impedance spectrum is a representative of the electrical processes taking place in the material which can be expressed as an equivalent electrical circuit comprising a parallel combination of resistive and capacitive elements. From the figure.5.36 it is observed that none of samples exhibit ideal semi-circle. It is further noted that the impedance values gradually increases with increasing Gd content. The incomplete

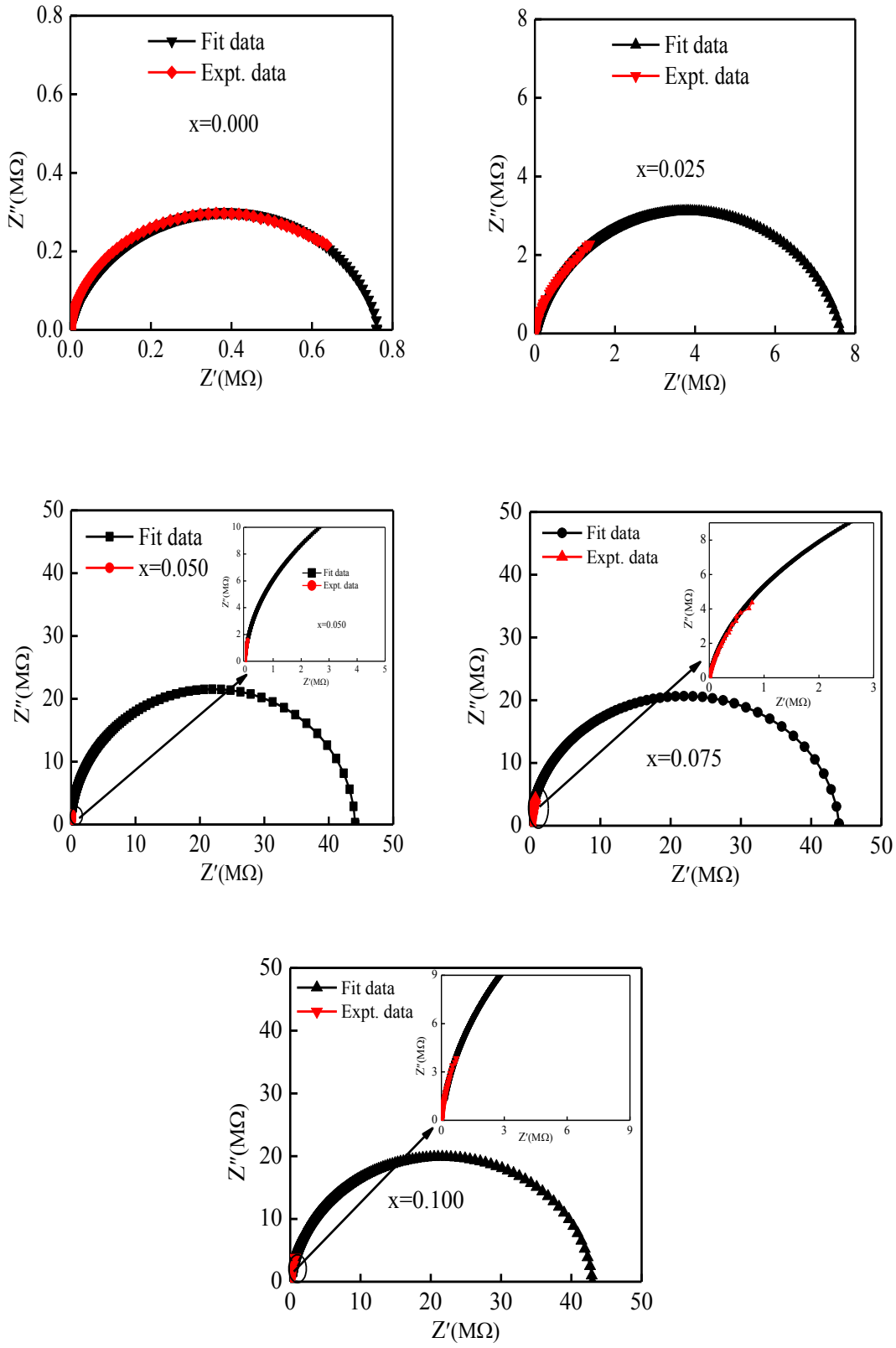

Fig.5.36 The Cole-Cole (Nyquist) plot of $Co_{0.40}Cu_{0.20}Zn_{0.40}Gd_xFe_{2-x}O_4$ at room temperature sintered at 1100 ºC.

semicircle obtained (in high frequency region) the Cole–Cole plot corresponds to the conduction due to grain boundary. The Cole-Cole plot shows the diameter of the semicircle arc increases with Gd content up to x=0.050, then decreases further increase of Gd content. The increase of diameter of the semicircles with Gd content can be attributed from the observed microstructure. It also observed that all the compositions exhibit single semicircular arc. This indicates that the materials have only grain boundary effect to the conduction mechanism at room temperature. As the formation of Gd_2O_3 at the grain boundary reduce grain size and reduction in Fe^{2+} ions which form during the sintering process and this result increase resistances at grain boundary.

5.12 AC conductivity study

The ζ_{AC} is an important parameter for understanding the conduction mechanism inside the materials. Figure 5.37 shows the variation of ac conductivity (σ_{AC}) with frequency at room temperature. The σ_{AC} increases almost linear indicating that the conductivity increases with increasing frequency [50].

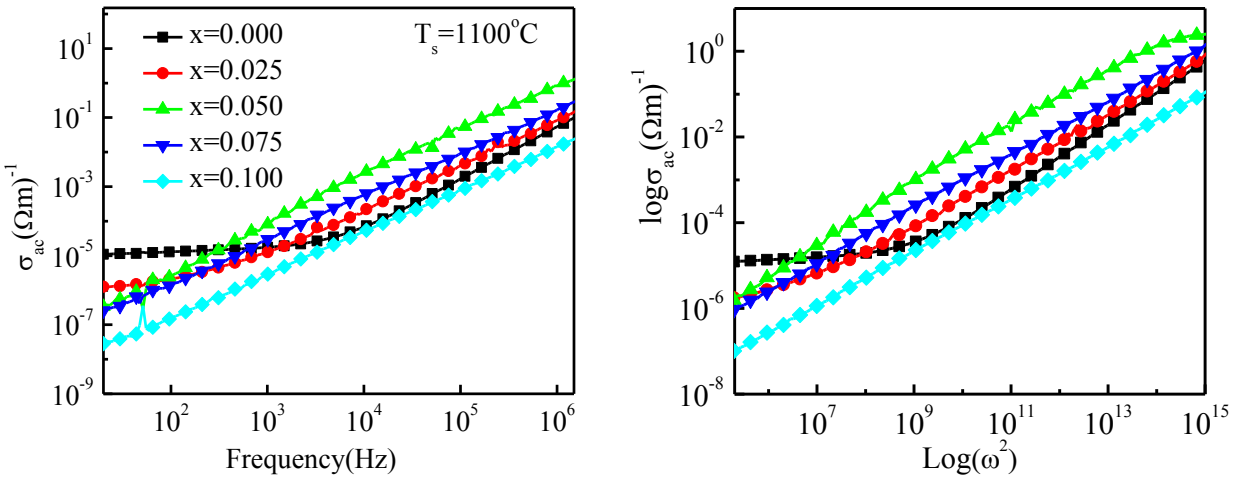

Fig.5.37 The variation of σ_{AC} with frequency for various $Co_{0.40}Cu_{0.20}Zn_{0.40}Gd_xFe_{2-x}O_4$ at room temperature at 1100 ºC

The electrical conductivity in ferrites is mainly due to the hopping of electrons between ions of the same element present in more than one valence state and distributed arbitrarily over crystallographic equivalent lattice sites. As a cubic close-packed oxygen lattice with the cations at the octahedral (B) and tetrahedral (A) sites in ferrites distance between two metal ions on B-B sites is smaller than the distance between two metals ions on the A-A sites. Therefore, electron hopping between A⇔B sites has a very small probability compared with that of B⇔B sites. The hopping between A⇔A sites are less probable due to the fact that there are Fe^{3+} and Zn^{2+} ions at the A sites with largest distance among them, and any Fe^{2+} ions formed during the sintering process preferentially occupy the B sites only. As the Gd^{3+} substitution increases it forced to migrate Fe^{3+} from A sites to B sites which increases the rate of electron hopping between $Fe^{3+}⇔Fe^{2+}$ at B sites, thereby increases the conductivity. It is observed from Fig.5.37 that AC conductivity increases with AC applied field. As the frequency of the AC applied field increases, hopping of charge carriers also increases, thereby increasing the AC conductivity. The variation of AC conductivity with applied frequency could be explained on the basis of Koop‟s model [51]. According to this model, the AC conductivity at low frequency is due to the conducting grain boundaries while, the conductivity at higher frequencies is due to conducting grains [52].It is well known that there are two types polarons viz. small poalrons and large polaons. In small polaron model the ζ_{AC} increases linearly with increase in frequency and in case of large polarons the conductivity decreases with increased frequency [53]. Furthermore the conductivity is almost constant at x=0.00 and x=0.025 which is called σ_{dc}. This is because at lower frequencies the resistive grain boundaries are more active according to the Maxwell –Wagner double layer

model. The frequency independent σ_{dc} is shifted to frequency independent σ_{AC} at hopping frequency indicating the translation from band conduction to polaron hopping conduction [54].

References

[1] Hossain, A. K. M. A., Seki, M., Kawai, T. and Tabata, H., "Colossal magnetoresistance in spinel type $Zn_{1-x}Ni_xFe_2O_4$", Journal of Applied Physics, Vol. 96, pp. 1273-1275, 2004.

[2] Hossain, A. K. M. Akther., Tabata, H., Kawai, T., "Magnetoresistive properties of *$Zn_{1-x}Co_xFe_2O_4$ ferrites*", J. Magn. Magn. Mater.,vol. 320, pp. 1157-1162, 2008.

[3] Raghavendera, A. T., Sagar E., Shirsath, K. Vijaya Kumarc., "Synthesis and study of nanocrystalline *Ni–Cu–Zn* ferrites prepared by oxalate based precursor method", J. Alloys Compd., Vol. 509, pp. 7004–7008, 2011.

[4] Nelson, J. B., Riley, D. P., "An experimental investigation of extrapolation methods in the derivation of accurate unit-cell dimensions of crystals", Proc. Phys. Soc. London, Vol. 57, pp. 160, 1945.

[5] Ben Tahar, L., Smiri, L. S., Artus, M., Joudrier, A. L., Herbst, F., Vaulay, M. J., Ammar , S., Fievet, F., "Characterization and magnetic properties of Sm- and Gd-substituted $CoFe_2O_4$ nanoparticles prepared by forced hydrolysis in polyol", Mater. Res. Bull. Vol. 42, pp 1888-1896, 2007.

[6] Sagar, E., Shirsath, Santosh S., Jadhav, B. G., Toksha, S. M., Patange, and. Jadhav, K. M., "Influence of Ce^{4+} ions on the structural and magnetic properties of $NiFe_2O_4$", J. Appl. Phys., Vol. 110, pp. 013914(1-8), 2011

[7] Cullity, B. D., Stock, S. R, "Elements of X-Ray Diffraction", 3rd Edition, Prentice Hall, 2001.

[8] Valenzuela, R., "Magnetic ceramics", Cambridge University press, 1994.

[9] Siva Ram Prasad, M., Prasad, B. B. V. S. V., Rajesh, B., Rao, K. H., Ramesh, K. V., "Magnetic properties and *DC* electrical resistivity studies on cadmium substituted *Ni–Zn* ferrite system", J. Magn. Magn. Mater., Vol. 323, pp. 2115–2121, 2011.

[10] Costa, A. C. F. M., Tortella, E., Morelli, M. R. and Kiminami, R. H. G. A., "Synthesis, microstructure and magnetic properties of Ni-Zn ferrites", J. Magn. Magn. Mater., Vol. 256, pp. 174, 2003.

[11] Hossain, A. K. M. A., Mahmud, S. T., Seki, M., Kawaia, T. and tabata, H., "Structural, electrical transport, and magntic properties of $Ni_{1-x}Zn_xFe_2O_4$", J. Magn. Magn. Mater., Vol. 312, pp. 210-219, 2007.

[12] Guillaud, C.,"The properties of manganese-zinc ferrites and the physical processes governing them", Proceedings of the IEEE, Vol. 104B, pp. 165-173, 1957.

[13] Smit, J., Wijn, H. P. J., Ferrites, Philips Tech. Library, Netherlands, 1959.

[14] Mahmud, S. T., Hossain, A. K. M. A., Hakim, A. K. M. Abdul, Seki, M., Kawai T., Tabata, H., "Influence of microstructure on the complex permeability of spinel type Ni–Zn ferrite", J. Magn. Magn. Mater., Vol. 305, pp. 269–274, 2006.

[15] Jun, Hu and Mi, Yan, "Preparation of high permeability Ni-Cu-Zn ferrite", Journal of Zhejiang University Science, Vol. 6B (6), pp. 580-583, 2005.

[16] Tsutaoka, T, Ueshima, M., Tokunaga, T., Nakamura, T. and Hatakeyama, K., "Frequency dispersion and temperature variation of complex permeability of Ni-Zn ferrite composite materials", Journal of Applied Physics, Vol. 78(6), pp. 3983-3991, 1995.

[17] Huang, J., "Microstructure and properties of $Ni_{0.5}Zn_{0.5}Fe_2O_4$-$BaTiO_3$ ceramic", Key Engineering Materials Vol. 336-338, pp. 779-782, 2007.

[18] Kang, S. H. and Yoo, H.I., "The effect of nonstoichiometry (δ) on the magnetic properties of $(Mg_{0.22}Mn_{0.07}Fe_{0.71})_{3-\delta}O_4$ ferrite", Journal of Applied Physics, Vol. 88, pp. 4754-4757, 2000.

[19] Caltun, O. F. and Spinu, L., "Magnetic properties of high frequency Ni-Zn ferrites doped with CuO", IEEE Transactions on Magnetics, Vol. 37(4), pp. 2353-2355, 2001.

[20] Rado, G. T., Wright, R. W., Emerson, W. H. and Terris, A., "Ferromagnetism at Very High Frequencies. IV. Temperature Dependence of the Magnetic Spectrum of a Ferrite", Physical Review., Vol. 88, pp. 909-915,1952.

[21] Hossain A. K. M. Akther, T. S. Biswas, S. T. Mahmud, Takeshi Yanagida, Hidekazu Tanaka, Tomoji Kawai, "Influence of Mg and Cr substitution on structural and magnetic properties of polycrystalline $Ni_{0.50}Zn_{0.50-x-y}Mg_xCr_yFe_2O_4$", Materials chemistry and physics, Vol. 113(1), pp. 172-178, 2009.

[22] Globus, A., "Some physical consideration about the domain wall size theory of magnetization mechanism", *J. Phys. Colloques,* Vol. 38, pp. 1-15, 1977.

[23] Smit, J., "Magnetic properties of materials", Mc-Graw Hill, New York, 1971.

[24] Jadhav, S. A., "Magnetic properties of Zn-substituted Li-Cu ferrites", J.Magn.Magn.Mater, Vol. 224, pp. 167-172, 2001.

[25] Lakhani, V. K., Bangchuan Zhao, Lan Wang, Trivedi, U. N., Modi, K. B., "Negative magnetization, magnetic anisotropy and magnetic ordering studies on Al^{3+} substituted copper ferrite", J. Alloys Compd., Vol. 509, pp. 4861–4867, 2011.

[26] Neel, L., *Physica*, 15, pp. 225-234, 1949.

[27] Smit, Jt. and Wijn, H. P. J., *Ferrites*, John Wiley & Sons, New York, 1959.

[28] Karche, B. R., Khasbardar, B. V., Vaingankar, A. S., "X-ray SEM and magnetic properties of Mg-Cd ferrites", J. Magn. Magn. Mater., Vol. 168, pp. 292-298, 1997.

[29] Bercoff, P. G., and Bertorello, H. R., "Localized canting effect in Zn-substitued Ni ferrites", J. Magn. Magn. Mater., Vol. 213, pp. 56-62, 2000.

[30] Yafet, Y. and Kittel, C., "Antiferromagnetic arrangements in ferrites", Physical review, Vol. 87, pp. 290-294, 1952

[31] Jadhav, S. R., Sawant, S. S. and Patil, S. A., "Tempaerature and frequency dependence of initial permeability in Zr^{4+}-substituted Cu-Zn ferrites", J. less-common Met., Vol. 158, pp.199-205, 1999.

[32] Kodama, R. H., "Magnetic nanoparticles", J. Magn. Magn. Mater. Vol. 200, pp. 359-372, 1999.

[33] Maxwell, J. C., "Electricity and Magnetism", Oxford University Press, New York, pp. 828. 1973.

[34] Koops, C. G., "On the Dispersion of Resistivity and Dielectric Constant of Some Semiconductors at Audio frequencies", Phys. Rev. Vol. 83, pp. 121–124, 1951.

[35] Rezlescu, N., Rezlescu, E., "Dielectric properties of copper containing ferrites", Phys. Stat. Sol. (a), Vol. 23, pp. 575-582, 1974.

[36] Irvine, J. T. S., Huanosta, A., Velenzuela, R., West, A. R., "Electrical Properties of Polycrystalline Nickel Zinc Ferrites", J. Am. Ceram .Soc. Vol. 73 pp. 729–732, 1990.

[37] Ahmed, M., El Nimr., M., Tawfik, A. and Aboel Ata, A., "Dialectical Behavior in Co-Zn ferrites", phys. Stat. sol. (a), Vol. 114, pp. 377-382, 1989.

[38] Zhu, J., Tseng, K. J. and Foo, C. F., "Effects of Multi-segment structure in core loss reduction of MnZn ferrite at high frequencies," IEEE Trans. Magn, Vol. pp. 3408-3410, 2000.

[39] Isasi, J., lopez, M. L., Veiga, M. L., Ruiz-Hitzky, E. and pico, C., "Structural characterization and Electrical Properties of a Novel defect Pyrochlore," J. Sol. Stat. Chem., Vol. 116, pp. 290-296, 1995.

[40] Rahaman, M. D., Saha, S. K., Ahmed, T. N., Saha, D. K., Akther Hossain, A. K. M., "Magnetoelectric effect of $(1-x)Ba_{0.5}Sr_{0.5}Zr_{0.5}Ti_{0.5}O_3+(x)Ni_{0.12}Mg_{0.18}Cu_{0.2}Zn_{0.5}Fe_2O_4$ composites", J. Magn. Magn. Mater. Vol. 371, pp. 112-120, 2014.

[41] Fouskova A. and Cross LE., "Dielectric properties of bismuth titanate", J. Appl. Phys., Vol. 41, pp. 2834-2842, 1970.

[42] Mccrum, N. G., Read, B. E., and Williums, G., "An elastic dielectric effects in polymeric solids", New York: Wiley, 1967.

[43] Liu, J., Duan, Ch. G., Yin, W. G. and Mei, W. N. and Smith, R. W. and Hardly, J. R., "Dieletric permittivity and electric modulus in $Bi_2Ti_4O_{11}$", J. Phys., Vol. 119, pp. 2812-2819, 2003.

[44] leon, C., Lucia, M. L., and Santamaria, J., "Correlated ion hopping in single-crystal yttria-stabilized zirconia", Phys. Rev. B, Vol. 55, p. 882-887, 1997.

[45] Sambasiva, Rao, K., Madhava Prasad, D., Murali Krishna, P., Tilak, B and Varadarajulu, K. C. h, "Impedance and modulus spectroscopy studies on $Ba_{0.1}Sr_{0.81}La_{0.06}Bi_2Nb_2O_2$ ceramic", Mater. Sci. Engg. B, Vol.133, pp. 144, 2006.

[46] Nadkarni, G. S. and Simmons, J. G., "Electrical properties of Evaporated Molybdenum Oxide Films," J. Appl. Phys., Vol. 41, pp. 545-551, 1970.

[47] Chowdari, B. V. R., Gopalkrishnnan, R., "ac conductivity analysis of glassy iodomolybdate system", Sol. Stat. Ion., Vol. 23, pp. 225-233, 1987.

[48] Farea, A. M. M., Kumar, S., Batoo, K. M., Yousef, A., Lee, C. G. and alimuddin, "Structure and electrical properties of $Co_{0.5}Cd_xFe_{2.5-x}O_4$ ferrites", J. Alloys Compd., Vol. 464, pp. 361-369, 2008.

[49] E. Barsoukov, J. R. Macdonald, Impedance spectroscopy Theory, Experiment and Applications, Second edition, Wiley-Inter science, New York (1998), p. 2.

[50] Miah, M. J., Khan M. N. I., Akther Hossain, A. K. M., **"**Weak ferromagnetism and magnetoelectric effect in multiferroic $xBa_{0.95}Sr_{0.05}TiO_3–(1–x)BiFe_{0.9}Gd_{0.1}O_3$ relaxors**"** J. Magn. Magn. Mater. Vol. 401, pp. 600-611, 2016.

[51] Richert, R. and Wagner, H., "The dielectric modulus: relaxation verses retardation", Solid Stat. Ion., Vol. 105, pp. 167-173, 1998.

[52] Ya, H., Jackman, R. B. and Hing, p., "Spectroscopic impedance study of nanocrystalline diamond films", J. Appl. Phys., Vol. 94, pp. 7878-7883, 2008.

[53] Mahajan, R. P., Patankar, K. K., Kothale, M. B., Patil, S. A., "conductivity, dielectric behavior and ME effect in copper ferrite- barium titanate composites", Bull. Mater. Sci, Vol. 23(4), pp. 273, 2000.

[54] Rahman, A., Rahman, M. A., Hossain, A. K. M. A., "Effect of Cu^{2+} substitution on structural, magnetic and transport properties of $Fe_{2.5}Zn_{0.5-x}Cu_xO_4$." Journal of Magnetism and Magnetic Materials, Vol.369, pp.168–175, 2014.

CHAPTER 6

CONCLUSIONS

6.1 Conclusions

The following conclusions have been drawn from the study of $Co_{0.40}Cu_{0.20}Zn_{0.40}Gd_xFe_{2-x}O_4$. Various $Co_{0.40}Cu_{0.20}Zn_{0.40}Gd_xFe_{2-x}O_4$ were successfully prepared by standard solid state reaction technique.

- The XRD analysis of various $Co_{0.40}Cu_{0.20}Zn_{0.40}Gd_xFe_{2-x}O_4$ confirms that all the samples have single phase cubic spinel structure. No impurity peak is found in XRD pattern.
- It is clear that the lattice constant, a_o increases with the increase of Gd^{3+} content that follows Vegard's law. This phenomenon is explained on the basis of ionic radii. The ionic radii of the cataions used in $Co_{0.4}Cu_{0.2}Zn_{0.4}Gd_xFe_{2-x}O_4$ are 0.91Å (Gd^{3+}) and 0.64 Å (Fe^{3+}). Here Fe is substituted by Gd. So increase in lattice a_o is expected with increasing Gd content.
- It is observed that the density of $Co_{0.4}Cu_{0.2}Zn_{0.4}Gd_xFe_{2-x}O_4$ increases with increasing sintering temperature up to 1100 °C, then decreases. On the other hand, porosity (p) of the samples decreases with sintering temperature up to 1100 °C and an increasing trend is observed beyond it. At high sintering temperatures density decreases, because the intragranular porosity increases as a result of discontinuous grain growth that leads to decrease the sintered density.
- $\mu_i^{/}$ and $\mu_i^{//}$ increase with Gd^{3+} substitution up to x=0.050 in $Co_{0.4}Cu_{0.2}Zn_{0.4}Gd_xFe_{2-x}O_4$ and after that they decrease. With the increase of sintering temperature the real part of initial permeability ($\mu_i^{/}$) increases for the sample sintered at 1100 °C and above 1100 °C a decreasing trend is observed.

Larger grains tend to consist of a large number of domain walls. The initial permeability increases with grain size. The domain wall motions are affected by grain size and enhance with the increase of grain size thus the $\mu_i^{/}$ increases. Therefore in the present case, variation of the initial permeability is strongly influenced by its grain size and porosity.

- The value of *Q-factor* increases with an increase of frequency. It is also observed that the value of *Q-factor* increases with increasing Gd content from x=0.000 to x=0.050 then it decreases. By increasing Gd content, the RQF increases and the peak associated with the RQF shifting to higher frequencies. Similar variation is observed for $Co_{0.40}Cu_{0.20}Zn_{0.40}Gd_xFe_{2-x}O_4$ sintered at other temperatures as well. Among all the studied samples, highest value of *Q*-factor (= 2714) is observed for $Co_{0.40}Cu_{0.20}Zn_{0.40}Gd_xFe_{2-x}O_4$ sintered at 1100 °C, similar to $\mu_i^{/}$. Above 1100 °C, *Q-factor* is found to decrease because at higher sintering temperature, abnormal grain growth occurs which creates trapped pores inside the grain. This increasing amount of pores influences the loss factor and turns into higher value which results a lower value of *Q*-factor.
- The magnetization (M) as a function of applied magnetic field (H) for various $Co_{0.40}Cu_{0.20}Zn_{0.40}Gd_xFe_{2-x}O_4$ (with x = 0.000-0.100 at a step of 0.025) measured at room temperature. The magnetization of all samples increases linearly with increasing the applied magnetic field up to 0.1T. Beyond this applied field magnetization increases slowly and then saturation occurs. It indicates that all the samples are in ferromagnetic state. It is observed that the value of M_S increases up to x = 0.050, then decreases further increase of Gd content. The observed variation in M_S can be explained on the basis of cation distribution and spin canting.

- The value of $\varepsilon^{/}$ (real part of dielectric constant) and $\varepsilon^{//}$ (imaginary part of dielectric constant) decrease with the increase of frequency. This is normal behavior of ferrites. The decrease in $\varepsilon^{/}$ and $\varepsilon^{//}$ with increase in frequency is due to the fact that the polarization decreases with increasing frequency then reaches a constant value. The observed variation in $\varepsilon^{/}$ and $\varepsilon^{//}$ may be understood on the basis of space charge polarization, which is due to the inhomogeneous structure governed by the number of space charge carriers and the resistivity of the samples. The space charge polarization resulting from electron displacement on the application of electric field and subsequent charge build up at the insulating grain boundary is a major contributor to the dielectric properties in ferrites. The decrease in $\varepsilon^{/}$ and $\varepsilon^{//}$ is rapid at low frequencies and becomes slow at high frequencies.
- The value of $M^{/}$ is very low in the low frequency region. As frequency increases the value of $M^{/}$ increases and reaches a maximum value at higher frequencies for all compositions due to the release of space charge polarization. Also at lower frequencies $M^{/}$ approaches nearly to zero, confirming the presence of an appreciable space charge polarization at room temperature. The value of $M^{/}$ shows increasing trend from the low frequency value towards the high frequency values as Gd content increases implies the reduction of $\varepsilon^{/}$ in the intrinsic grains.
- $M^{//}$ possessed a low value at low frequencies for all compositions. This is probably due to the large value of capacitance at low frequencies. It may be noted that the position of the peak shifts to lower frequencies with increasing Gd content, which implies that the dielectric relaxation is deactivated with compositions, in which a hopping process of charge carriers is distributed. $M^{//}$

shows a single asymmetric peak for all the studied compositions, indicating the non-exponential decay of the field.

- $Z^{/}$ and $Z^{//}$ decrease with increasing frequency. The decrease in the values of $Z^{/}$ and $Z^{//}$ with increasing frequency shows that the ac conductivity of the $Co_{0.40}Cu_{0.20}Zn_{0.40}Gd_xFe_{2-x}O_4$ increases as the frequency increases. The frequency dependence $Z^{/}$ indicates dielectric relaxation. It is also observed that the value of Z for all compositions coincide at higher frequencies which indicates possible absence of space charge polarization. The higher impedance value at lower frequency is due to the larger space charge polarization.
- The cole-cole plot shows the diameter of the semicircle arc increases with Gd content up to x=0.050, then decreases further increase of Gd content. The increase of diameter of the semicircles with Gd content can be attributed from the observed microstructure. I also observed that all the compositions exhibit single semicircular arc. This indicates that the materials have only grain boundary effect to the conduction mechanism
- The σ_{AC} increases with increasing frequency. The variation of AC conductivity with applied frequency can be explained on the basis of Joncher's power law. According to this model σ_{AC} at lower frequency is due to the conducting grain boundaries while the conductivity at higher frequencies is due to the conducting grain. The conductivity is almost constant at x=0.00 and x=0.025 which is called σ_{dc}. This is because at lower frequencies the resistive grain boundaries are more active according to the Maxwell –Wagner double layer model. The frequency independent σ_{dc} is shifted to frequency independent σ_{AC} at hopping frequency indicating the translation from band conduction to polaron hopping conduction.

- In conclusion it can be said that the composition $Co_{0.40}Cu_{0.20}Zn_{0.40}Gd_xFe_{2-x}O_4$ shows the maximum value of magnetic and electrical properties at x=0.025 for sintering temperature 1100 °C. This result indicates that it may have potential applications as ferrite materials.

- **6.2 Suggestions for future work**

  The temperature dependent initial permeability can be measured for $Co_{0.40}Cu_{0.20}Zn_{0.40}Gd_xFe_{2-x}O_4$. Susceptibility measurements with the variation of temperature can be carried out for the prepared sample. It was found that among the gadolinium doped CoCuZn ferrites $(Fe^{3+}_{0.60}Zn^{2+}_{0.16})$ $[Co^{2+}_{0.40}Cu^{2+}_{0.02}Gd^{2+}_{0.050}Fe^{3+}_{1.35}]$ had the maximum permeability $\mu_i^{/}$ and maximum Q-factor. So *Mg, Ca, La* and other Metals which prefer a sublattice to occupy, can be substituted in $Co_{0.40}Cu_{0.20}Zn_{0.40}Gd_xFe_{2-x}O_4$ to enhance the permeability value. Sintering additives like Bi_2O_3 and V_2O_5 can be mixed to promote densification and getting better result in lower sintering temperatures to magnetic materials.